POLITECNICO DI MILANO
DEPARTMENT AEROSPACE SCIENCE AND TECHNOLOGY
DOCTORAL PROGRAM IN AEROSPACE ENGINEERING

NON-IDEAL COMPRESSIBLE-FLUID DYNAMICS: DEVELOPING A COMBINED PERSPECTIVE ON MODELING, NUMERICS AND EXPERIMENTS

Doctoral Dissertation of:
Giulio Gori

Supervisor:
Prof. A. Guardone

Co-supervisor:
Prof. P. M. Congedo

Co-supervisor:
Prof. O. Le Maître

Tutor:
Prof. G. Gibertini

The Chair of the Doctoral Program:
Prof. P. Masarati

2019 – XXX

Dedicated to Dino

ACKNOWLEDGMENTS

The research work presented in this thesis was carried out at Politecnico di Milano, Italy, in the Laboratory of Compressible-fluid dynamics for Renewable Energy Applications (CREALab), between years 2014 and 2018. This research was supported through the European Research Council (ERC) Consolidator Grant N. 617603, Project NSHOCK funded under the FP7-IDEAS-ERC scheme, and through the UTOPIAE Marie Curie Innovative Training Network, H2020-MSCA-ITN-2016, Grant Agreement number 722734. The author gratefully acknowledge the support of NVIDIA Corporation with the donation of the two Tesla K40 GPU which were extensively used to obtain some of the developments presented this dissertation.

I would like to thank my supervisor, professor Alberto Guardone, for the irreplaceable advice and the priceless support provided me during the development of this dissertation. Alberto, your relentless dedication is outstanding and I am extremely proud of having been a student of yours.

I am also deeply indebted to my co-supervisors, professor Olivier Le Maître and professor Pietro M. Congedo, for their passionate guidance and their tireless support during this last year in France. I would like to thank the reviewers, Professor Gianluca Iaccarino and Professor Sergio Pirozzoli, for the time devoted to the review of this thesis and for their valuable suggestions.

To all my friends from the CREALab, Andrea, Barbara, Camilla, Davide, Gianluca, Giorgia, Luuc, Marta e Simone, thank you, these years have been amazing. Special thanks to all the guys and friends from the B14 building: I will never forget the enlightened discussions and the challenging problems we addressed together, during our marvelous lunch breaks. Many thanks also to João, my colleague and friend in Paris, for the thoughtful discussions we have had since the very first day I arrived in France.

I would also like to thank my numerous friends, for supporting me in my Ph.D. endeavor. Eventually, I would like to thank my family for their devoted support and their unconditional encouragement.

Giulio Gori
Milano, January 2019

SUMMARY

Non-Ideal Compressible-Fluid Dynamics (NICFD) is the branch of fluid mechanics devoted to the study of compressible flows whose behavior deviates from the one predicted by the ideal-gas model. This behavior is typical of molecular complex compounds in the vapor phase, namely when the operating thermodynamics conditions are close to the liquid-vapour saturation curve and critical point. NICFD flows are characterized by peculiar features which are not physically admissible under the ideal flow assumption, like for instance a non-ideal increase of the speed of sound upon isentropic expansion. Complex thermodynamic models were devised and applied to the theoretical analysis and numerical simulation of non-ideal flows. Nevertheless, only few experimental data in the NICFD regime were available up to date. Nowadays, the NICFD community is calling for the development of reliable and predictive numerical tools. To do so, the aim is to rely on and mix results from experiments, computations and theory. Since NICFD is a quite unexplored field, the objective is not only to numerically reproduce an observed phenomenon with a high level of fidelity, but also to develop tools which might be reasonably used to predict the reality in situations for which they were not specifically validated nor tested. To this extend, reliable numerical predictions require the further development of sophisticated physical models as well as a systematic treatment of calibration and validation procedure.

This dissertation, moving from the first-ever observations of non-ideal compressible flows, develops a combined perspective on modeling, numerics and experiments regarding NICFD flows and it provides advancements in all the mentioned branches. In this context, this work is a preliminary attempt to answer the craving of the NICFD community for a substantial improvement of the currently available numerical prediction tools and physical models. Moreover, results from experiment, computation and theory are combined using an uncertainty quantification framework, paving the way for a future systematic and comprehensive treatment of the inherent uncertainties.

The findings reported in the thesis reveal the existence of an unprecedented non-ideal effect. Namely, it is predicted that an overall Mach number increase may occur upon flow compression across steady oblique shock waves in fluids belonging to a special family. For these fluids, it is shown that there exists a particular subspace of the non-ideal region for which this unprecedented phenomenon is admitted. Moreover, it is also shown that, in a non-ideal regime, the flow maximum turning angle and

the shock wave slope, w.r.t. the upstream flow direction, strictly depend on the whole pre-shock state. This oppose the physics ruling out dilute gas flows, for which the variation of fluid properties across the shock solely depend on the pre-shock Mach number value.

The dissertation presents several numerical tools that are developed specifically to deal with complex fluid flows in the non-ideal regime. In particular, the thesis presents the verification of a Non-Ideal Computational Fluid Dynamics (CFD) solver. Moreover, the dissertation reports the very first accuracy assessment of the thermodynamic models implemented in the solver, against experimental data from dynamic test cases. The comparison of numerical prediction against experimental data was complemented with an uncertainty quantification analysis. Results report evidences claiming the reliability of the numerical implementation and the predictiveness of the solver.

Eventually, the dissertation reports an investigation of the dynamics of pressure probes for high frequency measurements carried out for fluids in a non-ideal regime. Moreover, numerical tools are exploited to develop a Bayesian inference framework which is ultimately used to infer material-dependent fluid parameters. The framework returns substantial indications towards the development of future experiments. Furthermore, results point out either an epistemic uncertainty underlying the computational model or a biased experimental measurement process.

SOMMARIO

Non-Ideal Compressible-Fluid Dynamics (NICFD) (i.e., fluidodinamica delle correnti comprimibili non-ideali) è la branca della fluidodinamica che si occupa di studiare correnti di fluido comprimibili il cui comportamento differisce rispetto a quanto previsto dalla legge di stato per i gas ideali. Questo particolare comportamento è tipico di sostanze formate da molecole molto complesse e si verifica quando il fluido è in forma di vapore, in uno stato termodinamico vicino alla curva di saturazione e con valori di pressione e temperatura nell'ordine di quelli critici. Quando la corrente si trova nel regime non-ideale, alcuni inusuali fenomeni, altrimenti non ammissibili in condizioni di flusso ideale, potrebbero apparire. Un esempio di un fenomeno associato ad effetti non-ideali è l'aumento della velocità del suono associata ad un'espansione isentropica. Per descrivere accuratamente una corrente non-ideale sono necessari complessi modelli termodinamici. In passato, questi modelli sono stati sviluppati e applicati con successo allo studio teorico e numerico di flussi non-ideali. Nonostante tutto, si riscontra una grave carenza di dati sperimentali dovuta principalmente alla elevata complessità nel realizzare esperimenti senza incorrere nella decomposizione chimica del fluido.

Oggigiorno, la comunità scientifica necessita di strumenti numerici che siano affidabili e in grado di predirre la realtà con adeguata accuratezza. Per raggiungere questo scopo gli sforzi sono rivolti a combinare i risultati di esperimenti con i risultati provenienti da simulazioni numeriche e sviluppi teorici. Lo studio di correnti non-ideali rappresenta un campo per molti versi ancora inesplorato. Da questo punto di vista, l'obiettivo non è solo quello di riprodurre virtualmente un fenomeno osservato con elevata fedeltà, ma è anche quello di sviluppare strumenti che possano essere utilizzati ragionevolmente anche per prevedere la realtà in situazioni per cui non sono stati espressamente creati e validati. A questo fine, lo sviluppo di strumenti numerici affidabili necessita dell'ulteriore sviluppo di sofisticati modelli fisici come anche di un approccio sistematico alle procedure di calibrazione e validazinoe.

Questa tesi è stata sviluppata a partire dalle prime misure sperimentali mai realizzate riguardanti correnti non-ideali. In particolare, viene qui sviluppato un approccio che combina risultati teorici, sperimentali e numerici e vengono presentati progressi in tutti e tre gli aspetti. Nel contesto dello studio di correnti non-ideali, questo lavoro rappresenta un primo tentativo di rispondere alle esigenze della comu-

nità scientifica, che chiede un miglioramento degli strumenti numerici e dei modelli fisici attualmente disponibili. Inoltre, risultati teorici, sperimentali e numerici vengono combinati all'interno di un più ampio contesto che prevede l'utilizzo di tecniche avanzate per la quantificazione delle incertezze intrinseche.

I risultati riportati in questa tesi rivelano l'esistenza di un effetto non-ideale mai osservato prima. Limitatamente a particolari fluidi, viene previsto un possibile incremento del numero di Mach attraverso onde d'urto compressive oblique. Inoltre, viene anche mostrato come, in regime non-ideale, l'angolo di deflessione massima del flusso e l'angolo che l'urto forma con la direzione della corrente dipendono anche dallo stato della corrente a monte. Questo contrasta con la fisica caratterizzante le correnti ideali, dove la variazione delle proprietà del fluido attraverso l'urto, e il valore dei due angoli menzionati prima, dipendono esclusivamente dal valore del numero di Mach a monte.

In questa tesi sono inoltre presentati diversi strumenti numerici espressamente sviluppati per riprodurre aspetti caratteristici delle correnti non-ideali. In questo lavoro viene descritto il processo di verifica dell'implementazione di un solutore numerico per la fluidodinamica non-ideale. Inoltre, in questa tesi viene presentata la prima valutazione dell'accuratezza dei modelli termodinamici, implementati nel solutore, basata su veri dati sperimentali. Il confronto tra dati numerici e sperimentali è rafforzato da un'analisi delle incertezze che evidenzia l'affidabilità e la predittività del solutore.

Infine, questa tesi tratta lo studio della risposta instazionaria di prese di pressione tipicamente sviluppate per fluidi ideali ma utilizzate comunemente per condurre misurazioni ad alta frequenza in correnti non-ideali. Inoltre, gli strumenti numerici presentati vengono utilizzati nel contesto di un processo di inferenza bayesiano con lo scopo di calibrare i parametri (dipendenti dal fluido in esame) che compaiono nel modello termodinamico di Peng-Robinson. Sebbene infruttuoso, questo tentativo fornisce indicazioni riguardo allo sviluppo di futuri esperimenti. In particolare, i risultati suggeriscono la presenza di una fonte di incertezza epistamica che affligge, possibilmente, sia il modello computazionale utilizzato per riprodurre l'esperimento numericamente, sia le misure sperimentali stesse (le poche attualmente disponibili) che potrebbero essere potenzialmente affette da un errore intrinseco.

TABLE OF CONTENTS

NOMENCLATURE

Acronyms

NICFD	- Non-Ideal Compressible-Fluid Dynamics
TROVA	- Test-Rig for Organic Vapours
MDM	- Octamethyltrisiloxane, $C_8H_{24}O_2Si_3$
EoS	- Equation of State
DoE	- Design of Experiment
ORC	- Organic Rankine Cycle
CFD	- Computational Fluid Dynamics
BZT	- Bethe-Zel'dovich-Thompson
PIG	- Polytropic Ideal Gas
vdW	- van der Waals
PR	- Peng-Robinson
PE	- Primary Energy
PDE	- Partial Differential Equation
ARS	- Approximate Riemann Solver
HLLC	- Harten-Lax-van Leer Contact scheme
$AUSM^+$	- Advection Upstream Splitting Method scheme
MUSCL	- Monotonic Upwind Scheme for Conservation Laws
RMSE	- Root Mean Squared Error
UQ	- Uncertainty Quantification
MCMC	- Markov-Chain Monte-Carlo
PCE	- Polynomial Chaos Expansion
U	- Uncertainty related to a quantity

Greek alphabet

ρ - Density
Γ - Fundamental derivative of gasdynamics
β - Shock angle
θ - Flow deviation angle
γ - Specific heat ratio
ω - Acentric factor
λ - Bulk viscosity coefficients
μ - Dynamic viscosity coefficients
κ - Thermal conductivity coefficient

Latin alphabet

R - Specific gas constant
a - van der Waals intermolecular force constant
b - Gas co-volume
c - Speed of sound
v - Specific volume
e - Specific internal energy per unit mass
s - Specific entropy per unit mass
h - Specific enthalpy per unit mass
T - Temperature
P - Pressure
M - Mach number
q - Heat
W - Work
Z - Compressibility factor
n - Number of moles
f - Number of degree of freedom of the molecule
$\mathcal{S}$ - Fundamental function for entropy
$\mathcal{E}$ - Fundamental function for energy
$\mathcal{M}$ - Molecular weight
$\mathcal{P}$ - Probability
$\mathcal{L}$ - Likelihood function
$\mathcal{U}$ - Uniform probability density distribution
$\mathcal{N}$ - Normal probability density distribution

Superscripts

t - Total quantity

Subscripts

A - Pre-shock state
B - Post-shock state
in - Quantity entering the control volume
out - Quantity exiting the control volume
ref - The value express a reference quantity
cr - The value refers to the variable at the critical point
min - Minimum value the variable may assume
max - Maximum value the variable may assume
n - Vector component normal to a reference direction
t - Vector component tangent to a reference direction
∞ - The value refers to the upstream unperturbed conditions

CHAPTER 1

INTRODUCTION

1.1 Introduction

In the last centuries mankind witnessed a relentless increase of global energy consumption. The energy demand is fostered by the continuous growth of large scale economies that harvest Earth resources in a never ending effort to supply goods and services to a steadily enlarging world population.

The global Primary Energy (PE) consumption reached 168,519 TWh in 2015 [1, 2], with a positive increasing trend recorded during the whole last century. The term PE refers to the energy potentially found in nature i.e., the energy contained in those resources that have not yet been subject to any human-engineered conversion process. Without any restriction, PE refers either to non-renewable or renewable sources, like for instance raw fuels, solar power, geothermal energy and so on. Despite a limited slowdown, mostly related to the 2008 economical crisis, the growing trend in global demand has been overwhelming over recent years. Besides, the available observations do not account for the amount of heat and electricity consumed off-grid, by isolated villages and industries.

As registered in 2017 [3], fossil fuels (coal, peat, shale, oil and natural gas) represent a share of approximately 80% of the global PE supply. Biofuels provide 10% while nuclear and renewable energies are left with a 5% share each. Studies reveal that only 18% of PE is converted into electricity and that the remaining part goes into heat and transportation.

Along with the relentless energy demand growth, concerns were raised about the drawback of an uncontrolled exploitation of natural resources. Indeed, the consumption of energy extracted from non-renewable sources, in particular fossil fuels, is usually associated to environmental pollution. The United Nations Development Programme's World Energy Assessment of 2000 [4] investigates the challenges underlying the shift from fossil fuels to renewable energy sources. International agreements set during the last years, like for instance the EU 2009 Renewable Energy Directive, established strict regulations to foster the exploitation of clean and renewable energies in place of fossil fuels.

Since the beginning of the third millennium the share of energy production related to renewable energy grew at the highest rate in history. Unfortunately, during the same period the exploitation of oil, coal, and natural gas kept growing at a much higher rate, thus frustrating the endeavor undertaken by the international community. For this reasons, sustainability, green economy, global worming, ozone layer depletion and water and air pollution are topics of relevant interest for the current and next human generations.

To address these problems, and to improve the efficiency of power generation processes, among other solutions the community turned in favor of the exploitation of low temperature sources and energy recover from biomass combustion, industrial waste heat, geothermal heat and solar ponds. Currently, the interest is largely focused on innovative fluids to be employed in power plants. Indeed, the most suitable fluids

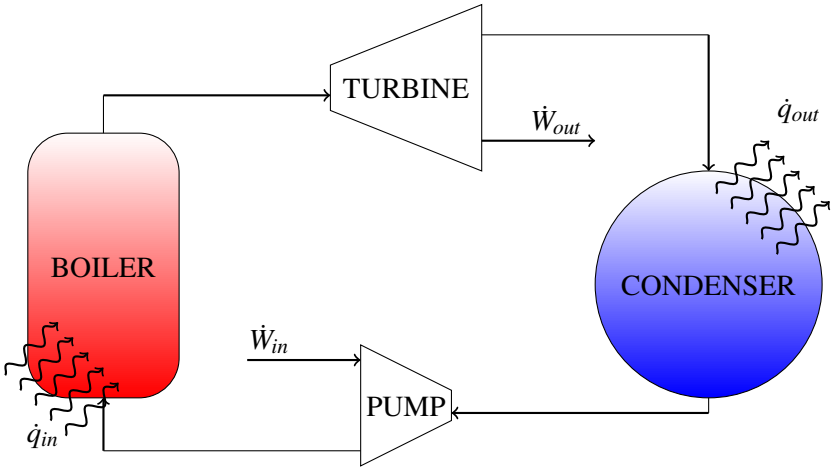

Figure 1.1: power production system based on the standard Rankine cycle. The working fluid is pumped into a boiler where the liquid evaporates (if dealing with a superheated Rankine cycle, the vapor is further heated). The vapor is then forced through a turbine, to extract useful work $\dot{W}_{out}$. Later, the vapor reaches a condenser where it passes into a liquid phase. The cycle is thus rebooted.

are endowed with particular characteristics such as a low boiling point, high thermal stability, safeness (non-flammability), a large availability and a low cost. These characteristic are generally found, but not only, in substances of molecular complex structure such as hydrocarbons or perfluorcarbons.

Organic Rankine Cycle (ORC) applications are named after their extensive use of organic compounds as working fluid within a Rankine cycle. In practice, ORCs systems rely on the well-known Rankine Cycle but they take advantage of carbon-based fluids in place of water. With reference to Fig. 1.1, in a Rankine Cycle the working fluid in its liquid phase is initially forced into a boiler (providing some external power $\dot{W}_{in}$ to a pump). In the boiler, the fluid evaporates thanks to the heat $\dot{q}_{in}$ from the source. The temperature and the pressure of the gas reach relatively large values before being conveyed to an expansion device (turbine), to extract useful work $\dot{q}_{out}$. Eventually, the fluid passes through a condenser, where it is cooled down and it is turned again into liquid. Eventually, the fluid is recovered by a pump, to reboot the cycle. Naturally, the net power output is equal to the difference between $\dot{W}_{out} - \dot{W}_{in}$. To maximize this difference, and increase the efficiency of the system, ORC devices are designed to produce an expansion in the close proximity of the fluid saturation curve, near its critical point. This allows to exploit some peculiar properties of molecular complex substances, which result in an increased process efficiency. For these reasons, the fluid experiences very extreme conditions during the cycle.

Non-Ideal Compressible-Fluid Dynamics (NICFD) is a relatively new branch of science devoted to the investigation of fluid flows at dense conditions i.e., density and

pressure are close to their critical point values. Indeed, for the vast majority of engineering applications the thermodynamics of a gas flow is reasonably well described by the *Ideal Gas Law*. The Ideal Gas Law consistently applies to a volume of gas in dilute conditions i.e., at low pressures and low values of density. In these conditions, the molecules interact only through elastic collision and a large part of the physics ruling the kinematics of particles can be neglected without any significant loss of accuracy. In the particular thermodynamic conditions of interest for ORC applications, the inter-molecular forces perform a major role. Within this limit, the gasdynamics is characterized by a whole new set of unusual phenomena that are interesting both from the theoretical and from the industrial perspective. As mentioned, ORC devices can benefit from non-ideal effects to improve the efficiency of the process. To this extent, a deep understanding of the NICFD is of utmost importance for the improvement of ORC system performances and justifies the ongoing research and development in this relatively recent branch of fluid mechanics.

For instance, a well-known non-ideal effects, the so-called *retrograde* behavior, has major implications for ORC. The presence of moisture within the plant have a detrimental effect on the efficiency of the cycle and it often results in damages to the turbine blades. A fluid endowed with a retrograde behavior can be expanded from the saturated vapor line into the superheated region, avoiding the detrimental formation of moisture. On the contrary, steam powered plants require the water to reach a largely superheated condition i.e., a larger amount of heat must be transferred to the fluid, to avoid the formation of moisture at the turbine exhaust. Moreover, non-ideal effects allow to recover a larger amount of thermal energy from the hot vapor exiting the expander, thus yielding an additional increase in cycle efficiency. Furthermore, working fluids with a low boiling temperature allow the use of ORC technology in several applications, like waste heat recovery from low/medium temperature sources, for which it would be difficult, if not impossible, to employ traditional water/steam technology. Therefore, it is straightforward that the optimal design of an ORC process is strictly related to a deep understanding of the NICFD aspects.

Non-ideal flow applications range from super-critical CO_2 flows in nuclear reactors [5] to the flows of interest renewable energy ORC applications [6–9]. Beside the mentioned ORC power systems, it is worth to recall that NICFD is also relevant for rocket propulsion, refrigerating systems, oil & gas applications and chemical or pharmaceutical applications [10–12]. Moreover, applications include also sterilization and cleaning [13].

In the last decades the scientific community has been racing to expand our knowledge about NICFD. As a consequence, the need to foster innovation in the NICFD field brought to the construction of experimental facilities suitable for the investigation of fundamental properties of non-ideal flows. The Test-Rig for Organic VApors (TROVA) at Politecnico di Milano [14, 15] is a blow-down wind tunnel where supersonic expansions of molecular complex fluids in the non-ideal regime are achieved. The Flexible Asymmetryc Shock Tube (FAST) at TU Delft [16, 17] consists in a

Ludwieg-tube to generate shock waves in dense gas conditions. The FAST is conceived to measure the velocity of waves propagating in dense vapors of organic fluids. Moreover, Delft university is finalizing the construction of the Organic Rankine Cycle Hybrid Integrated Device (ORCHID) [18], to investigate high temperature supersonic expanding flows, in a non-ideal regime, and to test mini-ORC expanders. Lappeenranta University of Technology is currently testing micro-ORC devices designed for the exploitation of waste heat from exhaust gases, in automotive applications. In particular, a micro-ORC test-rig using waste heat from Diesel engine exhaust gases was recently built at the Laboratory of Fluid Dynamics [19, 20]. The ORC Ludwieg tube, at Whittle Laboratory of University of Cambridge, is a Ludwieg-tube designed to study supersonic axial vane cascades, with a particular focus on trailing edge effects [21] The facility is designed to operate with several gases including air, CO_2 and organic fluids. At Münster University of Applied Sciences, the Closed Loop Organic Wind Tunnel (CLOWT), a closed-loop continuous-running wind tunnel implementing a closed gas cycle, is currently under construction [22] and [23]. The facility is aimed at investigating the flow around simple nozzle geometries as well as turbine blade cascades and it is designed to operate with fluorketone Novec^{TM} 649 ($CF_3CF_2C(O)CF(CF_3)_2$).

Despite the efforts done by research groups from all over the world, that are finally opening a window onto the unknowns of non-ideal flows [24–26], a large number of questions still remains unanswered. Certainly, this calls for the development of numerical tools that may used to foster the investigation of NICFD flows. Nowadays there exists only a few Computational Fluid Dynamics (CFD) tools which are capable of dealing with non-ideal flows. Indeed, the vast majority of numerical solvers soundly rely on the general assumption of that the fluid obeys the ideal gas law. Given that this latter assumption holds in most circumstances and applications for which a CFD solver is designed, the performances of the software can be optimized by introducing a set of simplifications that hasten the execution of the program and slim down the encoding phase. Indeed, to model the thermodynamics with a reasonable level of accuracy one must include accurate—but unfortunately complex and computationally expensive—EoS. Therefore, to deal with non-ideal flows the structure of a typical CFD solver must be largely modified or possibly even re-designed. Due to the demanding operating conditions which make experimental investigations rather complicated to carry out, numerical tools represent one of the most powerful resource that researchers and engineers may use to investigate NICFD flows. On the other hand, due to the lack of experimental data in the open literature, no NICFD CFD code was ever validated against measurements in the NICFD regime. The accuracy of the simulations, which amplifies the *unknown* accuracy of the underlying thermodynamic models, is therefore highly questionable.

1.2 Research Overview

This dissertation is mainly focused on the numerical investigation of non-ideal flows and it presents the latest advancements for NICFD applications.

The first part of the thesis is devoted to the investigation of shock-waves in the NICFD regime. A new unprecedented physical phenomenon is predicted, namely, the so-called non-ideal oblique shock waves. The variation of the properties of a complex fluid flowing across an oblique shock is analyzed with respect to the upstream thermodynamic state. In the limit of shocks of vanishing intensity, the investigation reveals the existence of a non-ideal effect that produces a Mach number increase upon compression. This advancement builds on the results presented in [27]. In the referenced work, the authors considered steady isentropic flows of fluids in their dense gas regime and they predicted that the Mach number may increase, rather than decrease, with density or pressure if the specific heats of the fluid are sufficiently large. Nevertheless, in this dissertation a detailed discussion is provided for shock-waves, though in the limit of vanishing intensity, along with consideration about their mechanical stability.

In the second part of this dissertation, the first-ever experimental accuracy assessment of a NICFD fluid model is presented. The NICFD model is implemented within the SU2 suite, an open-source platform designed to solve multi-physics Partial Differential Equation (PDE) problems and PDE-constrained optimization problems [28, 29]. In the present thesis, SU2 was generalised, in collaboration with researchers from TU Delft and Stanford University, to deal with a non-ideal, fully turbulent, solver [30–32]. To carry out the assessment, a set of reference test cases including non-ideal supersonic flows of siloxane fluid MDM (Octamethyltrisiloxane, $C_8H_{24}O_2Si_3$) was designed. The test cases are representative of applications of practical interest, more precisely, of supersonic flows within the turbine vanes of Organic Rankine Cycle (ORC) power systems.

In the third part of this dissertation, a first attempt to calibrate the Peng-Robinson EoS based on real experimental data collected at Politecnico di Milano is presented. The inference process takes advantage of a standard Bayesian approach which relies on a Markov Chain Monte Carlo method. Though the procedure does not succeed in providing information about the parameters' true value, it reveals either a potential epistemic uncertainty underlying the computational model of the test section (including a possible epistemic uncertainty affecting the state-of-the-art fluid model for complex compound) or a biased experimental measurement process.

In last part of the thesis, the NICFD CFD solver is exploited to carry out numerical investigations of diverse fluid problems of interest for ORC applications. In particular, the typical fish-tail shock pattern found at the trailing edge of turbine blades is investigated, to expose the possible non-ideal effects and to assess the influence of thermodynamic conditions on the shock properties. Secondly, the time-response of pressure probes is investigated for MDM fluid at either ideal and non-ideal con-

ditions. The role of non-idealities over the time-response of pressure probes is revealed and highlighted. Eventually, the non-ideal CFD solver is coupled to a virtual schlieren image generator, to predict the expected schlieren images of the density field of the flow developed in an experiment.

1.3 Thesis Outline

Chapter 2 presents a brief overview of the fundamental concepts supporting non-ideal Compressible-Fluid Dynamics. First, the relations that bound the thermodynamic variables among each others are introduced and specified according to diverse physical assumptions. Depending on these hypotheses, a set of well-known fluid models is presented and discussed. In the second part of the chapter, weak oblique shocks are investigated in the non-ideal regime. These latter are classical compression shock waves of finite amplitude where a non-ideal oblique Mach number increase is observed [33]. The non-ideal increase of the flow Mach number is arguably relevant in applications where oblique shock waves are either intentionally formed (e.g. engine intake ramps) or are present as a byproduct of the supersonic flow expansion (e.g. fish-tail shocks in turbine nozzle vanes, over/under-expanded jet from nozzle exit) [34, 35].

Chapter 3 reports the description of the steps required to extend an ideal CFD solver to non-ideal flows. Technical details about the modifications needed to accommodate the more complex EoS are provided. The considered NICFD CFD solver (SU2) is verified against very simple flow configurations for which it is possible to compute the analytic solution. The considered test cases include: the unsteady propagation of a shock within an open-end pipe and into an infinite acting reservoir, a steady supersonic flow over a double-wedged geometry, to generate a complex shock pattern, a non-classical rarefaction shock wave. Eventually, indications about the reliability of the numerical implementation and about solver capabilities are provided.

Chapter 4 reports the first-ever experimental assessment of the accuracy of a flow simulation software for non-ideal Compressible-Fluid Dynamics flows. Indeed, for the first time the capabilities of a non-ideal CFD solver are assessed against experimental measurements. The data used for comparison were collected using the TROVA test-rig at Politecnico di Milano. The test set includes flow configurations of practical interest for renewable energy applications. More precisely, experiments aim at reproducing the supersonic flow of MDM within turbine vanes in ORC power production systems. The assessment takes advantage of a non-intrusive polynomial chaos-based technique which was used to forward propagate the experimental uncertainties through the solver. The error bars resulting from this analysis are limited to very small values, pointing out the robustness and the predictive character of the numerical tool.

Chapter 5 introduces a Bayesian framework for the inference of complex fluid properties. In particular, the framework is a proof-of-concept for evaluating the potential analysis which could be done on non-ideal flows, and to draw the attention to the potential uncertainties underlying state-of-the-art fluid models. This latter statement includes both aleatoric and epistemic uncertainties. The framework is tailored on the TROVA test-rig. Synthetic data are generated and exploited to assess the reliability of the framework, and to provide an insight on its potential with respect to non-ideal flows.

Chapter 6 deals with exemplary applications of NICFD flows of practical interest. The NICFD CFD solver from SU2 is exploited to carry out investigations of compressible-fluid flows involving complex fluids. First, the numerical solver is used to conduct an analysis of the typical fish-tail shock pattern generated at the turbine blade trailing edge, in ORC turbomachinery applications. The analysis aims at investigating possible non-ideal effects across oblique shock waves and the influence of thermodynamic conditions on the shock properties. Secondly, the dynamics of pressure probes for high frequency measurements is investigated for fluids in the non-ideal regime. In particular, the time-response is reconstructed with respect to step perturbations on the pressure field. This analysis is carried out to assess the effects of non-idealities on the time-response of devices typically employed to measure pressure fluctuations past an ORC turbine rotor. Finally, the non-ideal CFD solver is used to reconstruct the flow-field around exemplary geometrical configurations. The solution is postprocessed to generate the expected schlieren image of the test section. The procedure may provide an additional way to compare numerical results against experimental measurements.

References

[1] *Key World Energy Statistics 2017*. International Energy Agency, 2017, p. 97. DOI: https://doi.org/https://doi.org/10.1787/key_energ_stat-2017-en. URL: https://www.oecd-ilibrary.org/content/publication/key_energ_stat-2017-en.

[2] *World Energy Outlook 2017*. International Energy Agency, 2017, p. 763. DOI: https://doi.org/https://doi.org/10.1787/weo-2017-en. URL: https://www.oecd-ilibrary.org/content/publication/weo-2017-en.

[3] Shell. *World Energy Model: a view to 2100*. 2017.

[4] *World Energy Assessment: Energy and the Challenge of Sustainability*. United Nations, 2000.

[5] V. Dostal, P. Hejzlar, and M. Driscoll. "The supercritical carbon dioxide power cycle: comparison to other advanced power cycles". In: *Nuclear technology* 154.3 (283-301). DOI: 10.1002/fld.762.

[6] U. Drescher and D. Bruggeman. "Fluid selection for the Organic Rankine Cycle (ORC) in biomass power and heat plants". In: *Applied Thermal Engineering* 27.1 (2007), pp. 223–228.

[7] W. Lang, R. Almbauer, and P. Colonna. "Assessment of Waste Heat Recovery for A Heavy-duty Truck Engine Using An ORC Turbogenerator". In: *Journal of Engineering for Gas Turbines and Power-Transactions of the ASME* 135.4 (2013), pp. 042313–1–10. DOI: 10.1115/1.4023123. URL: http://gasturbinespower.asmedigitalcollection.asme.org/data/Journals/JETPEZ/926648/gtp_135_4_042313.pdf.

[8] S. Quoilin, M. V. D. Broek, S. Declaye, P. Dewallef, and V. Lemort. "Techno-economic survey of Organic Rankine Cycle (ORC) systems". In: *Renewable and Sustainable Energy Reviews* 22.0 (2013), pp. 168–186. ISSN: 1364-0321. DOI: 10.1016/j.rser.2013.01.028.

[9] E. Casati, S. Vitale, M. Pini, G. Persico, and P. Colonna. "Centrifugal Turbines for Mini-Organic Rankine Cycle Power Systems". In: *Journal of Engineering for Gas Turbines and Power* 136 (2014).

[10] E. Reverchon and P. Pallado. "Hydrodynamic modeling of the RESS process". In: *J. of Supercritical Fluids* 9.4 (1996), pp. 216–221.

[11] B. Subramaniam, R. A. Rajewski, and K. Snavely. "Pharmaceutical processing with supercritical carbon dioxide". In: *J. Pharm. Sci.* 86.8 (1997), pp. 885–890.

[12] X.-Y. Sun, T.-J. Wang, Z.-W. Wang, and Y. Jin. "The characteristics of coherent structures in the rapid expansion flow of the supercritical carbon dioxide". In: *J. of Supercritical Fluids* 24.3 (#dec# 2002), pp. 231–237. ISSN: 08968446. DOI: 10.1016/S0896-8446(02)00084-0. URL: http://linkinghub.elsevier.com/retrieve/pii/S0896844602000840.

[13] T. Ito, Y. Otani, and H. Inomata. "Performance of air filters cleaned by supercritical carbon dioxide". In: *Sep. Purif. Technol.* 40.1 (2004), pp. 41–46. DOI: 10.1016/j.seppur.2004.01.002.

[14] A. Spinelli, M. Pini, V. Dossena, P. Gaetani, and F. Casella. "Design, Simulation, and Construction of a Test Rig for Organic Vapours". In: *ASME J. Eng. Gas Turb. Power* 135 (2013), p. 042303.

[15] A. Guardone, A. Spinelli, and V. Dossena. "Influence of Molecular Complexity on Nozzle Design for an Organic Vapor Wind Tunnel". In: *ASME J. Eng. Gas Turb. Power* 135 (2013), p. 042307.

[16] T. Mathijssen, M. Gallo, E. Casati, N. R. Nannan, C. Zamfirescu, A. Guardone, and P. Colonna. "The flexible asymmetric shock tube (FAST): a Ludwieg tube facility for wave propagation measurements in high-temperature vapours of organic fluids". In: *Exp. Fluids* 56.10 (2015), pp. 1–12.

[17] P. Colonna, A. Guardone, N. R. Nannan, and C. Zamfirescu. “Design of the dense gas flexible asymmetric shock tube”. In: *ASME Journal of Fluids Engineering* 130 (2008).

[18] A. J. Head, C. De Servi, E. Casati, M. Pini, and P. Colonna. “Preliminary design of the ORCHID: a facility for studying non-ideal compressible fluid dynamics and testing ORC expanders”. In: *ASME Turbo Expo 2016*. GT2016-56103. 2016.

[19] A. Uusitalo, J. Honkatukia, and T. Turunen-Saaresti. “Evaluation of a small-scale waste heat recovery organic Rankine cycle”. In: *Applied Energy* 192 (2017), pp. 146–158.

[20] T. Turunen-Saaresti, A. Uusitalo, and J. Honkatukia. “Design and testing of high temperature micro-ORC test stand using Siloxane as working fluid”. In: *Journal of Physics: Conference Series* 821.1 (2017), p. 012024.

[21] F. J. D. Galiana, A. P. S. Wheeler, J. Ong, and C. A. M. Ventura. “The effect of dense gas dynamics on loss in ORC transonic turbines”. In: *Journal of Physics: Conference Series* 821.1 (2017), p. 012021.

[22] F. Reinker, K. Hasselmann, S. der Wiesche, and E. Y. Kenig. “Thermodynamics and Fluid Mechanics of a Closed Blade Cascade Wind Tunnel for Organic Vapors”. In: *Journal of Engineering for Gas Turbines and Power* 138 (2016), p. 052601.

[23] F. Reinker, E. Y. Kenig, M. Passmann, and S. der Wiesche. “Closed Loop Organic Wind Tunnel (CLOWT): Design, Components and Control System”. In: *Energy Procedia* 129.Supplement C (2017), pp. 200–207.

[24] A. Spinelli, G. Cammi, S. Gallarini, M. Zocca, F. Cozzi, P. Gaetani, V. Dossena, and A. Guardone. “Experimental evidence of non-ideal compressible effects in expanding flow of a high molecular complexity vapour”. In: *Experiments in Fluids* 59.8 (July 2018), p. 126.

[25] A. Spinelli, G. Cammi, M. Zocca, S. Gallarini, F. Cozzi, P. Gaetani, V. Dossena, and A. Guardone. “Experimental observation of non-ideal expanding flows of Siloxane MDM vapor for ORC applications”. In: *Energy Procedia* 129 (2017), pp. 1125–1132.

[26] A. Spinelli, F. Cozzi, G. Cammi, M. Zocca, P. Gaetani, V. Dossena, and A. Guardone. “Preliminary characterization of an expanding flow of siloxane vapor MDM”. In: *Journal of Physics: Conference Series* 821.1 (2017), p. 012022. URL: `http://stacks.iop.org/1742-6596/821/i=1/a=012022`.

[27] M. S. Cramer and L. M. Best. “Steady, isentropic flows of dense gases”. In: *Phys. Fluids A* 3.4 (1991), pp. 219–226.

[28] F. Palacios, M. R. Colonno, A. C. Aranake, A. Campos, S. R. Copeland, T. D. Economon, A. K. Lonkar, T. W. Lukaczyk, T. W. R. Taylor, and J. J. Alonso. “Stanford University Unstructured (SU^2): An open-source integrated computational environment for multi-physics simulation and design”. In: *AIAA Paper 2013-0287* 51st AIAA Aerospace Sciences Meeting and Exhibit (Jan. 2013).

[29] T. D. Economon, D. Mudigere, G. Bansal, A. Heinecke, F. Palacios, J. Park, M. Smelyanskiy, J. J. Alonso, and P. Dubey. “Performance optimizations for scalable implicit RANS calculations with SU2”. In: *Computers & Fluids* 129 (2016), pp. 146–158. ISSN: 0045-7930. DOI: `http://dx.doi.org/10.1016/j.compfluid.2016.02.003`. URL: `http://www.sciencedirect.com/science/article/pii/S0045793016300214`.

[30] S. Vitale, G. Gori, M. Pini, A. Guardone, T. D. Economon, F. Palacios, J. J. Alonso, and P. Colonna. “Extension of the SU2 open source CFD code to the simulation of turbulent flows of fluids modelled with complex thermophysical laws”. In: *22nd AIAA Computational Fluid Dynamics Conference*. AIAA Paper 2760. 2015.

[31] G. Gori, A. Guardone, S. Vitale, A. Head, M. Pini, and P. Colonna. “Non-Ideal Compressible-Fluid Dynamics Simulation with SU2: Numerical Assessment of Nozzle and Blade Flows for Organic Rankine Cycle Applications”. In: *3rd International Seminar on ORC Power Systems*. Brussels, Belgium, Oct. 2015.

[32] M. Pini, S. Vitale, P. Colonna, G. Gori, A. Guardone, T. Economon, J. Alonso, and F. Palacios. “SU2: the Open-Source Software for Non-ideal Compressible Flows”. In: vol. 821. 1. 2017, p. 012013.

[33] G. Gori, D. Vimercati, and A. Guardone. “Non-ideal compressible-fluid effects in oblique shock waves”. In: *Journal of Physics: Conference Series* 821.1 (2017), p. 012003. URL: `http://stacks.iop.org/1742-6596/821/i=1/a=012003`.

[34] D. Vimercati, G. Gori, A. Spinelli, and A. Guardone. “Non-ideal effects on the typical trailing edge shock pattern of ORC turbine blades”. In: *Energy Procedia* 129.Supplement C (2017), pp. 1109–1116.

[35] G. Gori, D. Vimercati, and A. Guardone. “A Numerical Investigation of Oblique Shock Waves in Non-Ideal Compressible-Fluid Flows”. In: *31st International Symposium on Shock Wavess*. Nagoya, Japan, 2017.

CHAPTER 2

NON-IDEAL COMPRESSIBLE-FLUID DYNAMICS

2.1 Introduction

This chapter provides a brief summary of the fundamental concepts underlying Non-Ideal Compressible-Fluid Dynamics (NICFD). NICFD focuses on the investigation of a well-determined region of the thermodynamic state space, the *non-ideal* region, where the ideal gas law does not apply. It is worth to stress out that the term NICFD refers to a particular regime of the flow i.e., a particular thermodynamic state, and not to the fluid itself.

The characterisation of non-ideal compressible-fluid flows is not only of theoretical interest, but it is also relevant to applications such as in Organic Rankine Cycle machineries (ORC), supercritical CO_2 power systems, turbogenerators, refrigerators and many others, see reference [1–4]. Indeed, well-established and accurate thermodynamic models predict that several fluids currently employed in industrial processes feature non-ideal effects in the single-phase vapor region. Prominent examples are hydrocarbons, fluorocarbons and siloxanes used as working fluids in ORC power systems. Related phenomena of practical interest include, for instance, a decrease of the flow Mach number in supersonic expansions [5], the non-ideal evolution of the Mach number in diabatic supersonic nozzle flows [6] and the increase of the flow Mach number across oblique shock waves [7], which will be detailed later in this chapter.

The goal of this chapter is to provide a very general presentation of the fundamental concepts of classical thermodynamics (Sec. 2.2). Special attention is devoted the definition of the relations that bound the thermodynamic variables and rule out the evolution of the fluid state in time. A set of exemplary fluid models, which will be extensively used throughout this dissertation, are then recalled (Sec. 2.3). This first part is required to introduce the most relevant features characterizing NICFD flows.

2.2 Classical Thermodynamics

Classical thermodynamics relies on the definition of essential concepts such as *property* or *process*. Properties are macroscopic measurable attributes that define the state of the system while processes rule out the evolution of such state in time. To this extent, thermodynamics may be seen as a generalization of the topics traditionally covered in classical mechanics [8]. According to [9], given a system in a stable equilibrium state, whereas the system contains a simple monocomponent fluid, and given that the volume V of the domain is the one and only parameter, it is possible to define a *fundamental function* $\mathcal{S}$ for the entropy which reads

$$\mathcal{S} = \mathcal{S}(E, V, n) , \tag{2.1}$$

where n is the number of moles contained in the control volume. $\mathcal{S}$ benefits from the following relevant properties:

- It is homogeneous of degree one with respect to all its variables

- It is analytic in each of its variables and therefore differentiable to all orders, at least within the range of admissibility of the variables.
- It is strictly monotone with respect of energy E
- It is superadditive i.e., $\mathcal{S}(a+b) \geq \mathcal{S}(a)+\mathcal{S}(b)$

The actual functional dependence of S on E and V varies from system to system. Since $\mathcal{S}$ is strictly monotone with respect to E, it is possible to invert the relation, to provide an alternative representation of the state of the system

$$\mathcal{E} = \mathcal{E}(S,V,n) , \tag{2.2}$$

Thanks to the homogeneity property, these two relations can be expressed in terms of specific quantities (per unit mass). In particular:

$$s = \frac{\mathcal{S}}{n\mathcal{M}} = \frac{1}{n\mathcal{M}}\mathcal{S}\left(\frac{E}{n\mathcal{M}}, \frac{V}{n\mathcal{M}}, \frac{1}{\mathcal{M}}\right) = s(e,v) , \tag{2.3}$$

$$e = \frac{\mathcal{E}}{n\mathcal{M}} = \frac{1}{n\mathcal{M}}\mathcal{E}\left(\frac{S}{n\mathcal{M}}, \frac{V}{n\mathcal{M}}, \frac{1}{\mathcal{M}}\right) = e(e,v) , \tag{2.4}$$

where $\mathcal{M}$ is the molecular weight.

Since $\mathcal{S}$ is differentiable to all orders, it is possible to introduce its partial derivatives, to compute thermodynamic intensive parameters:

$$\frac{\partial e(s,v)}{\partial s} = T , \qquad \frac{\partial e(s,v)}{\partial v} = -P , \tag{2.5}$$

The intensive quantities temperature T and pressure P are thus defined from the fundamental function. Each of the partial derivatives constitutes a relation among the thermodynamic properties and it is referred to as an Equation of state (EoS). The EoS are not independent from each other as the Schwartz theorem on the equality of mixed partial derivatives must eventually apply.

$$\frac{\partial T}{\partial v} \equiv -\frac{\partial P}{\partial s} , \tag{2.6}$$

Eq. 2.6 is known as the *compatibility condition* among two different EoS.

In practical applications, the EoS are generally unknown and the relations bounding the properties of the fluid are to be established, starting from the physical modeling of the fluid of interest. These properties include pressure, temperature, viscosity, thermal conductivity, volume and so on. The EoS may be theoretical models, resulting from a mathematical description of the molecular structure of the gas, or they may be semi-empirical models, such as multi-parameter equations, calibrated according to experimental measurements.

2.3 Fluid models

The definition of an appropriate set of EoS is key to obtain an accurate description of the system thermodynamics. In order to simplify the EoS, one could decide to neglect part of the underlying physics thus imposing limits to the validity of the model. For instance, the assumptions standing underneath the ideal gas model are valid in the limit of a dilute gas, and they start to fail in the close proximity of the saturation curve and the critical point.

The kinetic theory of gases considers a gas as a large set of molecules in a continuous and rapid motion within a control volume. The motion of such particles is largely characterized by randomness, which is caused by their unpredictable interaction with other particles or with the boundaries of the domain. If the number of molecules is sufficiently large, the macroscopic properties of a gas can be approximated in terms of statistical quantities. The different assumptions that one may account for, for instance about the possible interactions among particles or about the structure of the atoms, will eventually lead to different models. In the following, the polytropic Ideal Gas, the polytropic van der Waals and the polytropic Peng-Robinson fluid models are presented. Hereinafter, a gas will be indicated as a polytropic if the energy is a linear function of the temperature T i.e., if the specific heat at constant volume in the dilute gas limit (c_{v_∞} = const). For the sake of completeness, it worth to mention that a model for the specific heat law $c_{v_\infty}(T)$ can be obtained from experimental data or, for example, from the equipartition principle of classical statistical mechanics (see [9]).

Besides the mentioned polytropic models, some of the results presented in the dissertation were obtained using a multiparameter EoS based on the Helmoltz potential [10], which currently represents the state-of-the-art. Such high fidelity EoS models a non-polytropic gas and it is not detailed in this dissertation due to its high complexity and because it doesn't add any further insight about the qualitative behavior of non-ideal flows. The reader is referred to the referenced work for further details.

2.3.1 The Ideal Gas Law

The polytropic EoS for *Ideal Gas* (PIG) is generally derived under the following main hypothesis:

- Particles belonging to the same specie have equal properties.
- Particles are perfectly spherical.
- The only interaction among particles consist in perfectly elastic collisions.
- The number of molecules in the control volume is statistically meaningful.
- The average distance between particles is large if compared to their size.

This set of hypotheses defines the limits of the dilute gas regime and they yield the well-know equations:

$$P(T,v) = \frac{RT}{v}, \tag{2.7a}$$

$$e(T,v) = e_{\text{ref}} + c_v (T - T_{\text{ref}}), \tag{2.7b}$$

$$s(T,v) = s_{\text{ref}} + c_v \ln \frac{T}{T_{\text{ref}}} + R \ln \frac{v}{v_{\text{ref}}}, \tag{2.7c}$$

the equations were reported as a function of temperature and specific volume (note that for an ideal gas the EoS for the energy depends on the temperature only) but, thanks to their own properties, they may be inverted and re-cast in other forms. Reference values e_{ref} and s_{ref} appear in the EoS: these are usually set w.r.t. a certain state of the system.

It is well known that, for a polytropic gas, the specific heat at constant volume c_v and the specific heat at constant pressure c_p may be defined as follows

$$c_v = \frac{1}{\gamma - 1} R \qquad c_p = \frac{\gamma}{\gamma - 1} R, \tag{2.8}$$

where the specific heat ratio is defined as $\gamma \doteq c_p / c_v$ and it can be related to the degrees of freedom f of the molecule through the relation

$$\gamma = 1 + \frac{2}{f}, \tag{2.9}$$

We observe that $f = 3$ for a mono-atomic gas (the 3 translational directions), and it increases with the molecular structure complexity, reducing γ to the limit of 1.

The PIG relies on a set of assumptions that are reasonable in a wide portion of the thermodynamic region. Nevertheless, as the state of the gas approaches the saturation curve, in the close proximity of the critical point, the inter-molecular interactions start gaining relevance. The assumptions on to which the PIG law relies does no longer apply and, consequently, the model fails.

2.3.2 The polytropic van der Waals Fluid Model

When the density of the gas reaches a point such that the average distance between particles is comparable to their size, additional physical effects must be taken into account. In particular, the intensity of the inter-molecular forces a and the covolume b are fluid-dependent parameters that came into play when the dilute gas limit assumption is relaxed. Moreover, as temperature increases, additional vibrating modes starts being excited thus activating idle energy levels which yield an increase of the heat capacity of the fluid.

In the last decades, many mathematical models where proposed to describe the thermodynamics of a gas in a dense regime. The van der Waals model (vdW) [11] includes the effects of the attractive inter-molecular forces and of the covolume.

$$P(T,v) = \frac{RT}{v-b} - \frac{a}{v^2}, \tag{2.10a}$$

$$e(T,v) = e_{\text{ref}} + \frac{RT}{\gamma-1} - \frac{a}{v}, \tag{2.10b}$$

$$s(T,v) = s_{\text{ref}} + \frac{R}{\gamma-1}\ln T + R\ln(v-b), \tag{2.10c}$$

The parameters a and b are related to molecular structure of the gas. According to the vdW model, they can be computed as follows:

$$a = \frac{27}{64}\frac{R^2T_{\text{cr}}^2}{P_{\text{cr}}} \qquad b = \frac{1}{8}\frac{RT_{\text{cr}}}{P_{\text{cr}}}, \tag{2.11}$$

where T_{cr} and P_{cr} are the critical temperature and pressure, respectively.

2.3.3 The polytropic Peng-Robinson Fluid Model

Peng and Robinson proposed their model for the first time in 1976 [12]. The model is relatively simple but yet able to predict the behavior of complex fluids with a reasonable level of accuracy, at least for the developments presented in this work. Indeed, the EoS depend on a limited number of parameters and their structure can be easily accessed. Basically, Peng and Robinson modified the (*Soave-Redlich-Kwong*) EoS to improve the prediction of liquid density values, vapor pressures, and equilibrium ratios. Briefly, the polytropic Peng-Robinson (PR) model can be conveniently written as

$$P(T,v) = \frac{RT}{v-b} - \frac{a\alpha^2(T,\omega)}{v^2+2bv-b^2}, \tag{2.12a}$$

$$e(T,v) = e_{\text{ref}} + \frac{RT}{\gamma-1} - \frac{a\alpha(T,\omega)(k+1)}{b\sqrt{2}}\tanh^{-1}\frac{b\sqrt{2}}{v+b}, \tag{2.12b}$$

$$s(T,v) = s_{\text{ref}} + \frac{R}{\gamma-1}lnT + R\ln(v-b) - \frac{a\alpha(T,\omega)k}{b\sqrt{2TT_{\text{cr}}}}\tanh^{-1}\frac{b\sqrt{2}}{v+b}, \tag{2.12c}$$

ω is the *acentric factor*, a parameter that depends on the molecular structure whereby $\alpha(T,\omega)$ is a function that further model the inter-molecular interactions as forces depending on the temperature T. According to the original formulation, the parameters are a and b are temperature independent and they are defined as follows:

$$a = 0.45724\frac{(RT_{\text{cr}})^2}{P_{\text{cr}}} \qquad b = 0.0778\frac{RT_{\text{cr}}}{P_{\text{cr}}}, \tag{2.13}$$

The $\alpha(T)$ function is instead expressed as follow

$$\alpha(T,\omega) = \left[1 + k\left(1 - \sqrt{\frac{T}{T_{\text{cr}}}}\right)\right], \tag{2.14}$$

where k is defined as $k = 0.37464 + 1.54226\omega - 0.26992\omega^2$.

2.4 Non-Ideal Compressible-Fluid Flows

The dynamics of compressible-fluid flows is identified by the so-called *Fundamental Derivative of Gasdynamics* Γ [13], a parameter to classify the qualitative behavior of fluid flows in many contexts. According to [13], it is possible to define the Γ as

$$\Gamma \equiv \frac{c^4}{2v^3}\left(\frac{\partial^2 v}{\partial P^2}\right)_s, \tag{2.15}$$

where c is the speed of sound

$$c^2 \equiv \left(\frac{\partial P}{\partial \rho}\right)_s. \tag{2.16}$$

Conventional treatments of gasdynamics assume, either explicitly or implicitly, that $\Gamma > 1$ in the dilute gas limit. For the PIG model, it can be proved that $\Gamma = (\gamma+1)/2$, therefore Γ is always a constant larger than unity. From the qualitative point of view, the gasdynamic behavior of any fluid with constant $\Gamma > 1$ resembles that of ideal gases [14]. As mentioned, there exist fluids endowed with a non-ideal gasdynamic behavior in a finite vapor-phase region, in close proximity of the saturation curve [13, 15–18]. In the non-ideal regime and in the close proximity of the vapor-liquid saturation curve, the fluid can show values of Γ smaller than one or even negative. It is standard practice to distinguish between the cases $\Gamma \leq 0$ and $0 < \Gamma \leq 1$: the former case refers to non-classical gasdynamics, as opposed to classical gasdynamics for which $\Gamma > 0$. Clearly, the presence and the extension of the non-ideal and non-classical region depend on the fluid model employed to model the thermodynamics.

Therefore, through the parameter Γ it is possible to identify the regime of the flow:

- $\Gamma \geq 1$ *ideal* regime.
- $0 \leq \Gamma < 1$ *non-ideal* regime.
- $\Gamma < 0$ *non-classical* regime.

Fig. 2.1 reports the saturation curve of siloxane MDM fluid (Octamethyltrisiloxane, $C_8H_{24}O_2Si_3$) on the $P - v$ plane, computed using the Span-Wagner [10] EoS included in the Fluidprop library. The $\Gamma = 1$ and $\Gamma = 0$ contour lines are also reported.

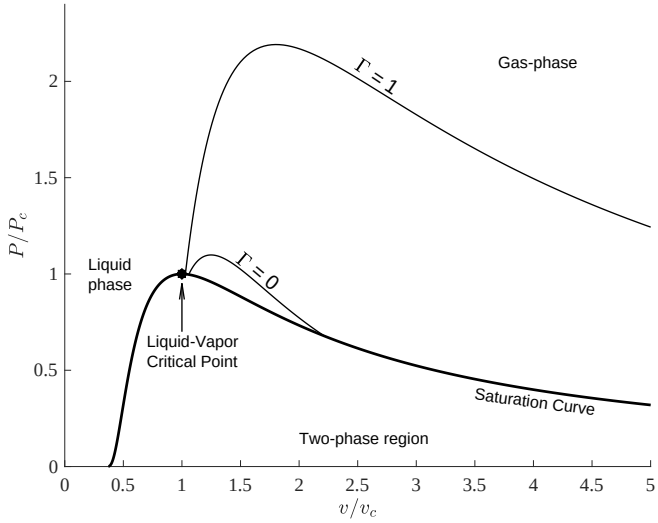

Figure 2.1: *p-v* diagram of a fluid featuring a non-ideal region. The liquid-vapor saturation curve (bold line) and the $\Gamma = 1$ and $\Gamma = 0$ contour lines are plotted;

The non-ideal and the non-classical regions lie in between the liquid-vapor saturation curve and the $\Gamma = 1$ and $\Gamma = 0$ contour lines. Within the non-classical limit, unconventional phenomena such as expansion shocks, isentropic compression fans, split shocks and composite waves are allowed, see for instance references [13, 18–23]. The so-called non-classical phenomena are caused by negative non-linearities (Γ changing its sign), and the most striking example is the admissibility of expansion shocks and composite waves. It must be noticed, though, that experimental evidence of negative nonlinearities is still missing at present, thus leaving the existence of non-classical phenomena an open question in fluid mechanics. In this respect, recent advancements indicate the possibility of observing negative nonlinearities in common substances (other than Bethe–Zel'dovich–Thompson fluids) due to critical-point anomalies [24, 25].

The compressibility factor Z is a parameter that quantifies how much the flow departs from the ideal regime. Z is defined as follows:

$$Z = \frac{Pv}{RT}, \tag{2.17}$$

For a flow in an ideal regime the compressibility factor is equal (or close) to unity; as the thermodynamics departs from ideality Z decreases. In this thesis, we will mostly deal with non-ideal regimes, limiting the discussion of non-classical flows to just one exemplary test case, to assess the reliability of a numerical solver in this unusual regime.

2.5 Thermal stability of chemical compounds

The non-ideal region ($\Gamma < 1$) is generally found in the close proximity of the liquid-vapor saturation curve, at values of pressure and temperature in the order of the critical ones. Such extreme conditions may be beyond the thermal stability point of the compound which, therefore, may undergo a chemical decomposition. Namely, the thermal stability is the capacity of the molecules to sustain high temperatures. Indeed, as the temperature increases so does the vibrating energy of the molecules. As pointed out by [26], chemical bonds have a finite strength that puts an upper limit on the vibrating energy that molecules may posses without bond rupture. As the temperature crosses the stability threshold, the molecule decomposes into a number of simpler elements. Therefore, though some compounds may be endowed (theoretically) with a non-ideal region, they may not be able to experience non-ideal effects due to an early chemical decomposition. Indeed, as the state of the fluid approaches the non-ideal region, the stability point is reached and the compound decomposes in a mixture of simpler substances with different properties and, most likely, not even endowed with a non-ideal behavior.

2.6 Conclusions

In this chapter, we provided a brief discussion of the thermodynamics of non-ideal flows. The fundamentals of thermodynamics were recalled, to introduce the EoS as functions that relate the properties of the fluid. These properties define the thermodynamic state which evolve in time through a particular process. Then a set of well known and widely used thermodynamic fluid model were introduced and detailed. In particular, the polytropic ideal gas model (PIG), the van polytropic der Waals model (vdW) and the Peng-Robinson (PR) model are described. Eventually, non-ideal compressible-fluid flows properties were presented and discussed. The definition of the fundamental derivative of gasdynamic Γ is recalled, to provide a criteria to classify the flow regime. Namely, $\Gamma > 1$ is typical of ideal flows while $\Gamma < 1$ points out a non-ideal regime. $\Gamma < 0$ identifies the non-classical regime, where an inverted thermodynamic behavior is expected. This dissertation is mainly devoted to the investigation of flows of fluid in the non-ideal regime.

References

[1] P. Colonna, N. R. Nannan, and A. Guardone. "Multiparameter equations of state for siloxanes:[(CH 3) 3-Si-O 1/2] 2-[O-Si-(CH 3) 2] i= 1,. . . , 3, and [O-Si-(CH 3) 2] 6". In: *Fluid Phase Equilib.* 263.2 (2008), pp. 115–130.

[2] P. Congedo, C. Corre, and P. Cinnella. "Numerical investigation of dense-gas effects in turbomachinery". In: *Comput. & Fluids* 49.1 (2011), pp. 290–301.

[3] A. Wheeler and J. Ong. "The role of dense gas dynamics on Organic Rankine Cycle turbine performance". In: *J. Eng. Gas Turbines Power* 135.10 (2013), p. 102603.

[4] P. Colonna, E. Casati, C. Trapp, T. Mathijssen, J. Larjola, T. Turunen-Saaresti, and A. Uusitalo. "Organic Rankine Cycle Power Systems: From the Concept to Current Technology, Applications, and an Outlook to the Future". In: *J. Eng. Gas Turb. Power* 137.10 (2015).

[5] M. S. Cramer and L. M. Best. "Steady, isentropic flows of dense gases". In: *Phys. Fluids A* 3.4 (1991), pp. 219–226.

[6] G. H. Schnerr and P. Leidner. "Diabatic supersonic flows of dense gases". In: *Phys. Fluids A* 3.10 (1991), pp. 2445–2458.

[7] G. Gori, D. Vimercati, and A. Guardone. "Non-ideal compressible-fluid effects in oblique shock waves". In: *Journal of Physics: Conference Series* 821.1 (2017), p. 012003. URL: `http://stacks.iop.org/1742-6596/821/i=1/a=012003`.

[8] E. P. Gyftopoulos and G. P. Beretta. *Thermodynamics: foundations and applications*. Mineola (New York), Dover Publications, 2005. ISBN: 0-486-43932-1.

[9] H. B. Callen. *Thermodynamics and an introduction to thermostatistics*. 2nd ed. Wiley, 1985.

[10] M. Thol, F. H. Dubberke, E. Baumhögger, J. Vrabec, and R. Span. "Speed of Sound Measurements and Fundamental Equations of State for Octamethyltrisiloxane and Decamethyltetrasiloxane". In: *Journal of Chemical & Engineering Data* 62.9 (2017), pp. 2633–2648.

[11] J. D. van der Waals. "Over de Continuïteit van den Gas - en Vloeistoftoestand (on the continuity of the gas and liquid state)". PhD thesis. Leiden University, 1873.

[12] D. Y. Peng and D. B. Robinson. "A New Two-constant Equation of State". In: *Ind. Eng. Chem. Fundam.* 15 (1976), pp. 59–64.

[13] P. A. Thompson. "A fundamental derivative in gasdynamics". In: *Phys. Fluids* 14.9 (1971), pp. 1843–1849.

[14] P. A. Thompson. *Compressilbe Fluid Dynamics*. McGraw-Hill, 1988.

[15] H. A. Bethe. *The theory of shock waves for an arbitrary equation of state*. Technical paper 545. Office Sci. Res. & Dev., 1942.

[16] Y. B. Zel'dovich. "On the Possibility of Rarefaction Shock Waves". In: *Zh. Eksp. Teor. Fiz.* 4 (1946), pp. 363–364.

[17] K. C. Lambrakis and P. A. Thompson. "Existence of Real Fluids with a Negative Fundamental Derivative Γ". In: *Phys. Fluids* 15.5 (1972), pp. 933–935.

[18] P. A. Thompson and K. C. Lambrakis. "Negative Shock Waves". In: *J. Fluid Mech.* 60 (1973), pp. 187–208.

[19] M. S. Cramer and A. Kluwick. "On the Propagation of Waves Exhibiting Both Positive and Negative Nonlinearity". In: *J. Fluid Mech.* 142 (1984), pp. 9–37.

[20] M. S. Cramer and R. Sen. "Shock formation in fluids having embedded regions of negative nonlinearity". In: *Phys. Fluids* 29 (1986), pp. 2181–2191.

[21] M. S. Cramer and R. Sen. “Exact solutions for sonic shocks in van der Waals gases”. In: *Phys. Fluids* 30 (1987), pp. 377–385.

[22] R. Menikoff and B. J. Plohr. “The Riemann problem for fluid flow of real material”. In: *Rev. Mod. Phys.* 61(1) (1989), pp. 75–130.

[23] J. W. Bates and D. C. Montgomery. “Some numerical studies of exotic shock wave behavior”. In: *Phys. Fluids* 11.2 (1999), pp. 462–475. DOI: http://dx.doi.org/10.1063/1.869862. URL: http://scitation.aip.org/content/aip/journal/pof2/11/2/10.1063/1.869862.

[24] N. R. Nannan, A. Guardone, and P. Colonna. “Critical point anomalies include expansion shock waves”. In: *Physics of Fluids* 26.2, 021701 (2014). DOI: http://dx.doi.org/10.1063/1.4863555. URL: http://scitation.aip.org/content/aip/journal/pof2/26/2/10.1063/1.4863555.

[25] N. R. Nannan, C. Sirianni, T. Mathijssen, A. Guardone, and P. Colonna. “The admissibility domain of rarefaction shock waves in the near-critical vapour–liquid equilibrium region of pure typical fluids”. In: *Journal of Fluid Mechanics* 795 (May 2016), pp. 241–261. ISSN: 1469-7645. DOI: 10.1017/jfm.2016.197. URL: http://journals.cambridge.org/article_S002211201600197X.

[26] I. Johns, E. McElhill, and J. Smith. “Thermal Stability of organic compounds”. In: *Industrial & Engineering Chemistry Product Research and Development* 1.1 (1962), pp. 2–6.

CHAPTER 3

NON-IDEAL OBLIQUE SHOCK-WAVES

Part of the contents of this chapter appear in

G. Gori, D. Vimercati and A. Guardone, *Non-Ideal compressible-fluid effects in oblique shock waves*, Journal of Physics: Conference Series, Vol. 821, 2017

D. Vimercati, G. Gori and A. Guardone, *Non-ideal effects on the typical trailing edge shock pattern of ORC turbine blades*, Energy Procedia, Vol. 129, 2017

D. Vimercati, G. Gori and A. Guardone, *Non-ideal oblique shock waves*, Journal of Fluid Mechanics, Vol. 847, 2018

3.1 Introduction

In this chapter, we discuss non-ideal gasdynamic effects in steady oblique shock-waves, such as those generated by a supersonic steady stream over a wedge. These latter are classical compression shocks of finite amplitude where a non-ideal oblique Mach number increase is observed [1]. The wedge prescribes a flow deflection angle $\theta \leq \theta_{\max}$, which is realized by a planar shock of angle β. The shock originates from the corner and separates the domain into two uniform regions A and B, respectively upstream and downstream the discontinuity (see Fig. 3.1).

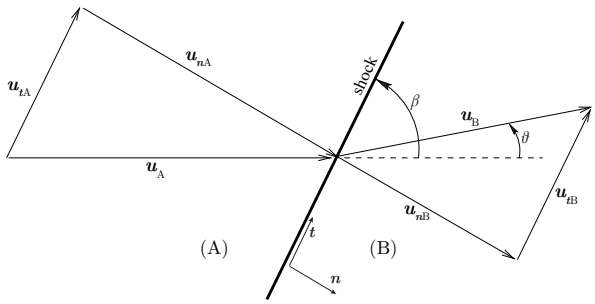

Figure 3.1: qualitative illustration of the local shock front. States A and B represent the pre-shock and post-shock states, respectively. The angles β and θ are the shock angle and the flow deviation angle, respectively, both computed with respect to the pre-shock flow direction. The reference frame is attached to the front and it is defined by the directions tangential and normal (**t** and **n**) to the shock;.

The condition $\theta = \theta_{max}$ corresponds to the maximum deflection that the flow can sustain across a planar attached shock wave. If $\theta > \theta_{\max}$, the shock wave detaches and the front is no longer planar, see [2].

In polytropic dilute gases, the variation of the thermodynamic and kinematic quantities across the shock (and the angle of the wave itself) are completely determined by only the Mach number of the flow ahead of the shock, relative to the shock front itself and the specific heat ratio γ.

When the behavior of the vapor strays the ideal gas law, a more or less noticeable dependence on the pre-shock thermodynamic state, say the values of the temperature and pressure, is also observed. Furthermore, there exist particular thermodynamic conditions of fluid ahead of the shock that result in a non-ideal Mach number increase in the post-shock state [1]. This peculiar kind of oblique shock waves, which are the focus of the following section, will be referred to as *non-ideal oblique shock waves*.

The definition of the thermodynamic admissibility region for non-ideal shock waves and the extension to flows of fluids exhibiting positive non-linearity can be found in [3]. Briefly, from the theoretical point of view non-ideal oblique shocks are possible for any flow in the regime $\Gamma < 1$, because the speed of sound no longer increases monotonically with increasing density along the shock adiabat.

Indeed, most of the features of shock waves, and of the nonlinear dynamics of compressible fluids in general, depends on the evolution of the speed of sound $c = \sqrt{(\partial P/\partial \rho)_s}$ along isentropic transformations. The fundamental derivative Γ can be expressed in terms of the sound-speed isentropic variation in non-dimensional form

$$\Gamma \equiv 1 + \frac{\rho}{c}\left(\frac{\partial c}{\partial \rho}\right)_s , \tag{3.1}$$

and this equation can be reformulated as

$$\left(\frac{\partial c}{\partial \rho}\right)_s \equiv \frac{c}{\rho}(\Gamma - 1) , \tag{3.2}$$

As mentioned, for perfect gases $\Gamma = (\gamma+1)/2 > 1$. Therefore, the speed of sound increases monotonically upon isentropic compression. Not surprisingly, this result is no longer valid for a flow in a non-ideal regime: the speed of sound can be non-monotonic with density along shock adiabats crossing thermodynamic regions where $\Gamma < 1$. According to this, and following the analysis of isentropic compressions by [4], it is straightforward to demonstrate that in the limit of shock waves of vanishing intensity, the Mach number can possibly increase across a compression wave, if $\Gamma < 1$.

To better explain this physical phenomenon, we first project the vector quantities onto an orthogonal reference system aligned with the shock, see Fig. 3.1. Therefore, vectors are decomposed in two components, one perpendicular (subscript n) and one parallel to the shock (subscript t).

The fact that the speed of sound may decrease across the shock implies that the Mach number of the flow parallel to the shock front increases (oblique shocks can be seen as normal shocks to which a uniform velocity field, parallel to the shock front, is

superposed). Such an increase can be large enough to compensate the decrease in the Mach number of the normal flow, which follows from mechanical stability conditions [5, 6]., thus resulting in an overall increase of the flow Mach number.

In the following, evidence that the non-monotone dependence of the speed of sound can result in the non-ideal increase of the flow Mach number across oblique shock waves is provided in details. The simple vdW model, which gives a qualitatively accurate description of the fluid behavior in the thermodynamic region of interest for this investigation, is employed.

3.2 Jump relations

We restrict our attention to single-phase flows of a mono-component fluid in which the effects of viscosity, heat conduction, chemical reactions and relaxation time can be neglected. The dynamics is thus governed by the well-known Euler equations of gasdynamics, in smooth regions of the flow field, along with the Rankine-Hugoniot conditions at jump discontinuities. Figure 3.2 shows a portion of the non-ideal thermodynamic region $\Gamma < 1$ for the polytropic vdW model of siloxane fluid MDM (Octamethyltrisiloxane, $C_8H_{24}O_2Si_3$), which will be largely considered throughout the this dissertation, together with the non-classical region $\Gamma < 0$. The present investigation is limited to oblique shocks that exhibit non-ideal, yet classical, features. Therefore, we will focus on shock waves whose adiabat lies entirely in the region $\Gamma > 0$.

We assume the shock to be a vanishing-thickness layer separating two regions of thermodynamic-equilibrium states within a non-reacting substance [7, 8]. Across the shock, matter flows and the fluid goes from state *A* to state *B* instantaneously. In a shock-attached reference frame (Fig. 3.1), the laws of conservation of mass, momentum and energy across the shock front, namely the well-known Rankine-Hugoniot relations for three-dimensional flows, locally assume the form

$$[\rho u_n] = 0, \tag{3.3a}$$

$$[P\mathbf{n} + \rho u_n \mathbf{u}] = 0, \tag{3.3b}$$

$$[h + \|\mathbf{u}\|^2/2] = 0, \tag{3.3c}$$

where $[\cdot] = ()_\mathrm{B} - ()_\mathrm{A}$ denotes the jump from the pre-shock state A to the post-shock state B. h is the fluid enthalpy, $\mathbf{n}$ is the unit vector normal to the shock front and $\mathbf{u}$ is the fluid velocity, being $\mathbf{u}_n = \mathbf{u} \cdot \mathbf{n}$ its normal component (we assume that the shock-attached coordinate system is such that $u_n > 0$). By projecting (3.3b) onto the normal direction and tangent plane, one obtains

$$[P + \rho u_n^2] = 0, \tag{3.4a}$$

$$[\mathbf{u}_t] = \mathbf{0}, \tag{3.4b}$$

where $\mathbf{u}_t = \mathbf{u} - \mathbf{u}_n$ denotes the tangential velocity. The above relations imply that the problem reduces to the study of normal shocks to which an orthogonal velocity field is superposed. After straightforward manipulations, the energy and the momentum balance equations in the direction normal to the shock are recast in the well-known form

$$[h] - \tfrac{1}{2}[P](v_\mathrm{A} + v_\mathrm{B}) = 0, \tag{3.5a}$$

$$[P] + m^2[v] = 0, \tag{3.5b}$$

where v is the specific volume and m,

$$m = \rho_\mathrm{A} u_{n\mathrm{A}} = \rho_\mathrm{B} u_{n\mathrm{B}}\,, \tag{3.6}$$

expresses the mass flow conservation across the discontinuity. Equation (3.5a), known as the Hugoniot relation, determines the so-called Hugoniot locus i.e., the locus of states that can possibly be connected to the initial state by means of a shock wave. In the P–v plane, the Hugoniot locus is commonly referred to as the shock adiabat, while the straight line defined by relation (3.5b) as the Rayleigh line. The Rankine-Hugoniot relations are not sufficient to isolate physical shock solutions. These are selected by enforcing extra conditions accounting for physical effects that are not modeled in the simplified governing equations, namely in the limit of vanishing viscosity and heat conduction. Because the second law of thermodynamics requires that entropy does not decrease, (3.3) must be extended to include

$$[s] \geq 0 \tag{3.7}$$

Further admissibility conditions stem from mechanical stability requirements. In order for the shock front to be stable against one-dimensional perturbations of the normal flow, the well-known *speed-ordering condition*

$$M_{nB} \leq 1 \leq M_{nA}\,, \tag{3.8}$$

must be satisfied along the shock front, where $M_n = u_n/c$ denotes the normal Mach number [5].

3.3 Non-ideal Effects in Oblique Shock-waves

A set of exemplary cases for the polytropic vdW model of siloxane fluid MDM is examined and used to investigate the dependence of the properties of oblique shock waves on the upstream state (P_A, v_A, M_A). Four different upstream states are considered, as described in Tab. 3.1 and shown in Fig. 3.2.

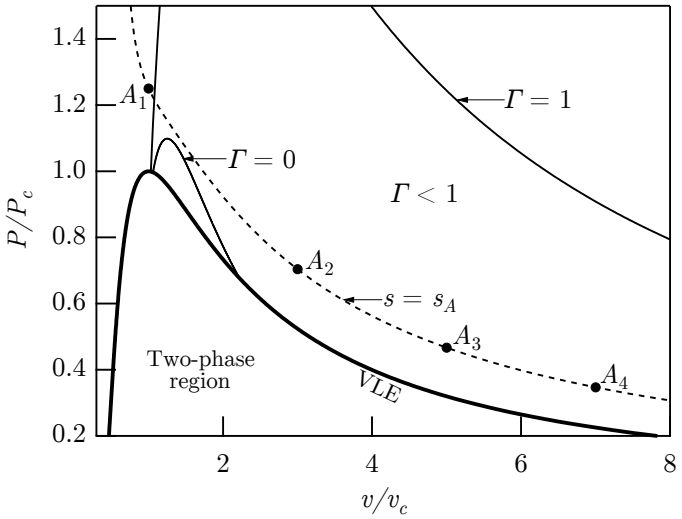

Figure 3.2: Pressure versus specific volume diagram computed from the polytropic van der Waals model of siloxane fluid MDM, illustrating the thermodynamic regions $\Gamma < 1$ and $\Gamma < 0$. Also shown are the four pre-shock states of the exemplary oblique shock configurations, chosen along the isentrope $s = s_A$;

Case	P_A/P_c	ρ_A/ρ_c	T_A/T_c	Γ_A
A_1	1.250	1.000	1.063	1.674
A_2	0.704	0.333	1.037	0.667
A_3	0.467	0.200	1.027	0.829
A_4	0.347	0.143	1.021	0.887

Table 3.1: Pre-shock states of the exemplary oblique shock configurations for the polytropic van der Waals model of siloxane fluid MDM. All the cases considered have the same pre-shock Mach number $M_A = 2$ and pre-shock entropy $s_A = s(1.250P_c, v_c)$, where subscript c denote the properties at critical point;

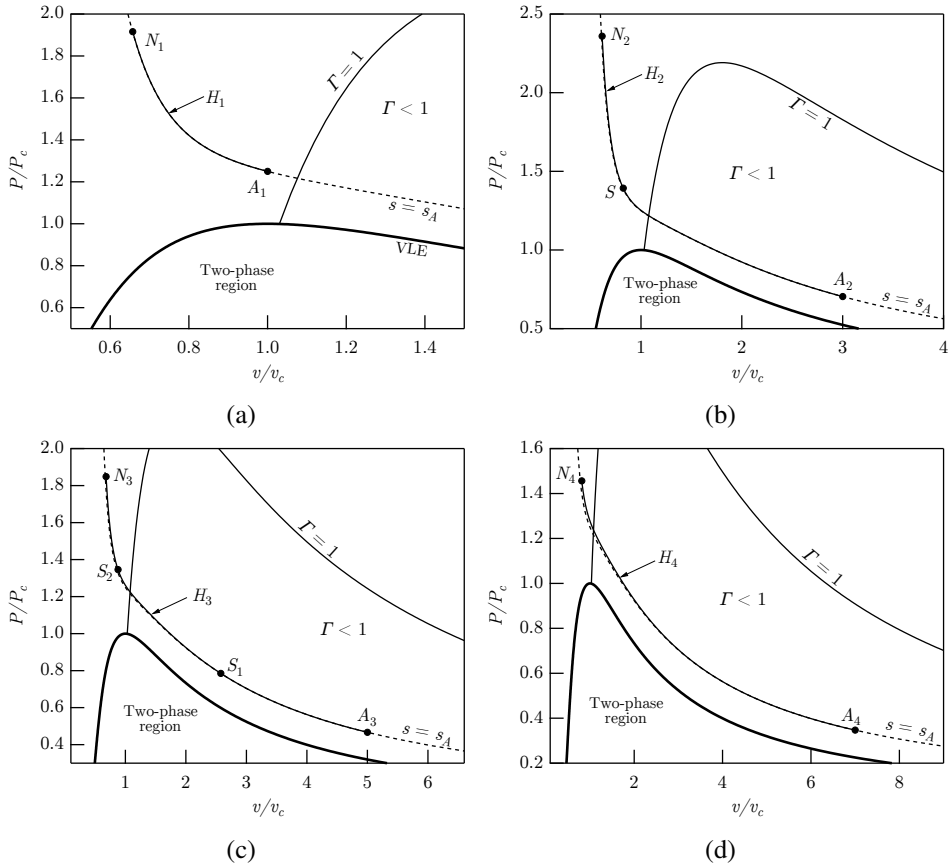

Figure 3.3: Pressure versus specific volume diagrams illustrating shock adiabats (curves labelled H) originating from pre-shock states as computed from the polytropic vdW model of siloxane fluid MDM. The endpoints labelled as N correspond to the normal shock configuration. Also shown are the post-shock states S at which $M_B = M_A$. (a) case A_1; (b) case A_2; (c) case A_3; (d) case A_4;

In order to simplify the following treatment, the selected configurations exhibit the same upstream values of the Mach number and of the entropy, namely $M_A = 2$ and $s_A = s(1.25P_c, v_c)$. First, we consider oblique shocks originating from pre-shock state A_1, which is located in the region $\Gamma > 1$ at density values higher than those corresponding to $\Gamma < 1$. Hence, $\Gamma_{A_1} > 1$ and, with reference to Fig. 3.3(a), the compressive branch of shock adiabat H_1 centered on state A_1 is entirely located in the region $\Gamma > 1$. The endpoint denoted as N_1 corresponds the post-shock state of the normal shock from state A_1. Fig. 3.4(a) shows the variation of the ratios c_A/c_B, M_B/M_A and $M_{B,n}/M_{A,n}$ with the shock angle β. The range of shock angles spans from the minimum value $\beta_{\min} = \mathrm{asin}(1/M_A)$, corresponding to an acoustic wave, up to $\beta = \pi/2$, corresponding to a normal shock wave. Owing to relation (3.3b), the tangential component of the velocity (with respect to the oblique shock) is conserved across the shock and, therefore, $c_A/c_B = M_{B,t}/M_{A,t}$.

As shown in Fig. 3.4(a), c_B increases and, therefore, $M_{B,t}/M_{A,t}$ decreases with increasing β or, equivalently, decreasing v. Because $M_{B,n} < M_{A,n}$, as required by the speed ordering relation Eq. 3.8, $M_B < M_A$ for each possible oblique shock configuration with upstream state A_1. These observations could be anticipated and reasonably justified by neglecting the entropy rise across the shock wave, so that the shock adiabat coincide with the isentrope passing through the pre-shock state. In this limit, the speed of sound would necessarily increase with increasing density because $\Gamma > 1$. However, this holds even if we take into account the entropy rise whenever condition $(\partial c/\partial s)_v > 0$ is satisfied, as it is the case within the polytropic vdW model. Moreover, as discussed by Menikoff and Plohr [9], $(\partial c/\partial s)_v > 0$ is expected to hold to occur for most real materials in their pure phases.

Next, state A_2, with $\Gamma_{A_2} < 1$, is considered. With reference to Fig. 3.3(b), a wide portion of the shock adiabat H_2 lies inside the region $\Gamma < 1$. As expected due to the almost negligible entropy rise together with $\Gamma_B < 1$, c_B initially decreases with increasing shock angle, as shown in Fig. 3.4(b), where $c_B < c_A$ up to 47.9° and a pronounced local minimum if found at 38.3°. As a result, there exists a range of shock angles in which the increase in tangential component of the Mach number is sufficient to compensate the necessary decrease in the normal Mach number. The post-shock state characterized by $M_B = M_A$ occurs at 42.5° and it is denoted as point S in Fig. 3.3(b). In the range between $\beta \in [\beta_{\min}, \beta = 42.5°]$ the Mach number increases across the shock. The local peak for M_B is found at 38.2° and corresponds to the ratio $M_B/M_A = 1.5$.

If the pre-shock density is further lowered, a larger portion of the shock adiabat in embedded in the region $\Gamma < 1$, as shown in Fig. 3.3(c) corresponding to A_3. As a result, the range of shock angles where $c_B < c_A$ also increases, see Fig. 3.4(c). For the present configuration, $c_B < c_A$ up to 72.1° with a local maximum at 51.0°. However, the evolution of the Mach number is somewhat more complex if compared to the previous case. The Mach number initially decreases with increasing shock angle, as the increase of $M_{B,t}$ is overcompensated by the decrease of $M_{B,n}$. At $\beta = 35.2°$,

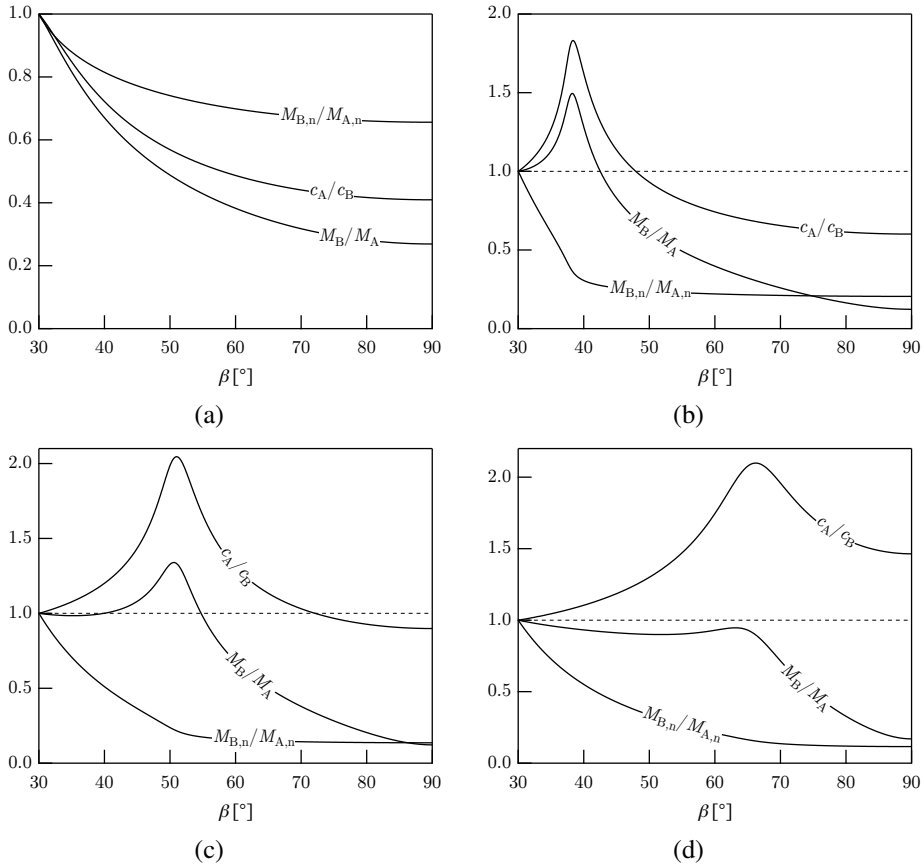

Figure 3.4: Variation of the speed of sound ratio c_A/c_B, normal Mach number ratio $M_{B,n}/M_{A,n}$ and Mach number ratio M_B/M_A with shock angle β as computed from the polytropic vdW model siloxane fluid MDM. The shock angle spans from the minimum value $\beta = \text{asin}(1/M_A)$, corresponding to an acoustic wave, up to the maximum value $\beta = \pi/2$, corresponding to a normal shock wave. (a) case A_1; (b) case A_2; (c) case A_3; (d) case A_4;

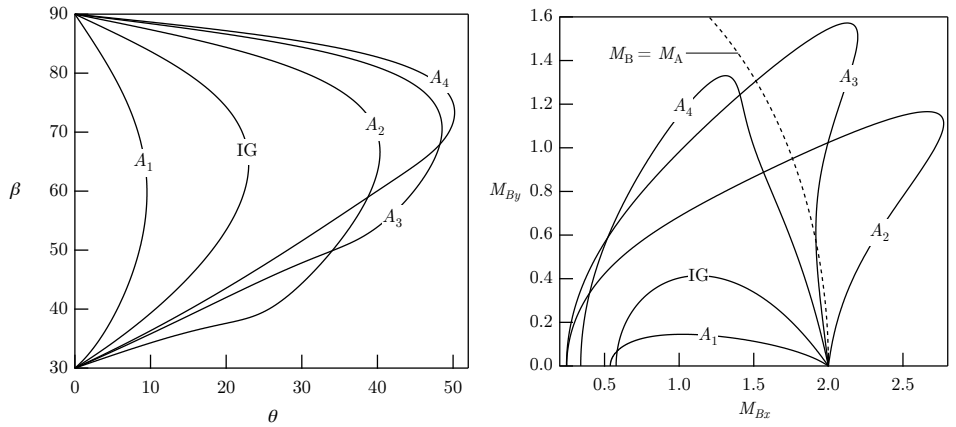

Figure 3.5: Diagrams illustrating (a) the variation of the flow deflection angle θ with shock angle β and (b) the polar of the Mach number, where $M_{Bx} = M_B \cos\theta$ and $M_{By} = M_B \sin\theta$, as computed from the polytropic van der Waals model of siloxane fluid MDM. Also shown are the curves, labeled *IG*, that correspond to the polytropic ideal gas case with the same upstream Mach number M_A used in the computation of the non-ideal cases.

the post-shock Mach number shows a local minimum and subsequently increases up to the pronounced peak ($\beta = 50.6°$) associated with the local minimum in the post-shock speed of sound. The two post-shock states that satisfy $M_B = M_A$ are shown in Fig.3.3(c), where they are denoted as points S_1 and S_2. State S_1 corresponds to a shock angle $\beta = 39.8°$ and it is located inside the region $\Gamma < 1$; post-shock state S_2 occurs at $\beta = 54.7°$ and, similarly to state S of case A_2, it is located in the thermodynamic region $\Gamma > 1$.

In the last exemplary case, we consider pre-shock state A_4. With reference to Fig. 3.3(d), the shock adiabat H_4 is almost entirely embedded in the region $\Gamma < 1$ and, as a result, $c_B < c_A$ over the complete range of shock angles, as shown in Fig. 3.4(d). However, the local minimum in the post-shock speed of sound now occurs at such large values of β that the necessary decrease in the normal component of the Mach number across the shock wave is sufficient to compensate the non-ideal increase in the tangential component of the Mach number. Therefore, $M_B < M_A$ for each possible oblique shock configuration originating from state A_4.

The variation of the flow deflection angle θ with the shock angle β for each of the configurations considered is shown in Fig. 3.5(a), where it is compared with the curve labelled *IG*, which corresponds to the polytropic ideal gas case and, as is well-known, it is independent of the pre-shock thermodynamic state P_A, v_A [2]. The curves computed by means of the polytropic vdW model exhibit substantial differences depending on the pre-shock thermodynamic state. In particular, the maximum turning angle $\theta_{\max}$ that the flow can sustain across a planar attached shock waves varies from

9.5° of case A_1 up to 50.2° of case A_4. In contrast, $\theta_{\max} = 23.0°$ for the polytropic ideal gas.

Finally, the same results can be conveniently presented also in term of the shock polar for the Mach number, namely a plot of $M_{By} = M_B \sin\theta$ versus $M_{Bx} = M_B \cos\theta$, as shown in Fig. 3.5(b) for each non-ideal configuration considered and the polytropic ideal gas counterpart.

If the pre-shock state A and the deviation angle ϑ are fixed, then, taking into account the equation of state $h = h(P, v)$, the Rankine-Hugoniot relation can be solved for the unknowns $(P_B, v_B, b_m u_B, \beta)$, provided that the deviation angle does not exceed a maximum value $\vartheta_{\max}$, which depends on the pre-shock state. For $\vartheta < \vartheta_{\max}$, the Rankine-Hugoniot equation yields two different solutions, namely the strong oblique shock (larger shock angle and pressure jump, downstream flow is always subsonic) and the weak oblique shock (lower shock angle and pressure jump, downstream flow always supersonic with the exception of a small interval in the close proximity of $\vartheta_{\max}$). Note, in particular, that $\vartheta = 0$ yields the trivial shock, namely, $\beta = \sin^{-1}(1/M_A)$, the acoustic angle, where $M = \|b_m u\|/c$ is the flow Mach number, and the normal shock solution. The acoustic limit makes it possible to explicitly ascertain the influence of the upstream state on the downstream Mach number. The Taylor series expansion of the function expressing the downstream Mach number, in the acoustic limit, assumes the form

$$M_B = M_A + \frac{J_A M_A^3}{\sqrt{M_A^2 - 1}}\vartheta + \mathcal{O}(\vartheta^2), \qquad \vartheta \to 0 \text{ and } [P] \to 0, \tag{3.9}$$

having defined $J = 1 - \Gamma - 1/M^2$ [10] and showing the dependence on the upstream thermodynamic state through Γ only.

3.4 Numerical prediction of non-ideal shock waves in other compounds

Despite the fact that the study presented up to here is limited to siloxane MDM only, most moderate-to-high molecular complex fluids exhibit the same qualitative behavior, in accordance with the principle of corresponding states. Therefore, the present analysis arguably applies to several different fluids employed in ORC power systems. This is confirmed by the calculations shown in Fig. 3.6. In Fig. 3.6, the variation of the fundamental derivative along the isentrope tangent to the saturated vapor boundary (local entropy maximum which occurs in retrograde fluids) is plotted for different ORC working fluids, showing the same qualitative trends. Moreover, Fig. 3.6 reports the minimum values of the total pressure and temperature leading to $J \geq 0$, and thus to the possibility of observing Mach number–increasing (weak) oblique shocks, along the same isentrope. These values would correspond to supercritical ORCs and are

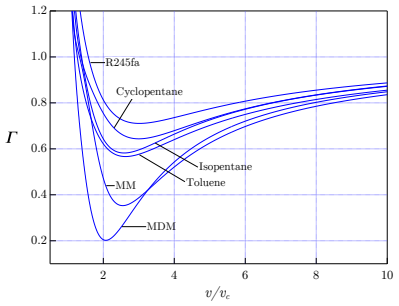

Fluid	$P^t_{\min}/P_c$	$T^t_{\min}/T_c$
MDM	1.174	1.015
MM	1.335	1.031
Toluene	1.808	1.061
Isopentane	1.918	1.073
Cyclopentane	2.129	1.082
R245fa	2.952	1.117

Figure 3.6: Results for different fluids currently employed in ORC power systems. Left: variation of the fundamental derivative with the specific volume, along the isentrope tangent to the saturation curve; right: minimum total pressure and temperature values for $J \geq 0$ along the isentrope tangent to the saturation curve. Reference thermodynamic models from the REFPROP library [11];

within the thermal stability limit for isopentane and R245fa, closer to the limit for MM, toluene and cyclopentane, while they appear to be slightly above the limit for MDM.

3.5 Conclusions

In this chapter, we provided a discussion of the thermodynamics of non-ideal flows with a special focus on non-ideal effects across oblique shock-waves.

Across a shock, the fluid undergoes a transformation from state A to state B and it was shown how this process is strictly related to the regime of the flow. If complex EoS are employed in place of the PIG, and if the pre-shock state is located in the non-ideal thermodynamic region $\Gamma < 1$, the speed of sound may decrease with pressure, along the shock adiabat. Under some particular conditions, the sound speed reduction is sufficiently large to result in the overall increase of the flow Mach number across the oblique shock wave.

The exemplary computations were performed using the polytropic van der Waals model of siloxane fluid MDM, for which the post-shock Mach number was found to increase up to 1.5 times the pre-shock Mach number. The present analysis has a sound theoretical basis, owing to the fact that the simple van der Waals model is known to predict the correct qualitative behavior in the single-phase thermodynamic region close to liquid-vapour equilibrium (sufficiently far from the critical point for critical phenomena to be negligible). Nevertheless, in the chapter the occurrence of non-ideal shock waves is confirmed for diverse substances using also state-of-the-art

thermodynamic models. The experimental verification of the occurrence of non-ideal shock waves can be devised in test rigs working with fluids of high or even moderate molecular complexity, though certain practical difficulties, mostly related to thermal stability of the working fluid, may be raised.

The non-ideal increase of the flow Mach number across oblique shocks and the dependence of the shock angle and flow deviation from the upstream thermodynamic state are arguably relevant in applications where oblique shock waves are either intentionally formed (e.g. engine intake ramps) or a byproduct of the supersonic flow expansion (e.g. fish-tail shocks in turbine nozzle vanes, over/under-expanded jet from nozzle exit). For instance, stator blades of supersonic high-pressure ORC turbines are designed to provide a large outlet Mach number, especially at the first stage. Due to the finite thickness of the trailing edge, a limited region of separation between the high speed flows from the pressure and suction sides is usually formed. The merging of these two supersonic flows gives rise to the so-called fish-tail shocks which are usually associated to a total pressure loss (in other words, performance degradation). The non-ideal effects described in the chapter influence the pattern of the fish-tail shocks and, therefore, their understanding is of the utmost relevance for the future improvement of ORC turbine design.

Complex patterns of oblique shock waves can also be found in applications other than ORCs including, just to mention a few, engine intakes rockets, supersonic nozzle outflows, under-expanded jets and highly-loaded turbo-machinery stages.

References

[1] G. Gori, D. Vimercati, and A. Guardone. "Non-ideal compressible-fluid effects in oblique shock waves". In: *Journal of Physics: Conference Series* 821.1 (2017), p. 012003. URL: http://stacks.iop.org/1742-6596/821/i=1/a=012003.

[2] P. A. Thompson. *Compressilbe Fluid Dynamics*. McGraw-Hill, 1988.

[3] D. Vimercati, G. Gori, and A. Guardone. "Non-ideal oblique shock waves". In: *Journal of Fluid Mechanics* 847 (2018), pp. 266–285. DOI: 10.1017/jfm.2018.328.

[4] M. S. Cramer and L. M. Best. "Steady, isentropic flows of dense gases". In: *Phys. Fluids A* 3.4 (1991), pp. 219–226.

[5] P. D. Lax. "Hyperbolic systems of conservation laws II". In: *Comm. Pure Appl. Math.* 10.4 (1957), pp. 537–566.

[6] O. Oleinik. "Uniqueness and stability of the generalized solution of the Cauchy problem for a quasi-linear equation". In: *Usp. Mat. Nauk* 14.2 (1959), pp. 165–170.

[7] Y. B. Zel'dovich. "On the Possibility of Rarefaction Shock Waves". In: *Zh. Eksp. Teor. Fiz.* 4 (1946), pp. 363–364.

[8] L. D. Landau and E. M. Lifshitz. *Fluid mechanics, 2nd edn*. Pergamon Press, 1987. Chap. 9.

[9] R. Menikoff and B. J. Plohr. "The Riemann problem for fluid flow of real material". In: *Rev. Mod. Phys.* 61(1) (1989), pp. 75–130.

[10] M. S. Cramer and A. B. Crickenberger. "Prandtl-Meyer function for dense gases". In: *AIAA Journal* 30.2 (1992), pp. 561–564.

[11] E. W. Lemmon, M. L. Huber, and M. O. McLinden. "NIST reference database 23: reference fluid thermodynamic and transport properties–REFPROP, version 9.1". In: *Standard Reference Data Program* (2013).

[12] D. Y. Peng and D. B. Robinson. "A New Two-constant Equation of State". In: *Ind. Eng. Chem. Fundam.* 15 (1976), pp. 59–64.

[13] J. J. Martin and Y. C. Hou. "Development of an Equation of State for Gases". In: *AIChE J.* 1.2 (June 1955), pp. 142–151.

[14] J. J. Martin, R. M. Kapoor, and N. De Nevers. "An Improved Equation of State for Gases". In: *AIChE J.* 5.2 (1959), pp. 159–160.

[15] R. Span and W. Wagner. "Equations of state for technical applications. I. Simultaneously optimized functional forms for nonpolar and polar fluids". In: *Int. J. Thermophys.* 24.1 (2003), pp. 1–39.

[16] R. Span and W. Wagner. "Equations of state for technical applications. II. Results for nonpolar fluids". In: *Int. J. Thermophys.* 24.1 (2003), pp. 41–109.

CHAPTER 4

THE NICFD CFD SOLVER

Part of the contents of this chapter appear in

S. Vitale, G. Gori, M. Pini, A. Guardone, T. D. Economon, F. Palacios, J. J. Alonso, P. Colonna, *Non-Ideal compressible-fluid effects in oblique shock waves*, 22nd AIAA Computational Fluid Dynamics Conference, 2015

M. Pini, S. Vitale, P. Colonna, G. Gori, A. Guardone, T. D. Economon, J. J. Alonso, F. Palacios, *SU2: the open-source software for non-ideal compressible flows*, Journal of Physics: Conference Series, Vol. 821, 2017

4.1 Introduction

In this chapter, the steps required to extend an ordinary CFD solver to non-ideal flows are briefly reported. Technical details about the modifications required to accommodate the more complex EoS, required to model non-ideal effects, are provided. The generalized flow equations are reported and differences with respect to ideal-gas counterpart are highlighted.

Non-ideal fluid mechanics concerns the dynamics of fluids that do not generally abide by the ideal gas law $Pv = RT$, with P pressure, v specific volume, R gas constant and T temperature. In most circumstances and applications, the ideal gas assumption yields an optimization of the software performances. For instance, the code implementation is greatly simplified by the fact that the speed of sound, the specific internal energy and the enthalpy are functions of the fluid temperature only. To deal with non-ideal flows, the structure of a typical CFD solver must be largely re-designed.

Currently, there exists only a limited number of CFD solvers suitable for the investigation of non-ideal flows. ANSYS® Fluent® is a well established and widely used CFD solver. Fluent is a professional software and it is endowed with a broad set of physical modeling tools needed to simulate flows, turbulence, heat transfer, and reactions for industrial applications. Fluent capabilities span from aerospace applications to combustion problems, including multiphase flows from bubble columns to oil platforms and many others. Nevertheless, the latest algorithms for non-ideal flows are still not available in Fluent. Moreover, its closed-source nature prevents researchers from customizing the code and adding new capabilities.

OpenFOAM® is a free open-source CFD with a large user base across most areas of engineering and science, from both commercial and academic organizations. Software capabilities range from chemical reacting flows to acoustics, to solid mechanics and to many other physical problems. In particular, in OpenFOAM it is possible to perform non-ideal gas simulations. Namely, it is equipped with the Peng-Robinson fluid model or, alternatively, with Look Up Tables (LUT) which replace the runtime

complex thermodynamic computations, related to use of state-of-the-art EoS, with simpler array indexing operations

Other CFD software, for instance zFlow, Joe and Flowmesh, are also capable of dealing with non-ideal flows. Namely, zFlow [1] is an advanced CFD code which can model inviscid flows of dense gases and has access to a wealth of thermodynamic library. Joe [2] is a compressible Navier-Stokes solver coupled to the FluidProp library [3]. Flowmesh [4] is instead an open-source finite-volume solver for the Euler equations of motions. The solver works with hybrid dynamic meshes that allow the simulation of the flow around complex geometries in a relative motion.

Moreover, though they do not represents a framework for the simulation of dense gas flows, literature is plentiful of contributions that treat the development of numerical schemes tailored on NICFD flows. Among the others, notable contributions are [5–10].

SU2 is an open-source platform designed to solve multi-physics Partial Differential Equation (PDE) and PDE-constrained optimization problems [11, 12]. Recently, the SU2 users community reached a considerable dimension which makes the code now attractive from research purposes. Indeed, a broad number of developers all over the world are currently active and take care of maintaining the code and extending its capabilities. Remarkably, the SU2 suite includes a numerical solver suitable for the investigation of fully turbulent non-ideal flows [13–15]. In the following, the reliability the SU2 non-ideal solver is verified against very simple flow configurations. For these test cases, it is possible to compute the analytic solutions and therefore to provide an indication about the solver capabilities. Test cases presented here include steady and unsteady flows in the ideal, non-ideal and non-classical regime.

In this chapter, Sec. 4.2 shows the steps required to extend a CFD solver to non-ideal flows. Eventually, Sec. 4.3 reports the verification of the non-ideal solver for a set of reference test cases of fluid flows in the dense gas regime.

4.2 The SU2 NICFD CFD solver

In the following, the main features characterizing a non-ideal solver are briefly presented. We start by recalling the three-dimensional Navier-Stokes equations for compressible flows which read:

$$\frac{\partial \mathbf{u}}{\partial t} + \nabla \cdot \mathbf{f}(\mathbf{u}) = \nabla \cdot \mathbf{d}(\mathbf{u}), \tag{4.1}$$

where $\mathbf{u} = (\rho, \mathbf{m}, E^t)^T$ is the vector of the conserved variables.

The vector $\mathbf{u}$ includes the mass density $\rho \in \mathbb{R}^+$, the momentum density $\mathbf{m} \in \mathbb{R}^3$, and the total energy density per unit volume $E^t \in \mathbb{R}$, $E^t = \rho\left(e + \frac{1}{2}||\mathbf{v}||^2\right)$, being e the internal energy per unit mass and $\mathbf{v} = \mathbf{m}/\rho \in \mathbb{R}^3$ the velocity vector. The function $\mathbf{f}(\mathbf{u}) \in \mathbb{R}^5 \times \mathbb{R}^3$ is the hypervector of the advection and pressure fluxes, namely,

$\mathbf{f}(\mathbf{u}) = (\mathbf{m}, (\mathbf{m} \otimes \mathbf{m})/\rho + \Pi, \mathbf{m}(E^t + P)/\rho)^T$, where $\Pi = \Pi(\mathbf{u})$ is the pressure as a function of the conserved variables $\mathbf{u}$, $\mathbf{I} \in \mathbb{R}^3$ the identity matrix and $\otimes$ operator is the direct product. The viscous and thermal flux function $\mathbf{d}(\mathbf{u}) \in \mathbb{R}^5 \times \mathbb{R}^3$ reads $\mathbf{d}(\mathbf{u}) = (\mathbf{0}, \varepsilon, \mathbf{v}^T \cdot \varepsilon - \mathbf{q})^T$.

The Navier-Stokes equations (4.1) must be completed by constitutive models suitable for the computation of the fluid thermodynamic state and of the molecular properties μ, λ and κ. For Newtonian fluids of interest here, the viscous stress tensor, $\varepsilon = \varepsilon(\mathbf{v}) \in \mathbb{R}^3$, reads $\varepsilon(\mathbf{v}) = \mu \left[\nabla \mathbf{v} + (\nabla \mathbf{v})^T\right] + \lambda(\mathbf{v})\mathbf{I}$, where $\mu = \mu(\mathbf{u})$ and $\lambda = \lambda(\mathbf{u})$ are respectively the dynamic and bulk viscosity coefficients, and $\mathbf{q} = \mathbf{q}(\mathbf{u})$ is the thermal flux. Under the Fourier hypothesis, the thermal flux simplifies to $\mathbf{q}(\mathbf{u}) = -\kappa \nabla T(\mathbf{u})$, where $\kappa = \kappa(\mathbf{u})$ is the thermal conductivity coefficient and $T = T(\mathbf{u})$ is the temperature.

As reported in the previous chapter, the local state of a thermodynamic system in a stable equilibrium is completely defined by two independent variables only. In completing the Navier-Stokes system (4.1) with thermodynamics, one note that the two independent variables (density and internal energy) can be immediately computed from the conservative variable vector and from the definition of total energy.

$$\rho = u^{(1)}, \quad e = \frac{u^{(5)}}{u^{(1)}} - \frac{(u^{(2)} + u^{(3)} + u^{(4)})^2}{2u^{(1)}u^{(1)}} = E - \frac{\|\mathbf{v}\|^2}{2}, \tag{4.2}$$

where $u^{(i)}$ is the i-th element of the vector $\mathbf{u}$. Unless very simple EoS are considered, the computation of the thermodynamic state usually requires the solution of a nonlinear equation (or of a set of equations), as most models consider the temperature and the density (or specific volume) as independent variables. As a consequence, the thermodynamic completion of the Navier-Stokes equations with accurate thermodynamics models is a complex and expensive task which usually yields a sharp increase of the computational time and to numerical stability issues. For example, the non-ideal dependence of the internal energy and enthalpy on both the temperature and the density—for an ideal gas both e and h depends on T only—forbids one to use simplified expressions for the flux function $\mathbf{f}$ and its Jacobian $\mathbf{A} = \partial \mathbf{f}/\partial \mathbf{u}$. Furthermore, the flux function $\mathbf{f}$ is no longer a homogeneous function of degree one with respect to $\mathbf{u}$. Additionally, also the transport coefficients do no longer depend on temperature only. To produce an upwind discrete counterpart of the flux function $\mathbf{f}$ in the NICFD regime, the implementation of a generalised approximate Riemann solver (ARS) of Roe type [16–18] is required. Note that the following discussion could be extended to other numerical schemes but it is here limited to the Roe type solvers only. For the sake of completeness, in SU2 there are several algorithms capable of accommodating complex EoS. Namely, the Harten-Lax-van Leer Contact (HLLC) and the Advection Upstream Splitting Method (AUSM$^+$) type solvers. The implementation of the three schemes is based on the work from [7, 19].

The generalised Roe matrix $\tilde{\mathbf{A}}_{ij}^n$ fulfilling the Roe linearisation problem

$$[\mathbf{f}(\mathbf{u}_j) - \mathbf{f}(\mathbf{u}_i)] \cdot \mathbf{n} = \tilde{\mathbf{A}}_{ij}^n [\mathbf{u}_j - \mathbf{u}_i], \tag{4.3}$$

between state i and state j along a given direction vector n, is the scalar product of the jacobian matrix of the fluxes times the vector $\mathbf{n}$. The jacobian $\tilde{\mathbf{A}}_{ij}^n$ is evaluated at the intermediate generalised state comprising the Roe-averaged values ($\tilde{\cdot}$) of the velocity $\tilde{\mathbf{v}}_{ij}$ and total enthalpy per unit mass $\tilde{h}_{ij}^t$, namely

$$\tilde{\mathbf{v}}_{ij} = \frac{\sqrt{\rho_i}v_i + \sqrt{\rho_j}v_j}{\sqrt{\rho_i}+\sqrt{\rho_j}} \qquad \text{and} \qquad \tilde{h}_{ij}^t = \frac{\sqrt{\rho_i}h_i^t + \sqrt{\rho_j}h_j^t}{\sqrt{\rho_i}+\sqrt{\rho_j}}$$

When non-ideal gas models are considered, an additional consistency condition must be fulfilled [18], namely

$$\tilde{\chi}_{ij}(\rho_i - \rho_j) + \tilde{\kappa}_{ij}(\rho_i e_i - \rho_j e_j) = (P_i - P_j)\,, \tag{4.4}$$

where the pressure derivatives $\tilde{\chi}_{ij}$ and $\tilde{\kappa}_{ij}$ are defined as

$$\chi = \left(\frac{\partial P}{\partial \rho}\right)_{\rho e} = \left(\frac{\partial P}{\partial \rho}\right)_e - \frac{e}{\rho}\left(\frac{\partial P}{\partial e}\right)_\rho \quad \text{and} \quad \kappa = \left(\frac{\partial P}{\partial \rho e}\right)_\rho = \frac{1}{\rho}\left(\frac{\partial P}{\partial e}\right)_\rho\,, \tag{4.5}$$

When the PIG law applies, χ is equal to zero and κ is a constant equal to $\gamma - 1$. Therefore, the consistency condition (4.4) is identically satisfied for all the possible intermediate states. When non-ideal gas models are used, Eq. (4.4) provides only one relation for the two unknowns χ and κ and a proper closure condition must be given. In SU2, the closure proposed in [17] is implemented.

The generalized jacobian matrix $\tilde{\mathbf{A}}_{ij}^n$ of the convective flux reads

$$\tilde{\mathbf{A}}_{ij}^n = \begin{bmatrix} 0 & n_1 & n_2 & n_3 & 0 \\ \zeta n_1 & (1-\kappa)\tilde{\mathrm{v}}_1 n_1 & \tilde{\mathrm{v}}_1 n_2 - \kappa n_1 \tilde{\mathrm{v}}_2 & \tilde{\mathrm{v}}_1 n_3 - \kappa n_1 \tilde{\mathrm{v}}_3 & \kappa n_1 \\ \zeta n_2 & \tilde{\mathrm{v}}_2 n_1 - \kappa n_2 \tilde{\mathrm{v}}_1 & (1-\kappa)\tilde{\mathrm{v}}_2 n_2 & \tilde{\mathrm{v}}_2 n_3 - \kappa n_2 \tilde{\mathrm{v}}_3 & \kappa n_2 \\ \zeta n_3 & \tilde{\mathrm{v}}_3 n_1 - \kappa n_3 \tilde{\mathrm{v}}_1 & \tilde{\mathrm{v}}_3 n_2 - \kappa n_3 \tilde{\mathrm{v}}_2 & (1-\kappa)\tilde{\mathrm{v}}_3 n_3 & \kappa n_3 \\ 0 & \tilde{h}^t n_1 & \tilde{h}^t n_2 & \tilde{h}^t n_3 & 0 \end{bmatrix} - \begin{bmatrix} 0 & 0 & 0 & 0 & 0 \\ \tilde{\mathrm{v}}_1 q_n & -q_n & 0 & 0 & 0 \\ \tilde{\mathrm{v}}_2 q_n & 0 & -q_n & 0 & 0 \\ \tilde{\mathrm{v}}_3 q_n & 0 & 0 & -q_n & 0 \\ (\tilde{h}^t - \zeta) q_n & \kappa \tilde{\mathrm{v}}_1 q_n & \kappa \tilde{\mathrm{v}}_2 q_n & \kappa \tilde{\mathrm{v}}_3 q_n & -(1+\kappa) q_n \end{bmatrix},$$

where

$$\zeta = \left(\chi + \frac{1}{2}\kappa |\tilde{\mathbf{v}}|^2\right), \quad q_n = \tilde{\mathbf{v}} \cdot \mathbf{n}, \tag{4.6}$$

The discrete form of (4.1) is obtained by enforcing the integral over a number of node-centered finite volumes, which are constructed from the underlying unstructured triangulation of the domain. The SU2 numerical solver is based on baricentrical finite volumes [20] which are easily built from hybrid meshes made of elements

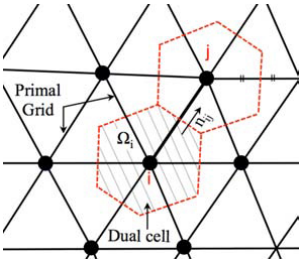

Figure 4.1: schematic of the primal mesh and the control volume on a dual mesh;

of different types in both two and three spatial dimensions. The standard edge-based structure on a dual grid with control volumes constructed using a median-dual vertex-based scheme is shown in Fig. 4.1. Eq. 4.7 shows the semi-discretized integral form of the PDE:

$$\frac{d\hat{\mathbf{u}}_i}{dt} + \sum_{j \in \mathcal{N}(i)} (\hat{\mathbf{f}}_{ij} + \hat{\mathbf{d}}_{ij}) \Delta S_{ij} - Q|\Omega_i| = \frac{d\hat{\mathbf{u}}_i}{dt} + R(\hat{\mathbf{u}}_i) = 0\,, \tag{4.7}$$

where the hat points out that the variable is expressed in the discrete form and $\hat{\mathbf{u}}_i$ is the solution averaged in the volume belonging to the $i-th$ cell $\hat{\mathbf{u}}_i = \int_{\Omega_i} \mathbf{u}\, d\Omega$. $R_i(\hat{\mathbf{u}})$ is the residual and $\tilde{\mathbf{f}}_{ij}$ and $\tilde{\mathbf{f}}_{ij}$ are the projected numerical approximations of the convective and viscous fluxes, respectively. ΔS_{ij} is the area of the face associated with the edge ij, Ω_i is the volume of the control volume and $\mathcal{N}(i)$ are the neighboring nodes to node i. The convective and viscous fluxes are evaluated at the midpoint of an edge: the numerical solver loops through all of the edges in the primal mesh and then integrates the numerical fluxes, to evaluate the residual at every node in the grid.

A detailed description of the modifications applied to extend SU2 to NICFD flows is provided in [13]. Within the SU2 framework, an embedded thermodynamic library provides access to several different EoS. Namely, it includes the PIG, the polytropic vdW [21] and the polytropic PR [22] fluid models. Moreover, the multi-purpose thermodynamic library FluidProp [3], implementing the state-of-the-art fluid models, can be accessed through a dedicated interface. For instance, the FluidProp library includes a set of models for the accurate computation of molecular transport properties in both dilute-gas and non-ideal conditions, based on the generalized multiparameter correlations from [23] In turbulent flows, the transport coefficients μ, λ and κ, appearing in the Reynolds-Averaged Navier-Stokes (RANS) equations, include also the contribution of the so-called turbulence or eddy viscosity and the total thermal conductivity resulting from the Boussinesq hypothesis [24]. The turbulent contribution is evaluated using well-established turbulence models, as reported in [12]. In [12], all the details related to the numerical solution of the RANS equations, using a standard node-centred finite-volume scheme for dilute gases on unstructured grids, are also reported. In SU2, a limited construction of the flow variable, according to

Fluid	R_{gas} [J/KgK]	γ	P_{cr} [Pa]	T_{cr} [K]	ρ_{cr} [Kg/m^3]
Air	287.058	1.4	-	-	-
MDM	35.152	1.018	1415000	564.09	256.82

Table 4.1: fluid parameters considered for the unsteady propagation of a shock within a pipe. Subscript *cr* indicates values at the critical point;

the MUSCL approach [25], is available to obtain a second-order accuracy in smooth flow regions.

4.3 Software Verification

In the context of ideal flows of air, the reliability of the SU2 suite was already assessed extensively in earlier works, see for instance [11, 12, 26–28].

In this section, the capabilities of the SU2 NICFD solver are verified for simple flow configurations involving fluids in a non-ideal regime. For these particular test cases, the analytic solution is available. The test set include: the unsteady propagation of a shock within an open-end pipe, a steady supersonic flow over a double-wedge and a non-classical rarefaction shock wave. Eventually, the non-ideal expanding flow through a converging-diverging nozzle is considered, to assess the error related to the algorithms implementation and the dependence of the solution on the numerical grid.

4.3.1 Unsteady Shock Propagation

This test case concerns the propagation of a shock through a fluid in the non-ideal gas regime. Unsteady simulations were carried out using a first order dual-time stepping method and a time step equal to $1 \cdot 10^{-4}$ s. In space, first and second order accurate schemes of Roe type were employed. For second order accurate schemes, a flux limiting function (Venkatakrishnan slope limiter) was used. Spatial gradients were reconstructed using a weighted least square approach. In the following, the propagation of the shock is simulated both considering air and siloxane MDM. Tab. 4.1 reports the fluid parameters specified for the numerical simulations (the gas constant R, the critical values and the specific heat ratio γ). The domain consists of an open-end pipe of finite length, namely a rectangular domain of length $L = 10$ m and height $h = 0.5$ m. The problem is two-dimensional and viscous and thermal effects are neglected. The shock moves from left to right and it is generated by applying an initial pressure and temperature jump at the left boundary. The pipe presents an open end, on the right side. Therefore, the shock propagates rightwards and it is eventually discharged into an infinite-acting reservoir. A constant pressure condition is imposed at the right boundary, $p_{out} = 101325$ Pa for air and $p_{out} = 800000$ Pa for MDM. With reference to Fig. 4.2(a), initially the left-to-right movement of the shock creates two uniform

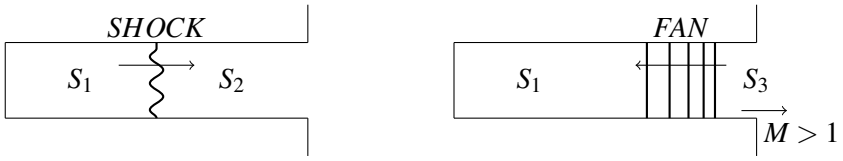

(a) (b)

Figure 4.2: unsteady shock propagation through an open-end pipe. Pictures identify the pertinent thermodynamic regions. (a) A shock wave separating zone 1 and 2 is initially moving rightwards; (b) A rarefaction fan separating zone 1 and 3 is traveling leftwards, after the shock is discharged into the infinite-acting reservoir;

regions: 1 (downstream state with respect to the shock) and 2 (upstream state with respect to the shock). Given the simplicity of the considered problem, it is possible to retrieve the analytic solution for both the PIG and the polytropic vdW fluid model. Indeed, the *Rankine-Hugoniot* condition impose a dependence of the post-shock state on the upstream fluid conditions, see [29].

The state downstream the shock (S_1) is fully known as it is arbitrarily assigned as an initial condition. The value of the static pressure P_2 is also arbitrarily applied, as a boundary condition. Therefore, it is possible to solve the Rankine-Hugoniot equation numerically, to retrieve the value of the density in the post-shock region. According to the state principle, once ρ_2 and p_2 are available the post-shock state (S_2) is uniquely defined. At this point, the speed of the shock can be reconstructed.

After the shock is discharged, the fluid may exit the pipe at either supersonic, transonic or subsonic speed. Only the subsonic discharge case is considered here: a rarefaction fan is produced and characteristic waves travel upstream, from right to left, to generate an isentropic expansion which matches the outer pressure. Consequently, a new region with state S_3 is found instead of zone 2, see Fig. 4.2(b). The analytic solution for this particular configuration is retrieved by exploiting the properties of the Riemann invariants. For MDM, the physics of the rarefaction is governed by more complex equations. The detailed procedure to retrieve the exact solution for a vdW flow is reported in [30].

Diverse meshes made up by quadrilateral elements were employed. Each mesh includes only one element in the direction parallel to the shock as along this direction the solution is constant. Namely, in the shock propagation direction the grid resolution is 10/50 [m] (grid *A*), 10/100 [m] (grid *B*), 10/250 [m] (grid *C*) and 10/500 [m] (grid *D*). Fig. 4.4(a) reports the grid sensitivity analysis. The analysis is carried out evaluating the solution of the flow field involving pure air at $t = 0.01$, more time instances were considered but the comparison is not reported here for the sake of brevity. Results show little differences among the solutions computed over the diverse grids. Given the relatively cheap computational cost, hereinafter the most refined grid (*D*) is selected and used to carry out further analyses. A comparison of the

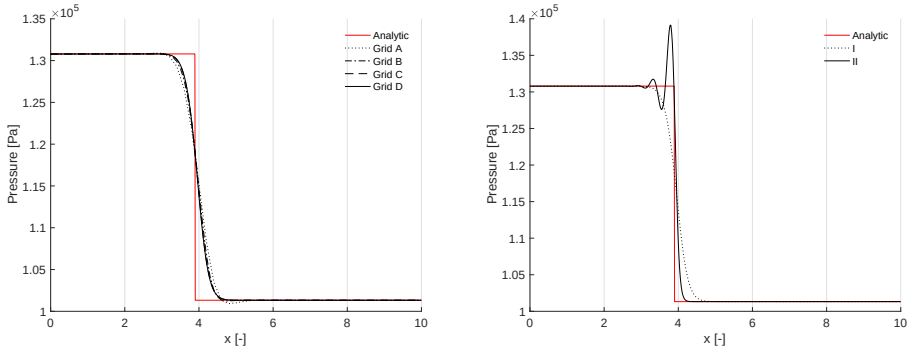

(a) air $t = 0.01$ s (b) air $t = 0.01$ s

Figure 4.3: shock propagation through air. The analytic solution is drawn as a continuous red line. (a) Comparison of the first order (time accurate) solution obtained using grids of different spatial resolution (*A*-*D*); (b) First order (time accurate) solution (dotted black curve) and second order (time accurate) solution (continuous black curve) comparison using the most refined grid;

	S_2	$\bar{S}_2$	$\Delta_{err}\%$	S_3	$\bar{S}_3$	$\Delta_{err}\%$
P [Pa]	130795	130795	< 0.01	101325	101324	< 0.01
T [K]	326.32	326.35	< 0.01	303.15	303.37	≈ 0.07
ρ [Kg/m^3]	1.3963	1.3961	$\approx$ -0.14	1.1641	1.1635	≈ 0.05

Table 4.2: air. The analytic thermodynamic states and the states computed using numerical simulations (barred values);

solution for the pressure distribution, as obtained using first and second order time accurate schemes, is reported in Fig. 4.4(b). The comparison is again obtained for air at $t = 0.01$, but more are available. As expected, the steep pressure gradient across the shock is smeared out using a first order accurate scheme. On the other hand, though the second order accurate scheme returns a very sharp pressure profile the typical oscillating behavior [31] is found in the close proximity of the shock. Hereinafter, we will make use of first order time accurate scheme only.

Tab. 4.2 and Tab. 4.3 reports the fluid states in regions 1-3, respectively for air and MDM, as predicted using the analytic procedure. In the same tables, the values computed through SU2 are also reported (barred values). Fig. 4.4(a-b) shows the analytic solution (the value of pressure along the pipe) at a specific time instance t for both an ideal (air, $t = 0.01$) and the non-ideal (MDM, $t = 0.05$) case. At the selected instances, the shock is still traveling rightwards. The exact solution (continuous line) is compared against the first and the second order accurate calculations (dashed and

	S_2	$\bar{S}_2$	$\Delta_{err}\%$	S_3	$\bar{S}_3$	$\Delta_{err}\%$
P [Pa]	838120	838120	< 0.01	800000	800000	< 0.01
T [K]	571.17	571.17	< 0.01	570.50	570.51	< 0.01
ρ [Kg/m^3]	52.53	52.53	< 0.01	49.52	49.52	< 0.01

Table 4.3: MDM. The analytic thermodynamic states and the states computed using numerical simulations (barred values);

dotted curves, respectively). Fig. 4.4(c-d) reports the same comparison for the rarefaction fan (traveling leftward) generated after the shock leaves the domain. Results are in good agreement: the shocks and the fans are correctly captured in terms of speed and intensity. Nevertheless, the solutions are smeared out due to numerical dissipation effects.

4.3.2 Double Wedge

The two-dimensional domain, depicted in Fig. 4.5(a), presents two abrupt slope variations that turn the stream by $\Delta\theta = 10^\circ$ each. Two different test cases are considered: a supersonic flow of MDM modeled with the PIG EoS and a supersonic flow of MDM modeled with the polytropic vdW EoS. Viscous effects and thermal conductivity are neglected. The numerical grid, a single-block mesh made up by quadrilateral cells, was created using the commercial software ANSYS ICEM. Different levels of spatial resolution were evaluated, starting from 10^4 up to 10^6 nodes. Fig. 4.6 reports the coarser grid. An implicit, second order accurate, Harten-Lax-van Leer Contact (HLLC) scheme [32] was exploited to carry out computations. For this test case, simulations were also done using a Roe type solver but results show no relevant difference, therefore they are not reported in the following.

In the following, inlet flow conditions correspond to M =2.4, static pressure P =1260000 Pa and temperature T 632.5 K, with a specific heat ratio $\gamma = 1.0125$. Five different and uniform regions, separated by shocks or contact/shear lines, are found. With reference to Fig. 4.5(b), the flow enters the domain at supersonic speed and, because of the consecutive changes in the wall slope (θ_1 and θ_2), two shock waves are generated. The two shocks propagate through the domain. After intersecting, the shocks form a single front which separates region 1 from region 5. Since the flow is zone 5 passes through a single oblique shock, while the flow in zone 3 undergoes two separate, weaker, shocks, the total entropic jump is generally different. It follows that also the variation of total pressure and total temperature are different along the two separate paths. Therefore, static pressure values in zone 3 and 5 will not match. Because of this mismatch, a weak shock or an expansion fan (dotted line in Fig. 4.5(b)) is generated in the flow, giving rise to a new region (zone 4). In principle, a shockwave propagating in between region 3 and 4 would be reflected at the lower wall,

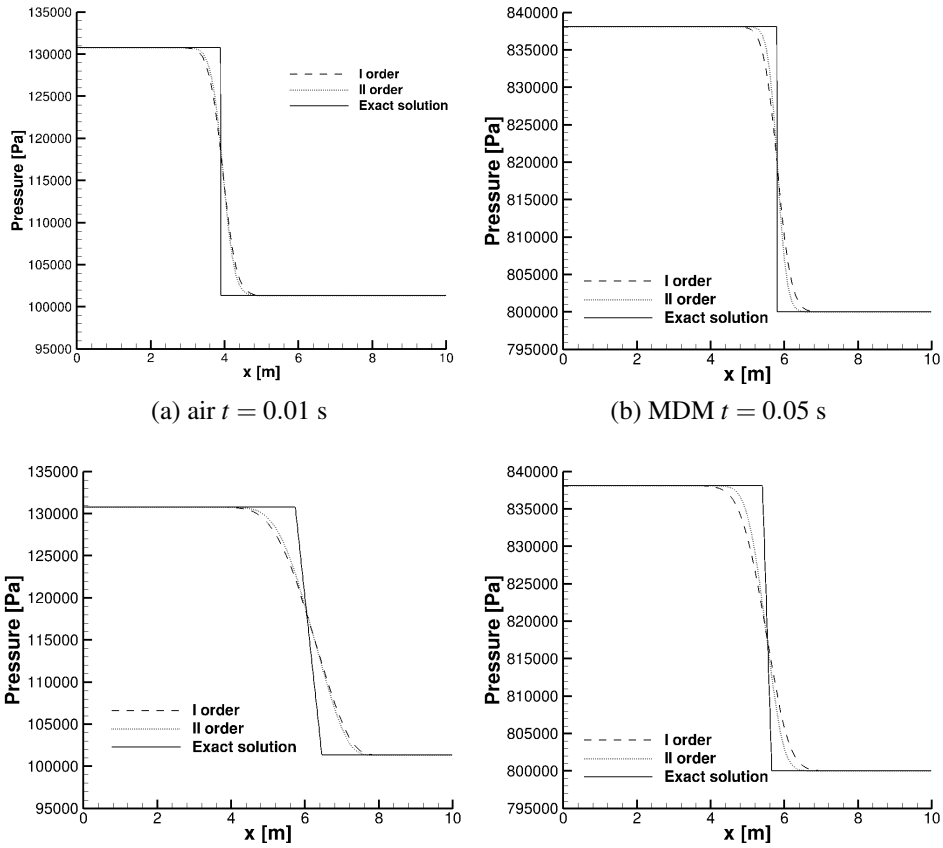

(a) air $t = 0.01$ s

(b) MDM $t = 0.05$ s

(c) air $t = 0.04$ s

(d) MDM $t = 0.13$ s

Figure 4.4: shock propagation within an open-end pipe. Analytic solution (continuous line), first order solution (dashed line) and second order solution (dotted curve); (a) Air: shock propagating rightwards; (b) MDM: shock propagating rightwards; (c) Air: rarefaction fan propagating leftwards; (d) MDM: rarefaction fan propagating leftwards;

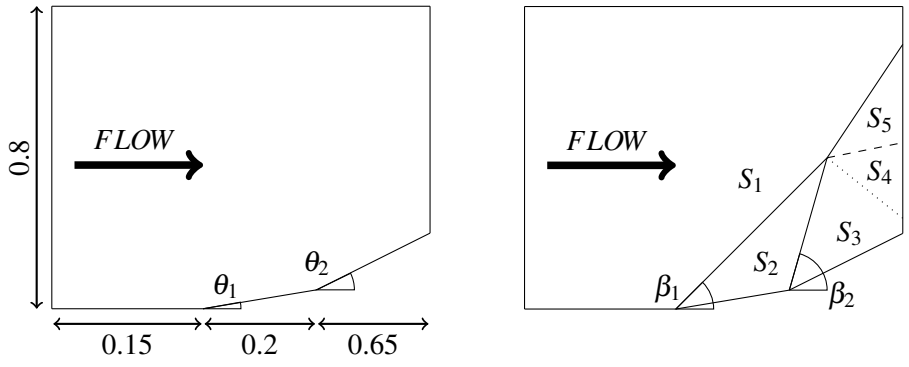

Figure 4.5: double wedge domain. Pictures are not to scale. (a) geometry: $\theta_1 = 10^\circ$ and $\theta_1 = 20^\circ$ w.r.t. the horizontal plane; (b) expected shock-wave pattern. S_n identifies the thermodynamic state corresponding to each of the five regions;

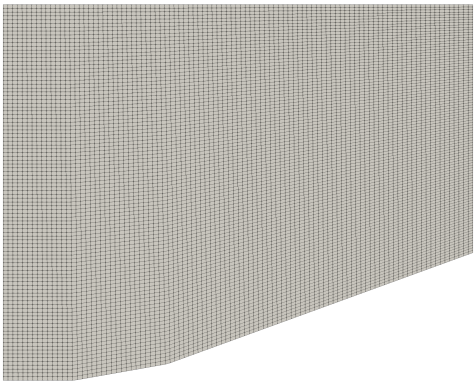

Figure 4.6: double wedge. Structured grid composed by 10^4 quadrilateral cells;

thus further complicating the domain downstream. Similarly, a rarefaction fan would be also reflected, giving rise to a non-simple region caused by the intersection of the incident and reflected characteristics lines. Here, we refer to zone 4 as the portion of the domain right after the shock (or the fan) and below the contact discontinuity that separates region 4 and 5. Namely, region 4 indicates the homogeneous region which is not interested by the propagation of waves reflected at the lower wall. Indeed, since the flow is steady, the direction of the stream and the value of the static pressure in zone 4 must necessarily be the same of region 5. A slip, or contact, surface (dashed line in Fig. 4.5(b)) is therefore generated in between zones 4 and 5.

Fig. 4.5(b) depicts the expected pattern and identifies the five characteristic uniform regions. The thermodynamic state of each zone n is identified with the following

notation S_n. Further information concerning the double ramp problem may be found in [33].

4.3.2.1 Ideal flow of MDM

The analytic solution of an ideal flow over the double-wedge geometry can be obtained by recursively applying the shock jump relations. It has to be point out that, in this test case, the siloxane MDM actually enters the domain in a non-ideal regime but the simple PIG model is used to describe its thermodynamics. Nevertheless, it is still possible to compare numerical results against theoretical predictions, given that the same EoS is employed. In the dilute gas limit, assuming a polytropic behavior, the shock angle β depends on the value of the Mach number only and the following relation applies:

$$\tan\Delta\theta = \frac{2\cot\beta\left(M_1^2\sin^2\beta - 1\right)}{\left(\gamma+1\right)M_1^2 - 2\left(M_1^2\sin^2\beta - 1\right)}, \tag{4.8}$$

Since $\Delta\theta_1 = 10°$, from Eq. (4.8), $\beta_1 = 31.3949°$. Once β is known, the flow can be decomposed into a normal and a tangent component w.r.t. the shock. The state of the fluid S_2 is then reconstructed exploiting the Rankine-Hugoniot condition. Moving further, the flows is turned a second time ($\Delta\theta_2 = 10°$). The theoretical angle $\beta_2 = 34.1594°$ and the state S_3 are again retrieved exploiting the jump relations. Between region 3 and 4, a rarefaction fan operates to match P_4 and P_5. Therefore, to reconstruct S_4 and S_5, one has to solve a system of coupled equations:

$$P_5 = \left[\frac{2\gamma}{\gamma+1}\left(M_1^2\sin^2\beta_{15} - 1\right) + 1\right]P_1\,, \tag{4.9a}$$

$$\tan\Delta\theta_{15} = \frac{2\cot\beta_{15}\left(M_1^2\sin^2\beta_{15} - 1\right)}{\left(\gamma+1\right)M_1^2 - 2\left(M_1^2\sin^2\beta_{15} - 1\right)}, \tag{4.9b}$$

$$P_4 = P_3^t\left[1 + \frac{\gamma-1}{2}M_4^2\right]^{-\frac{\gamma}{\gamma-1}}, \tag{4.9c}$$

$$\nu\left(M_4\right) = \Delta\theta_{34}^{rad} + \nu\left(M_3\right), \tag{4.9d}$$

$$\tag{4.9e}$$

The first equation is derived combining the continuity condition, the equation for the conservation of momentum across the shock and the Rankine-Hugoniot condition. The second equation is known as the *shock-polar relation* and it relates the flow turning angle to the angle of the shock and to the upstream Mach number. The third equation is the isentropic relation for pressure while the fourth equation is exploited to describe a supersonic Prandlt-Meyer expansion ($\nu\left(M_3\right)$ is the Prandlt-Meyer function). The unknowns are β_{15} (the angle of the shock-wave separating region 1 from

	S_1	S_2	S_3	S_4	S_5
$P\ [MPa]$	1.2600	1.9739	3.0020	2.9597	2.9597
$T\ [K]$	632.5000	636.1324	639.5294	639.4177	640.0357
$\rho\ [Kg/m^3]$	56.6709	88.2738	133.5345	131.6776	131.5504
$M\ [-]$	2.4000	2.1940	1.9845	1.9917	1.9515

Table 4.4: double wedge, supersonic ideal flow of MDM. Thermodynamic states predicted by the analytic procedure;

	$\Delta^{\bar{S}_2}_{err}\%$	$\Delta^{\bar{S}_3}_{err}\%$	$\Delta^{\bar{S}_4}_{err}\%$	$\Delta^{\bar{S}_5}_{err}\%$
$P\ [MPa]$	< 0.02	< 0.01	< 0.1	< 0.1
$T\ [K]$	< 0.01	< 0.01	< 0.01	< 0.02
$\rho\ [Kg/m^3]$	< 0.01	< 0.01	< 0.1	< 0.1
$M\ [-]$	< 0.02	< 0.04	< 0.2	< 0.3

Table 4.5: double wedge, supersonic ideal flow of MDM. Thermodynamic states computed using the numerical solver;

region 5), P_5, P_4, $\Delta\theta_{15}$ (the angle between flow direction before and after shock-wave 1-5), $\Delta\theta_{34}$ (the rotation of the flow expanding from region 3 to region 4) and M_4. Given that conditions $P_5 = P_4$ and $\Delta\theta_{15} = \Delta\theta_{34}$ must apply, the problem can be solved numerically yielding $\beta_{15} = 39.7870°$. S_4 from S_3 are reconstructed using the isentropic relations. S_5 can be obtained from S_1 by means of the Rankine-Hugoniot condition.

Tab. 4.4 summarizes the state of the fluid in the five region, as predicted via the analytic model. Results from the SU2 numerical solver are instead reported in Tab. 4.5. Percentage errors are well below 1% for all the considered quantities. The angle $\beta_{15} = 39.63°$ obtained from numerical simulations reveals an error of -0.39% w.r.t. the theoretical value.

Fig. 4.7(a-b) reports the Mach number and pressure fields for the ideal flow of MDM. A contact discontinuity is clearly visible in Fig. 4.7(a) while a non appreciable rarefaction fan occurs between region 3 and 4.

4.3.2.2 Non-ideal flow of MDM under the polytropic vdW model

The MDM flow problem is now studied using the vdW EoS to model the thermodynamic behavior. The conditions of the MDM fluid at the domain inlet were properly selected to enter the non-ideal thermodynamic region: the compressibility factor is $Z_c = 0.7559$ while $\Gamma = 0.6364$. Therefore, non-ideal effects are expected to play a relevant role. The resulting shock-wave pattern still follows the one depicted in Fig. 4.5(b).

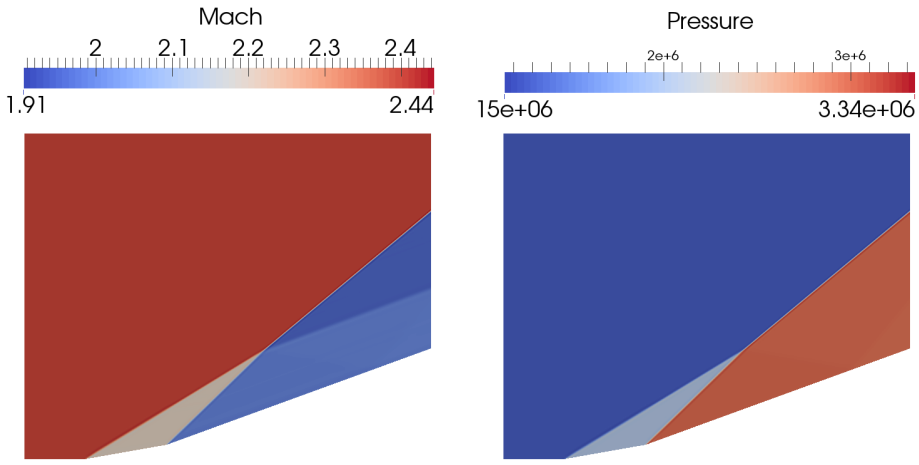

(a) (b)

Figure 4.7: double wedge. Numerical solution for an ideal supersonic flow of MDM. (a) Mach number field; (b) Pressure field;

Given the larger complexity of the vdW model, the verification of the numerical solver is carried out through an a-posteriori procedure. In particular, the verification is achieved by proving that the computed states do satisfy the shock adiabat which, for a vdW flow, reads:

$$P_2 = \frac{\frac{1-b\rho_1}{\rho_1(\gamma-1)}\left(P_1+a\rho_1^2\right)-a\rho_1-\frac{P_1}{2}\left(\frac{1}{\rho_2}-\frac{1}{\rho_1}\right)+a\left(1-\frac{1}{\gamma-1}\right)\rho_2+\frac{ab\rho_2^2}{(\gamma-1)}}{\left(\frac{1}{2}+\frac{1}{\gamma-1}\right)\frac{1}{\rho_2}-\left(\frac{1}{2\rho_1}+\frac{b}{\gamma-1}\right)}, \tag{4.10}$$

In the non-ideal regime, the value of the angle β depends also on the thermodynamic state of the fluid ahead of the shock:

$$\beta = \arcsin\sqrt{\frac{P_2-P_1}{\rho_2-\rho_1}\frac{\rho_2}{\rho_1}\frac{1}{c_1^2M_1^2}}, \tag{4.11}$$

Tab. 4.6 summarize the thermodynamic state of the fluid in each region, as computed using SU2. Integral relations, such as the Rankine-Hugoniot condition, are correctly satisfied and thermodynamic states are fairly reconstructed. Namely, from region 1 to 2 the percentage error $\varepsilon_{RH}^{12}\%$ between P_2 and $\bar{P}_2$ is well below 0.01%. From region 2 to 3 $\varepsilon_{RH}^{23} \approx -0.01\%$ and from region 1 to 5 $\varepsilon_{RH}^{15} \approx -0.01\%$. The errors are very limited thus providing an indication about the reliability of the non-ideal solver

	$\bar{S}_1$	$\bar{S}_2$	$\bar{S}_3$	$\bar{S}_4$	$\bar{S}_5$
$P\ [MPa]$	1.2600	1.7253	2.3104	2.3072	2.3042
$T\ [K]$	632.5000	637.1390	643.0800	643.0580	643.2910
$\rho\ [Kg/m^3]$	74.9693	121.3440	205.8930	205.4750	204.6620
$M\ [-]$	2.4000	2.7309	2.6187	2.62356	2.5950

Table 4.6: double wedge, supersonic vdW flow of MDM. Thermodynamic states computed using the numerical solver;

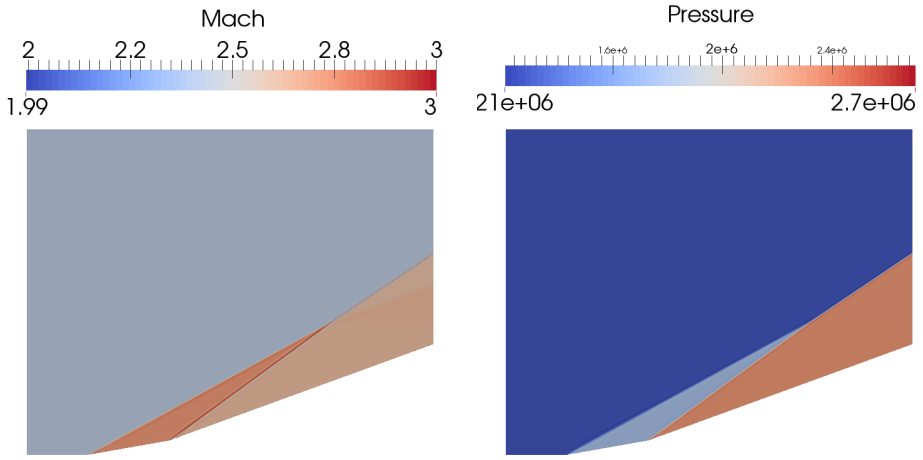

(a) (b)

Figure 4.8: double wedge. Numerical solution for a vdW supersonic flow of air. (a) Mach number field; (b) Pressure field;

predictions. On the shock angle, the error results $\varepsilon_\beta^{12} \approx -0.65\%$, $\varepsilon_\beta^{23} \approx -0.04\%$ and $\varepsilon_\beta^{15} \approx -0.53\%$. The Mach number and pressure fields are depicted in Fig. 4.8(a) and in Fig. 4.8(b). Fig. 4.8(a) reveals that the flow is far from being ideal as the solution features a non-ideal oblique shock waves. Indeed, the Mach number increases as the stream crosses the shock-wave separating region 1 from zone 2.

4.3.3 Non-Classical Rarefaction Shock Waves

In this section, the capabilities of the non-ideal solver are assessed for a non-classical flow. In thermodynamic conditions close to the critical point, fluids of complex molecules are supposed to allow for non-classical gas dynamic phenomena such as rarefaction shock waves or compression fans [34–40]. The non-classical region encloses all the possible states of a thermodynamic system, defined as a combination

	Density	Pressure	Temperature	Mach
S_A	0.79	1.06	1.01	1.70
S_B	0.45	0.93	1.00	1.19

Table 4.7: non-classical rarefaction shock wave. Fluid state, reduced with respect to the critical point, before and after the rarefaction shock-wave;

of pressure, temperature and density, that produce a negative value of $\Gamma < 0$ [41, 42]. The considered fluid is again MDM modeled under the polytropic gas assumption. Note that the admissibility of rarefaction shock waves strongly depends on the chosen EoS and state-of-the-art thermodynamic models do not predict a non-classical region for siloxane MDM, see [43]. The test case consists of a supersonic stream over an edge. The upstream state was properly selected to generate a non-classical rarefaction shock-wave. We identify the state of the fluid (S) ahead and past the discontinuity with the subscript A and B, respectively. For this particular test case, the value of the specific heat ratio at the inflow, as computed using FluidProp, corresponds to $\gamma = 1.0125$. The fluid enters the domain at conditions close to the critical point. Tab. 4.7 reports flow properties reduced by the critical values. The geometry consists of a simple domain containing an edge with slope $\theta = 15.945^\circ$, see Fig. 4.9(a). The fluid flows from left to right, viscosity and thermal conductivity effects are neglected. A second-order accurate implicit MUSCL scheme of Roe type was employed to model the numeric convective fluxes. Fig. 4.9(a) shows the Mach number flow field predicted using the PIG law. A rarefaction fan develops over the edge and the Mach number increases upon expansion. Fig. 4.9(b) reports the Mach number field as obtained using the vdW fluid model. Fig. 4.9(b) reveals the presence of a strong discontinuity which separates the domain into two uniform regions. The Mach number decreases across the shock. At the same time, a pressure and a density drop and an entropy increase are observed across the discontinuity, which therefore is identified as a non-classical rarefaction shock wave.

Fig. 4.11(a) reports a comparison of the pressure trend, as extracted along a horizontal line passing by y = 0.25, for the PIG, the vdW and the PR EoS. Pressure decreases gently across the fan in the fluid flow modeled as an ideal gas. On the other hand, pressure drops with a steeper gradient when the vdW or the PR EoS are employed. Fig. 4.10(a) and (b) report respectively the Mach number and density variation across the shock, as predicted from the diverse EoS. Clearly, Fig. 4.10(a) shows that, in the ideal regime, the Mach number increases upon expansion whereas the inverted behavior is found when using more accurate fluid models. Note that both the vdW and the PR EoS predict a non-monotonic variation of the Mach number across the shock, see [44]. On the other hand, as shown in Fig. 4.10(b) density always decreases across the shock. Similarly, in Fig. 4.11(b) the entropy variation (scaled by the nominal value at the domain inflow) is plotted for the PIG and the vdW gas

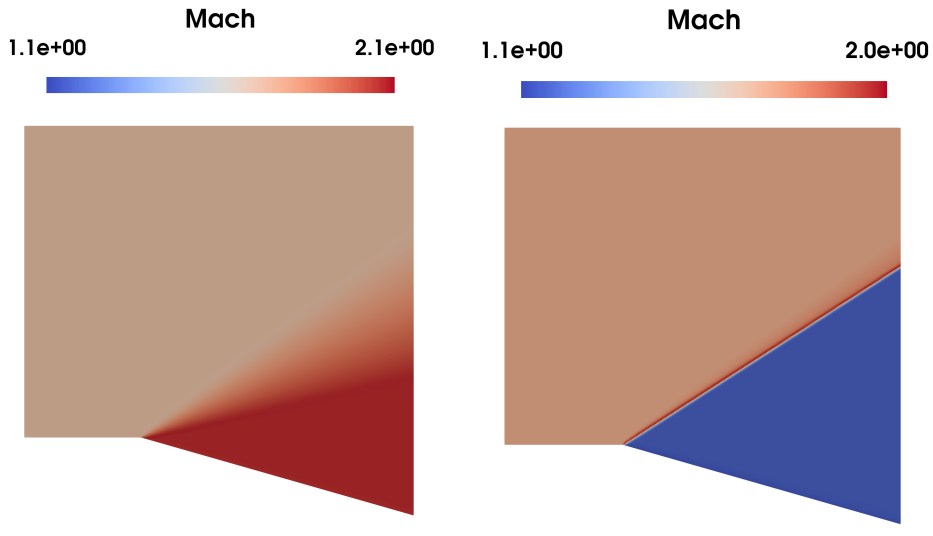

(a) (b)

Figure 4.9: non-classical rarefaction shock wave. (a) Mach flow field as computed using the PIG EoS, using mesh E; (b) Mach flow field as computed using the vdW EoS, using mesh E;

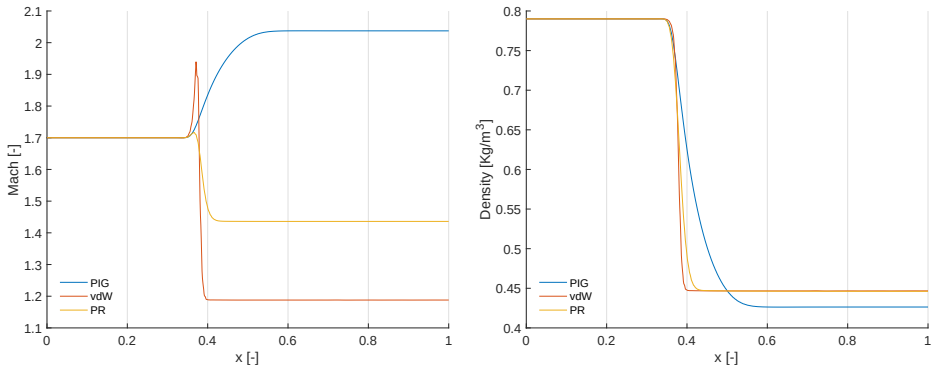

(a) (b)

Figure 4.10: non-classical rarefaction shock wave, properties variation along a straight line passing for $y = 0.25$. (a) Mach number; (b) Density;

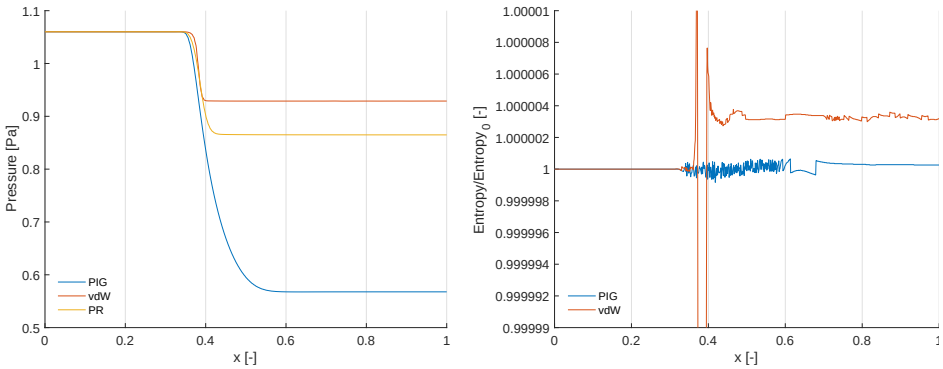

(a) (b)

Figure 4.11: non-classical rarefaction shock wave. (a) Pressure trends along $y = 0.25$ predicted using different EoS; (b) Entropy trends along $y = 0.25$ predicted using different EoS;

models. The PIG EoS is associated to a constant entropy, which further confirms the occurrence of a rarefaction fan, while the vdW model is associated to a (slight) entropy production across the discontinuity. Therefore, the vdW model predicts a non-classical rarefaction shock wave. Fig. 4.11(b) does not report the trend related to the flow modeled using the PR EoS as results show a non physical entropy destruction. This is in agreement with the findings from [43], where the authors prove that the PR EoS doesn't predict siloxane MDM to be endowed with a non-classical thermodynamic region. Tab. 4.7, reports the state of the fluid as computed past the shock (S_B). The deviation between the numerical and the theoretical value of p_B, computed using the shock adiabat for a vdW fluid (Eq 4.10, is approximately $5.3163 \cdot 10^{-5}\%$. The theoretical value $\beta = 32.8602°$ (Eq. 4.11) fairly compares the numerical outcome $\beta = 32.735°$.

Unstructured meshes of different resolution were used to evaluate the sensitivity of the solution w.r.t. the numerical grid. Namely, grid A (1200 grid nodes), grid B (4600 grid nodes), grid C (10000 grid nodes), grid D (28000 grid nodes) and grid E (63000 grid nodes). Fig. 4.12(a) and (b) depict the pressure profiles (extracted along the abscissa $y = 0.25$), for the different grids as resulting using the PIG and the vdW fluid models, respectively. In both cases, as the spatial resolution increases pressure trends converge to the very same solution. This confirms the consistency of the implemented algorithms.

4.3.4 Non-Ideal Expansion in a de Laval Nozzle

The test case regards the non-ideal expansion of a MDM flow within a planar converging-diverging nozzle. Further details about the geometry of the nozzle and test conditions are provided in the following chapter (Sec. 5.4.1). Through the nozzle, the fluid ac-

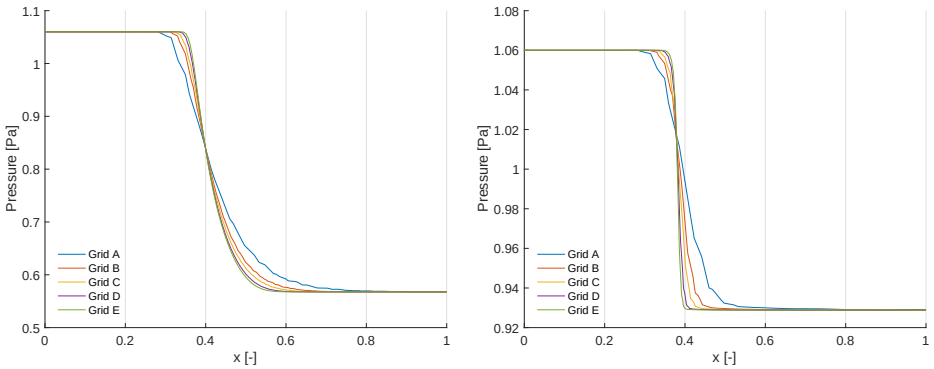

Figure 4.12: non-classical rarefaction shock wave, grid sensitivity analysis for pressure trend along $y = 0.25$. (a) Ideal MDM flow; (b) vdW MDM flow;

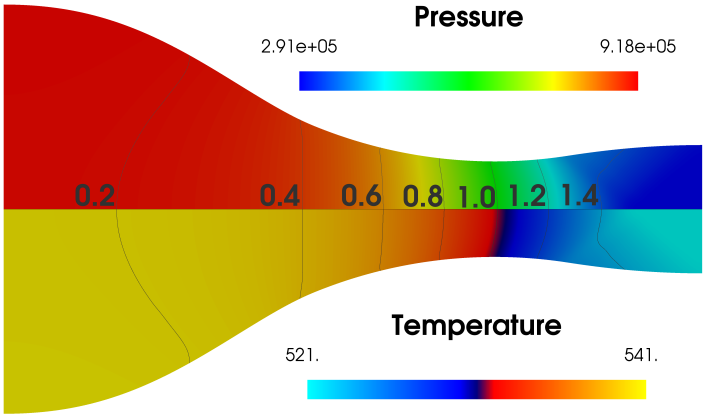

Figure 4.13: non-ideal expansion in a de Laval nozzle. Pressure (upper) and temperature (lower) fields as computed by the NICFD solver. Mach contours are also reported. Quantities vary smoothly along the axis of the nozzle while they are almost uniform over each sections;

celerates from still conditions up to a supersonic speed, whilst pressure and density decrease. The total conditions of the flow at the inlet of the nozzle correspond to $P^t = 919892.3$ Pa and $T^t = 540.685$ K. The EoS by [45] implemented in the Fluidprop library is used. Fig. 4.13 reports the pressure (upper) and temperature (lower) fields as resulting from numerical simulation, Mach contours are reported as well. The MDM flows from left to right, accelerating up to Mach ~ 1.5. Results confirm the expected quasi one-dimensional behavior: the Mach number, the density and the pressure are found to vary smoothly along the axis and to be almost constant across the section. Furthermore, isolines assume the expected parabolic shape. A grid sensitivity analysis is here reported, to evaluate the dependence of the solution w.r.t. the

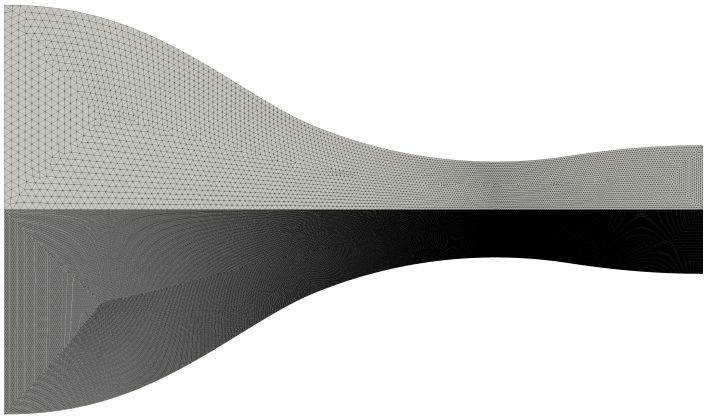

Figure 4.14: non-ideal expansion in a de Laval nozzle. Picture reports the coarser (upper side) and the finer (lower side) meshes used to conduct the grid sensitivity study;

computational grid. In particular, the variability of a few quantities (Mach, static pressure, entropy and total enthalpy) of interest was evaluated. The analysis is carried out assuming an inviscid and adiabatic flow. Since the geometry is symmetric along the nozzle centerline, only half of the domain is considered, to reduce the burden of numerical simulations. The coarser mesh includes almost 12k elements (6k points) while the finest one contains 415k elements (209k points). Fig. 4.14 reports the coarser (upper side) and the finer meshes (lower side).

Results are reported in Fig. 4.15: the Mach number and pressure trends along the nozzle centerline (repectively Fig. 4.15(a-b) show a very loose dependence on the selected spatial discretization. Indeed, the curves resulting from the different meshes are superimposed. On the other hand, the entropy (Fig. 4.15(c)) and the total enthalpy (Fig. 4.15(d) trends suffer a certain dependence on the numerical grid. Rigorously, given the inviscid and adiabatic flow assumptions the total enthalpy is a conserved quantity. Moreover, since apparently the flow features the absence of strong gradients (such as shock waves), the solution should be homoentropic. Nevertheless, results reveal a maximum variation, from the lowest to the largest value, in the order of $\approx 0.6\%$, for both quantities. This non-physical result is possibly due to numerical errors arising from the underlying algorithm implementation. However, the error is very limited and it does not question the validity of predictions from the SU2 non-ideal solver. In particular, it the close proximity of the nozzle discharge section the curves show a discontinuity which vanishes as the grids are refined. The discontinuity is possibly due to the presence of a very weak shock wave generated within the expander. Here, the nozzle is convex because it is designed to turn the flow in the direction parallel to the centerline. In numerical simulations, the convex shape is obtained by means of a discontinuous line which may be seen as a set of consecutive wedges. Each wedge generates a weak compressive wave and all the waves eventu-

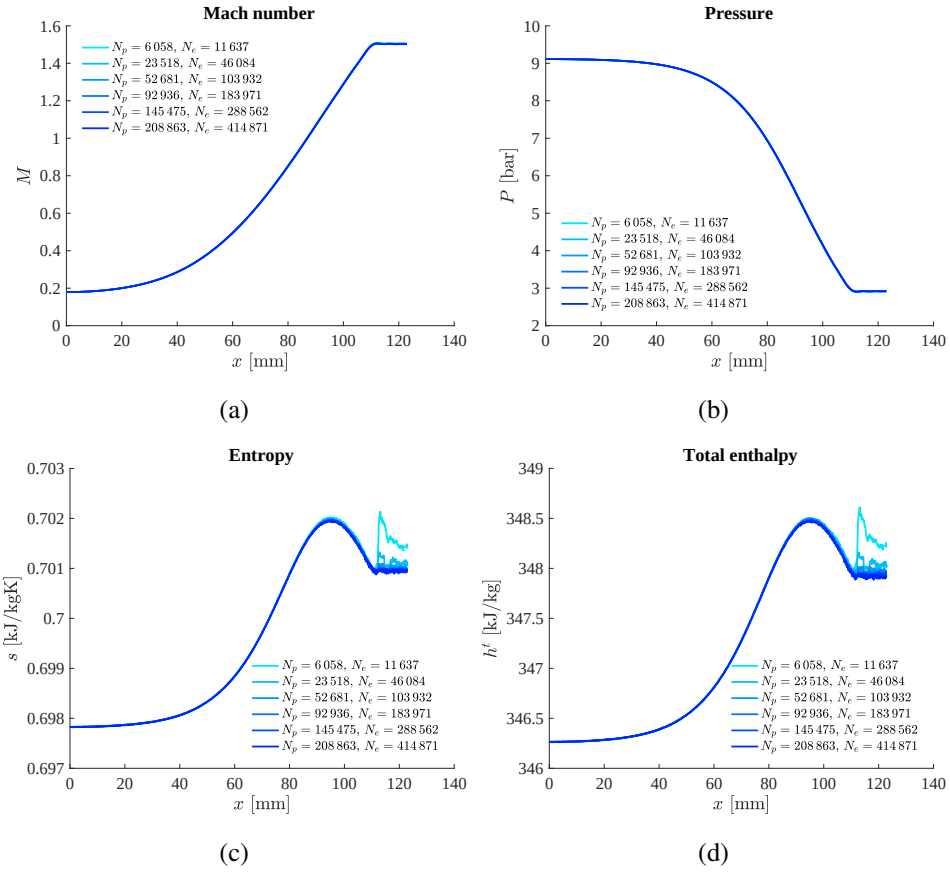

Figure 4.15: non-ideal expansion through a de Laval nozzle. Grid sensitivity analysis considering a symmetric domain. (a) Mach number trend along the centerline; (b) Pressure trend along the centerline; (c) Entropy trend along the centerline; (d) Total enthalpy trend along the centerline;

ally coalesce into a single shock that propagates downstream, intersecting the nozzle centerline. As the grid is refined, the entropy generation related to the shock reduces as the mesh is refined, until the discontinuity disappears.

4.3.5 Non-Ideal Turbulent Flow around an ORC Turbine Stator Blade

The Biere is a famous ORC blade geometry which is typically employed in supersonic axial turbine stators. The Biere represents a reference two-dimensional benchmark case to test the design of devices operating with siloxane fluid MDM (Octamethyltrisiloxane, $C_8H_{24}O_2Si_3$). In the following, the Reynolds-Averaged Navier-Stokes (RANS) model is employed. RANS simulations take advantage of both the

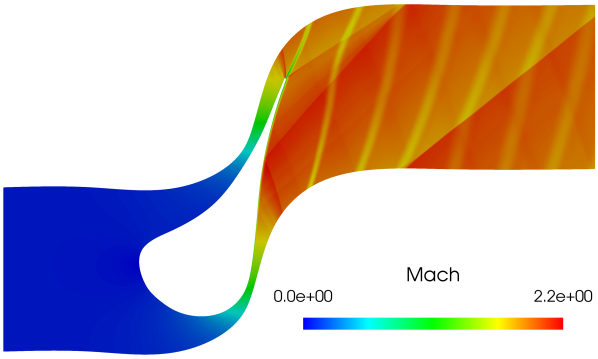

Figure 4.16: Numerical Mach flow-field around a typical ORC turbine blade;

Menter's Shear Stress Transport (SST) [46] and the Spalart-Allmaras (SA) [47] turbulence closures.

Fig. 4.16 reports the Mach number field computed over the finest mesh considered hereinafter (590k grid points). The numerical domain is periodic over the vertical axis (y) with a stagger spacing of 45 mm. The flow is simulated up to a distance of $0.5-0.6$ and 2 chord-lengths ahead and past the blade, respectively. The blade profile is meant to obtain a convergent-divergent cascade passage which serves to accelerate the fluid up to a largely supersonic speed. Across the cascade, the fluid is expanded from superheated conditions close to the saturation line ($\mathrm{P}^{\mathrm{T}}_{in} = 8$ bar, $\mathrm{T}^{\mathrm{T}}_{in} = 545.15$ K) to a static pressure in the order of $P \approx 1$ bar. As the flow past the cascade is largely supersonic (M ≈ 2 at the blade trailing edge), compressibility effects are known to play a key role. Indeed, because of the high flow Mach number achieved at the nozzle exit, a typical fish-tail shock pattern is generated downstream the trailing edge, see [48]. Moreover, shock-waves propagate through the vane and they interact with the boundary layer developing over the suction side of the neighboring blade.

In this section, the flow around the blade is computed using several grid of increasing resolution to compare the sensitivity of the numerical solution w.r.t. the spatial discretization. Namely, the Quantity of interest (QoI) are the pressure coefficient C_p distribution over the blade pressure and suction sides and the total pressure loss and entropy generation across the cascade. For the sake of clarity, the pressure coefficient is defined as

$$C_p(x/c) = \frac{P^s(x/c) - P^s_\infty}{\frac{1}{2}\rho_\infty V^2_\infty} \tag{4.12}$$

where c is the blade chord and $x \in [0, c]$ while the subscript ∞ points out the freestream values at the inlet (pressure P, density ρ and velocity V).

Hybrid meshes are generated using an in-house grid generator and they include,

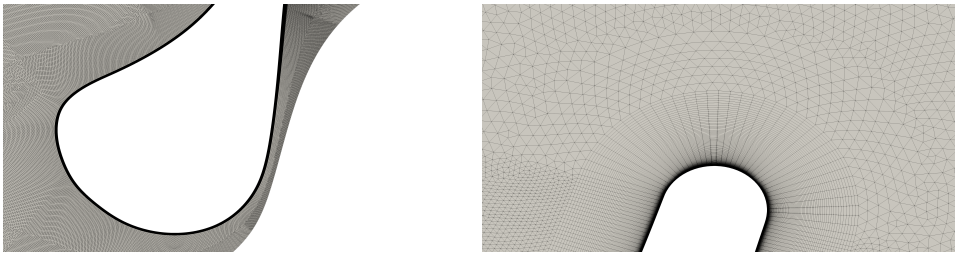

(a) (b)

Figure 4.17: enlargement of the 590k points grid in the close proximity of domain critical regions. (a) Blade leading edge; (b) Blade trailing edge;

respectively, 52k, 85k, 123k, 180k, 319k, and 590k grid points. Fig. 4.17(a) and (b) report an enlargement of the computational grid in the close proximity of the blade leading and trailing edges, respectively, for the 590k grid points mesh. CFD simulations rely on a generalized Approximate Riemann solver (ARS) of Roe type and they take advantage of the PR fluid model to describe the thermodynamics. An implicit Monotone Upstream-centered Schemes for Conservation Laws (MUSCL) scheme, with van Albada slope limiter, is used to ensure second order accuracy and mitigate spurious oscillations in the steady state solution. Non-Reflecting Boundary Conditions (NRBC) [49] are also implemented, to suppress the non-physical reflection of acoustic pressure perturbations at inflow and outflow boundaries.

Fig. 4.18(a) and Fig. 4.19(a) report the grid analysis w.r.t. the pressure coefficient distribution obtained using the SST and the SA turbulence models, respectively. Fig. 4.18(a) and Fig. 4.19(b) report an enlargement of the blade section characterized by the presence of an incident shock wave (corresponding to one of the fish-tail shock branches generated at the trailing edge). As highlighted by the referenced pictures, the pressure coefficient distribution converges as the grid resolution is increased. Note that, to avoid confusion, the distribution is reported only for a few selected grid. Nevertheless, results related to the other meshes are consistent with the convergence trend. Moreover, the different turbulence models yield very similar results.

Fig. 4.20(a) and (b) report the relative total pressure loss across the cascade as predicted using the diverse meshes, respectively for the SST and the SA turbulence models. The relative total pressure loss is defined as the QoI percentage difference w.r.t. the value obtained using the finest mesh. Again, for both closures the QoI shows a consistent trend as the predicted value converges by increasing the mesh spatial resolution. Eventually, the relative entropy generation is evaluated w.r.t. the finest mesh (Fig. 4.21(a) and (b) for the SST and the SA closures). Once again, results confirm the consistency of the numerical implementation.

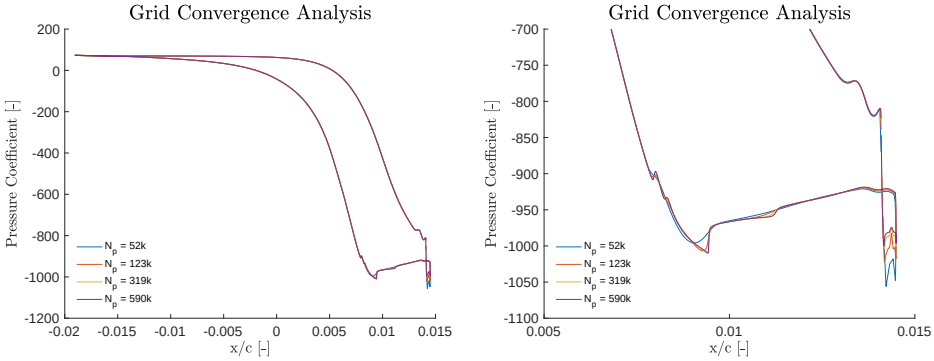

(a) (b)

Figure 4.18: pressure coefficient distribution computed using the SST closure model. (a) Coefficient distribution over the blade suction and pressure sides, for the whole chord length; (b) Coefficient distribution over the blade suction and pressure sides at the trailing edge section;

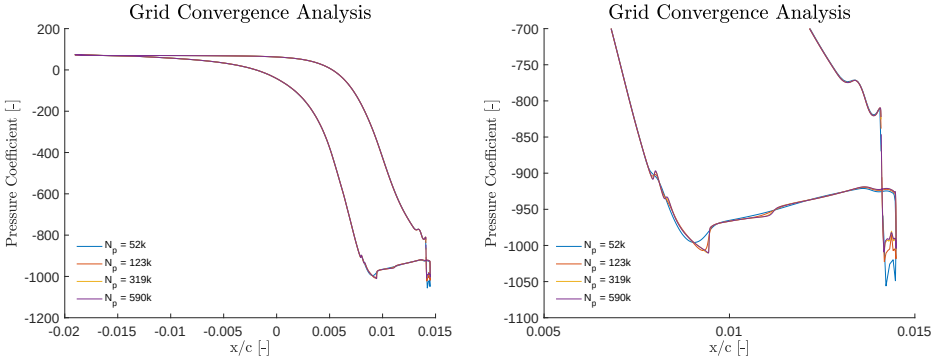

(a) (b)

Figure 4.19: pressure coefficient distribution computed using the SA closure model. (a) Coefficient distribution over the blade suction and pressure sides, for the whole chord length; (b) Coefficient distribution over the blade suction and pressure sides at the trailing edge section;

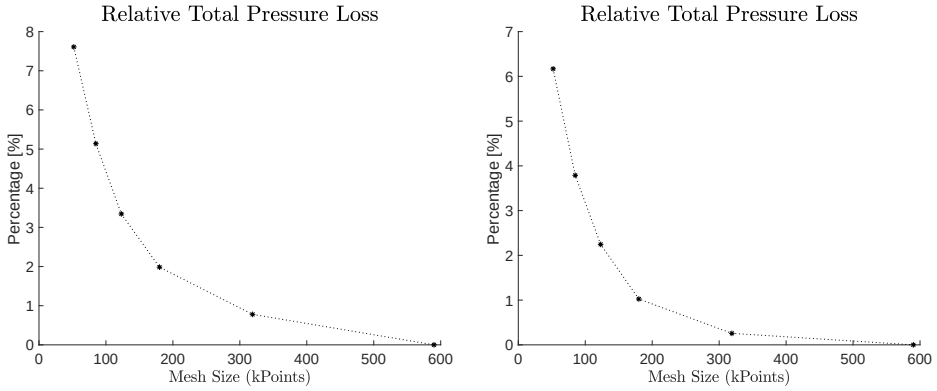

(a) (b)

Figure 4.20: grid sensitivity analysis. Relative total pressure loss across the cascade (w.r.t. the reference value computed using the finest mesh). (a) SST turbulence model; (b) SA turbulence model;

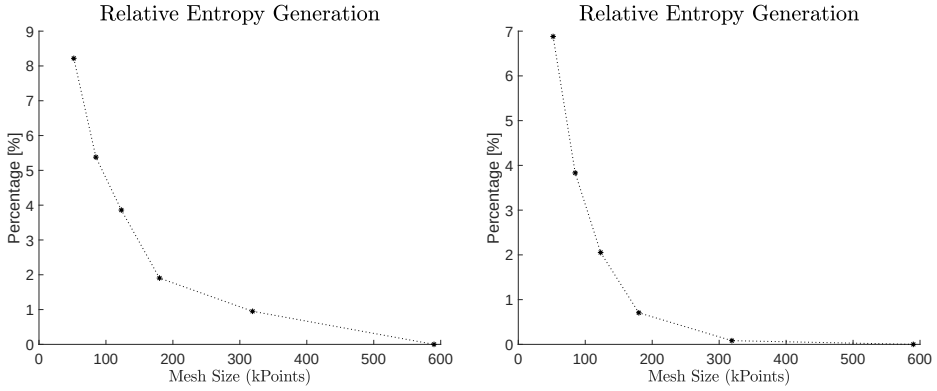

(a) (b)

Figure 4.21: grid sensitivity analysis. Relative entropy generation across the cascade (w.r.t. the reference value computed using the finest mesh). (a) SST turbulence model; (b) SA turbulence model;

4.4 Conclusions

In this chapter, the main characteristics of a non-ideal CFD solver were presented. Starting from the Navier-Stokes equations for compressible flows, the semi-discretized integral form of the PDE is defined over a standard median-dual vertex based grid. The equations are generalized, to accommodate complex EoS, and a brief summary of the most relevant differences a non-ideal solver must implement, with respect to an ideal one, are provided.

The capabilities of the SU2 non-ideal CFD solver were assessed by means of a comparison of numerical predictions against analytic solutions. The verification test cases included simple flow configurations involving fluids in the ideal, non-ideal and non-classical regime. Numerical results fairly compared to theoretical predictions, for all the test cases. The considered flows are well simulated by the CFD solver, thus confirming the validity of the CFD implementation.

References

[1] P. Colonna and S. Rebay. “Numerical simulation of dense gas flows on unstructured grids with an implicit high resolution upwind Euler solver”. In: *Int. J. Numer. Meth. Fluids* 46 (2004), pp. 735–765.

[2] R. Pecnik, V. E. Terrapon, F. Ham, G. Iaccarino, and H. Pitsch. “Reynolds-Averaged Navier-Stokes Simulations of the HyShot II Scramjet”. In: *AIAA Journal* 50.8 (2012), pp. 1717–1732.

[3] P. Colonna, T. P. der Stelt, and A. Guardone. *FluidProp: A program for the estimation of thermophysical properties of fluids*. Energy Technology Section, Delft University of Technology, The Netherlands. 2005.

[4] B. Re. “An adaptive interpolation-free conservative scheme for the three-dimensional Euler equations on dynamic meshes for aeronautical applications”. PhD thesis. Politecnico di Milano, 2016.

[5] P. Cinnella and P. Congedo. “Numerical solver for dense gas flows”. In: *AIAA Journal* 43.11 (2005), pp. 2458–2461.

[6] P. Cinnella. “Roe-type schemes for dense gas flow computations”. In: *Computers & Fluids* 35.10 (2006), pp. 1264–1281. ISSN: 0045-7930.

[7] E. Rinaldi. “Models and simulation of non-ideal fluid flows in unconventional turbomachinery: Toward highly efficient next-generation green power systems”. PhD thesis. TU Delft, 2015.

[8] R. Abgrall, P. Congedo, D. D. Santis, and N. Razaaly. “A non-linear residual distribution scheme for real-gas computations”. In: *Computers & Fluids* 102 (2014), pp. 148–169.

[9] P. M. Congedo, P. Cinnella, and C. E. Corre. “Efficient numerical simulation of three-dimensional Bethe-Zel’dovich-Thompson Fluid Flows”. In: *5th ECCOMAS*. Venice, Italy, 2008. URL: `https://hal.inria.fr/inria-00549372`.

[10] L. Sciacovelli, P. Cinnella, and X. Gloerfelt. “Direct numerical simulations of supersonic turbulent channel flows of dense gases”. In: *Journal of Fluid Mechanics* 821 (2017), 153?199. DOI: `10.1017/jfm.2017.237`.

[11] F. Palacios, M. R. Colonno, A. C. Aranake, A. Campos, S. R. Copeland, T. D. Economon, A. K. Lonkar, T. W. Lukaczyk, T. W. R. Taylor, and J. J. Alonso. “Stanford University Unstructured (SU^2): An open-source integrated computational environment for multi-physics simulation and design”. In: *AIAA Paper 2013-0287* 51st AIAA Aerospace Sciences Meeting and Exhibit (Jan. 2013).

[12] T. D. Economon, D. Mudigere, G. Bansal, A. Heinecke, F. Palacios, J. Park, M. Smelyanskiy, J. J. Alonso, and P. Dubey. “Performance optimizations for scalable implicit RANS calculations with SU2”. In: *Computers & Fluids* 129 (2016), pp. 146–158. ISSN: 0045-7930. DOI: `http://dx.doi.org/10.1016/j.compfluid.2016.02.003`. URL: `http://www.sciencedirect.com/science/article/pii/S0045793016300214`.

[13] S. Vitale, G. Gori, M. Pini, A. Guardone, T. D. Economon, F. Palacios, J. J. Alonso, and P. Colonna. “Extension of the SU2 open source CFD code to the simulation of turbulent flows of fluids modelled with complex thermophysical laws”. In: *22^{nd} AIAA Computational Fluid Dynamics Conference*. AIAA Paper 2760. 2015.

[14] G. Gori, A. Guardone, S. Vitale, A. Head, M. Pini, and P. Colonna. “Non-Ideal Compressible-Fluid Dynamics Simulation with SU2: Numerical Assessment of Nozzle and Blade Flows for Organic Rankine Cycle Applications”. In: *3rd International Seminar on ORC Power Systems*. Brussels, Belgium, Oct. 2015.

[15] M. Pini, S. Vitale, P. Colonna, G. Gori, A. Guardone, T. Economon, J. Alonso, and F. Palacios. "SU2: the Open-Source Software for Non-ideal Compressible Flows". In: vol. 821. 1. 2017, p. 012013.

[16] P. Roe. "Approximate Riemann solvers, parameter vectors and difference schemes". In: *Journal or Computational Physics* 43 (1981), pp. 357–372.

[17] J. Montagne and M. Vinokur. "Generalized flux-vector splitting and Roe average for an equilibrium real gas". In: *Journal of Computational Physics* 89.2 (1990), pp. 276–300.

[18] A. Guardone and L. Vigevano. "Roe linearization for the van der Waals gas". In: *J. Comput. Phys.* 175.1 (2002), pp. 50–78.

[19] E. Rinaldi, R. Pecnik, and P. Colonna. "Exact Jacobians for implicit navier-Stokes simulations of equilibrium real gas flows". In: *Journal of Computational Physics* (2014).

[20] V. Selmin. "The node-centred finite volume approach: bridge between finite differences and finite elements". In: *Comp. Meth. Appl. Mech. Engng.* 102 (1993), pp. 107–138.

[21] J. D. van der Waals. "Over de Continuïteit van den Gas - en Vloeistoftoestand (on the continuity of the gas and liquid state)". PhD thesis. Leiden University, 1873.

[22] D. Y. Peng and D. B. Robinson. "A New Two-constant Equation of State". In: *Ind. Eng. Chem. Fundam.* 15 (1976), pp. 59–64.

[23] T.-H. .-.-H. Chung, M. Ajlan, L. L. Lee, and K. E. Starling. "Generalized multiparameter correlation for nonpolar and polar fluid transport properties". In: *Ind. Eng. Chem. Res.* 27.4 (Apr. 1988), pp. 671–679. ISSN: 0888-5885. DOI: 10.1021/ie00076a024.

[24] D. Wilcox. *Turbulence Modeling for CFD*. 2nd Ed., DCW Industries, Inc., 1998.

[25] R. J. LeVeque. *Finite volume methods for conservation laws and hyperbolic systems*. Cambridge University Press, 2002.

[26] F. Palacios, T. D. Economon, A. Aranake, R. S. Copeland, A. Lonkar, T. Lukaczyk, D. E. Manosalvas, R. K. Naik, S. Padron, B. Tracey, A. Variyar, and J. J. Alonso. "Stanford university unstructured (SU2): Analysis and design technology for turbulent flows". In: *AIAA Paper 2014-0243* 52nd Aerospace Sciences Meeting (2014).

[27] T. D. Economon, F. Palacios, S. R. Copeland, T. W. Lukaczyk, and J. J. Alonso. "SU2: An Open-Source Suite for Multiphysics Simulation and Design". In: *AIAA Journal* 54.3 (2016/09/08 2015), pp. 828–846. DOI: 10.2514/1.J053813. URL: http://dx.doi.org/10.2514/1.J053813.

[28] R. Sanchez, H. Kline, D. Thomas, A. Variyar, M. Righi, D. T. Economon, J. J. Alonso, R. Palacios, G. Dimitriadis, and V. Terrapon. "Assessment of the fluid-structure interaction capabilities for aeronautical applications of the open-source solver SU2". In: *ECCOMAS, VII European Congress on Computational Methods in Applied Sciences and Engineering, Crete Island, Greece* (2016).

[29] P. A. Thompson. *Compressilbe Fluid Dynamics*. McGraw-Hill, 1988.

[30] L. P. Quartapelle, Castelletti, A. Guardone, and G. Quaranta. "Solution of the Riemann problem of classical gasdynamics". In: *Journal of Coputational Physics* 190 (2003), p. 2003.

[31] R. J. LeVeque. *Numerical methods for conservation laws*. Lectures in Mathematics, ETH Zurich, 1992.

[32] E. F. Toro. "The HLL and HLLC Riemann Solvers". In: *Riemann Solvers and Numerical Methods for Fluid Dynamics: A Practical Introduction*. Berlin, Heidelberg: Springer Berlin Heidelberg, 1997, pp. 293–311. ISBN: 978-3-662-03490-3. DOI: 10.1007/978-3-662-03490-3_10. URL: https://doi.org/10.1007/978-3-662-03490-3_10.

[33] B. Edney. “Anomalous Heat Transfer and Pressure Distributions on Blunt Bodies at Hypersonic Speeds in the Presence of an Impinging Shock”. In: FFA–115 (Jan. 1968).

[34] P. A. Thompson. “A fundamental derivative in gasdynamics”. In: *Phys. Fluids* 14.9 (1971), pp. 1843–1849.

[35] P. A. Thompson and K. C. Lambrakis. “Negative Shock Waves”. In: *J. Fluid Mech.* 60 (1973), pp. 187–208.

[36] M. S. Cramer and A. Kluwick. “On the Propagation of Waves Exhibiting Both Positive and Negative Nonlinearity”. In: *J. Fluid Mech.* 142 (1984), pp. 9–37.

[37] M. S. Cramer and R. Sen. “Shock formation in fluids having embedded regions of negative nonlinearity”. In: *Phys. Fluids* 29 (1986), pp. 2181–2191.

[38] M. S. Cramer and R. Sen. “Exact solutions for sonic shocks in van der Waals gases”. In: *Phys. Fluids* 30 (1987), pp. 377–385.

[39] R. Menikoff and B. J. Plohr. “The Riemann problem for fluid flow of real material”. In: *Rev. Mod. Phys.* 61(1) (1989), pp. 75–130.

[40] J. W. Bates and D. C. Montgomery. “Some numerical studies of exotic shock wave behavior”. In: *Phys. Fluids* 11.2 (1999), pp. 462–475. DOI: http://dx.doi.org/10.1063/1.869862. URL: http://scitation.aip.org/content/aip/journal/pof2/11/2/10.1063/1.869862.

[41] C. Zamfirescu, A. Guardone, and P. Colonna. “Admissibility region for rarefaction shock waves in dense gases”. In: *J. Fluid Mech.* 599 (Mar. 2008), pp. 363–381.

[42] A. Guardone, C. Zamfirescu, and P. Colonna. “Maximum intensity of rarefaction shock waves for dense gases”. In: *Journal of Fluid Mechanics* 642 (2010), pp. 127–146.

[43] P. Colonna, A. Guardone, and N. R. Nannan. “Siloxanes: a new class of candidate Bethe-Zel’dovich-Thompson fluids”. In: *Phys. Fluids* 19.10 (2007), pp. 086102-1-12.

[44] A. Kluwick. “Handbook of Shock Waves”. In: ed. by G. Ben-Dor, O. Igra, and T. Elperin. Academic Press, 2001, pp. 339–411.

[45] M. Thol, F. H. Dubberke, E. Baumhögger, J. Vrabec, and R. Span. “Speed of Sound Measurements and Fundamental Equations of State for Octamethyltrisiloxane and Decamethyltetrasiloxane”. In: *Journal of Chemical & Engineering Data* 62.9 (2017), pp. 2633–2648.

[46] F. Menter. “Zonal Two Equation $k-\omega$, Turbulence Models for Aerodynamic Flows”. In: *AIAA Paper* 93-2906 (1993).

[47] P. Spalart and S. Allmaras. “A one-equation turbulence model for aerodynamic flows”. In: *AIAA Paper 1992-0439* (1992).

[48] B. Saracoglu, G. Paniagua, J. Sanchez, and P. Rambaud. “Effects of blunt trailing edge flow discharge in supersonic regime”. In: *Computers & Fluids* 88 (2013), pp. 200–209.

[49] M. B. Giles. “Nonreflecting boundary conditions for Euler equation calculations”. In: *AIAA Journal* 28 (Dec. 1990), pp. 2050–2058. DOI: 10.2514/3.10521.

CHAPTER 5

ASSESSMENT OF THE NON-IDEAL THERMODYNAMIC MODEL ACCURACY

Part of the contents of this chapter appear in

G. Gori, M. Zocca, G. Cammi, A. Spinelli and A. Guardone, *Experimental assessment of the open-source SU2 CFD suite for ORC applications*, Energy Procedia, Vol. 129, 2017

5.1 Introduction

The SU2 an open-source suite [1, 2] was recently generalized to deal with non-ideal, fully turbulent, flows and it now embodies the reference among NICFD solvers. In the limited framework of ideal flows of air, the reliability of the SU2 suite was already extensively assessed in earlier works, see for instance [1–5]. Preliminary verification of the SU2 NICFD solver implementation can be found in [6–8] while a preliminar experimental assessment is presented in [9]. A fundamental step of model validation [10] is the assessment of its accuracy. This process aims at evaluating the capability of a given model, implemented within a computer code, to predict a specified physical phenomenon. Despite the cited works, none of the currently available fluid models for non-ideal flows was ever assessed against real experimental measurements in the NICFD regime. The present chapter reports the first-ever experimental assessment of a Non-Ideal Compressible-Fluid Dynamics (NICFD) model.

The experimental test set considered to carry out the assessment includes flow configurations of practical interest for renewable energy applications. More precisely, experiments aim at reproducing the supersonic flow of MDM within turbine vanes in ORC power production systems. In turbomachinery applications, three different region of interest can be identified along the turbine vane, each region featuring characteristic traits. With reference to see Fig. 5.1, the fluid first enters the domain, on the left, and it undergoes an isentropic expansion that accelerates the flow to supersonic speed. This occurs in region *A*, where the portion of the domain in between two blades resembles a de Laval converging-diverging nozzle. Afterwards, the uniform stream past the turbine vane is crossed by an oblique shock (region *B*). Here, the shock-wave propagates in the domain and it interacts with the boundary layer developing over the suction side of the lower blade. Shock waves are generated at each blade trailing edge, where the characteristic fish-tail shock pattern is formed (region *C*). These typical flow configurations, involving fluid flows in mildly-to-highly non-ideal regimes, are reproduced numerically, using the non-ideal solver from SU2. Results are then compared against pressure and Mach number measurements collected at the Compressible-fluid dynamics for Renewable Energy Applications (CREA) laboratory of Politecnico di Milano, using the Test-Rig for Organic VApours (TROVA) [11–13].

The process takes advantage of an Uncertainty Quantification (UQ) analysis [10], to assess the role of aleatory uncertainties on the nominal test conditions and thus to

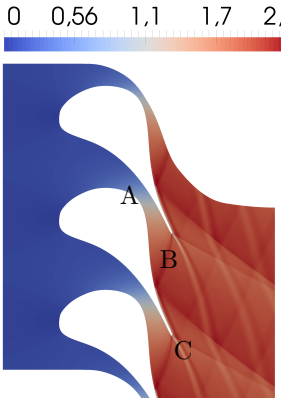

Mach number field around a turbine stator for ORC applications. Three different flow configurations were identified:

A Converging-diverging nozzle

B Oblique shock-wave and shock-boundary-layer interaction

C Fishtail shock pattern at the blade trailing edge

Figure 5.1: characteristic flow regions across an ORC turbine stator;

quantify the validity and robustness of SU2 predictions. In the chapter, the Uncertainty Quantification framework is introduced in Sec. 5.3. Sec. 5.4 describes the considered test cases and it reports the outcome of the assessment. Eventually, Sec. 5.5 summarizes the content of the chapter.

5.2 The TROVA test-rig

The TROVA is a blow-down facility designed to investigate the expansion of molecular complex fluids in the NICFD region of interest for ORC applications. In a blow-down facility, a high-pressure reservoir empties during the experimental run. Therefore, operating conditions change over time. However, in all the test cases reported hereinafter the flow within the TROVA test section is simulated assuming steady upstream conditions. Indeed, the characteristic time of the unsteady flow is negligible w.r.t. reservoir emptying time. This latter assumption is confirmed by experimental observations which prove negligible flow unsteadiness over the considered time scale, see [14]. For each case, the inflow conditions correspond to those measured at specific time instances during the discharge.

In the test chamber, diverse nozzle profiles may be easily assembled, to achieve the desired expansion rate. At the discharge section, an experimental body such as a turbine blade (or an airfoil), may be placed to investigate peculiar flow features, including oblique shock waves. Within the test section, probes are mounted at selected stations, to record the value of static pressure in time. Temperature and pressure are also monitored within the settling chamber, ahead of the test section. The experimental data set consists of static pressure measurements complemented with their related uncertainty (2σ range), evaluated by considering the whole measurement chain.

Moreover, Mach number measurements are available as well. Indeed, the TROVA test-rig is equipped with an optical schlieren apparatus that provides images of the

density gradient field [14, 15] in the test section. Schlieren images can be exploited to measure the Mach number, allowing to gather further information which are beneficial to strengthen the assessment. Briefly, small flaws due to machining, which are found over the test section walls, produce small perturbations that propagate as Mach waves into the stream. Following [16], a line-detection algorithm is applied to schlieren frames to determine the slope of the Mach waves μ. From the well-known relation $M = 1/\sin\mu$, direct measurement of the local Mach number is carried out. The uncertainty related to the experimental measure of the angle of the wave is assumed to be half of the angular resolution, given that this latter quantity depends on the resolution of the schlieren image, see [17].

5.3 Uncertainty Quantification

Reality is necessarily affected by uncertainty which can be classified as either aleatoric or epistemic. When dealing with numerical computations, one must keep in mind that the nominal conditions considered for the simulation hardly occur in practical applications. Here, aleatory uncertainties are mainly due to the process of retrieving the exact state of the fluid through measurements. Therefore, the boundary conditions one must apply, say for instance at the inlet, are not exact but they lie in a range of possible values. Epistemic uncertainties are instead related to a lack of knowledge regarding the physics of the problem. For instance, they might be due to some approximation made to model the thermodynamic behavior of the fluid. One of the goal of Uncertainty Quantification is to account for such uncertainties (on both parameters and measurements) in order to *quantify* the statistical variability of a Quantity of Interest (QoI).

In the assessment process, uncertainties are propagated through the solver, to compute the statistical moments of selected outputs. This allows for a more robust and comprehensive comparison of numerical outputs against experimental data. In order to carry out this process, an efficient stochastic method is presented in the next section.

5.3.1 Forward Uncertainty Quantification method

A non-intrusive Polynomial Chaos Expansions (PCE) approach (see Ref. [18]) is adopted here. In non-intrusive methods, a single deterministic computation is replaced by a whole set of similar computations, each of which (called a *realization*) being run for specific values of the uncertain conditions. PCE are derived from the original theory of Wiener on spectral representation of stochastic processes, using Gaussian random variables. Let ξ be a vector of standard independent random variables $\xi_i, i = 1, 2, \cdots, n_\xi$. Any well-behaved process u (i.e., a second-order process, then with a finite variance) can be expanded in a convergent (in the mean square

sense) series of the form

$$u(\mathbf{x},t,\xi) = \sum_{\alpha} u_{\alpha}(\mathbf{x},t)\Psi_{\alpha}(\xi)\,, \tag{5.1}$$

where α are multi-indices, $\alpha = (\alpha_1, \alpha_2, ..., \alpha_n)$. Each component $\alpha_i = 0, 1, ...,$ and Ψ_{α} are multivariate polynomial functions orthogonal with respect to the probability distribution function of the vector ξ. Each Ψ_{α} is defined by a product of orthogonal polynomials $\Phi_i^{\alpha_i}(\xi_i)$. That is, $\Psi_{\alpha}(\xi) = \prod_{i=1}^{n_\xi} \Phi_i^{\alpha_i}(\xi_i)$, where each $\Phi_i^{\alpha_i}$ is a polynomial of degree α_i, so that the degree of Ψ_{α} is $|\alpha|_1 = \sum_{i=1}^{n_\xi} \alpha_i$. A one-to-one correspondence exists between the choice of stochastic variable ξ_i and the polynomials $\Phi_i^{\alpha_i}(\xi_i)$. For instance, if ξ_i is a normal/uniform variable, the corresponding $\Phi_i^{\alpha_i}(\xi_i)$ are Hermite/Legendre polynomials of degree α_i. Coefficients $u_{\alpha}(x,t)$ are called PCE coefficients of the random process u.

For practical use, PCEs are truncated to a degree No

$$u(\mathbf{x},t,\xi) = \sum_{|\alpha|_1 \leq \mathrm{No}} u_{\alpha}(\mathbf{x},t)\Psi_{\alpha}(\xi)\,, \tag{5.2}$$

The number of multivariate polynomials Ψ_{α} i.e., the dimension of the expansion basis, is related to the stochastic dimension n_ξ and the degree No of polynomials and it is given by the formula $(n_\xi + \mathrm{No})!/(n_\xi!\mathrm{No}!)$.

Several approaches can be used to estimate PCE coefficients. The approach used in this study is based on quadrature formulae (see Ref. [18] for details). The PCE coefficients are evaluated from a set of abscissas and weights (ξ_i, ω_i) as follows

$$u_{\alpha}(\mathbf{x},t) = \|\Psi_{\alpha}\|^{-2} \sum_{i=1}^{n} u(\mathbf{x},t,\xi_i)\Psi_{\alpha}(\xi_i)\omega_i\,, \tag{5.3}$$

where n refers to the number of quadrature points, depending on the quadrature formula.

From the PCE of the random process, it is then straightforward to compute the mean (E) and variance (V) of the random process $u(\mathbf{x},t)$ and to estimate sensitivity information using the ANalysis Of VAriance decomposition (ANOVA) [18] as follows

$$E(u(\mathbf{x},t)) = u_0(\mathbf{x},t),\;\; V(u(\mathbf{x},t)) = \sum_{\alpha} u_{\alpha}^2(\mathbf{x},t)\,, \tag{5.4}$$

ANOVA relies on the decomposition of the variance according to the contribution of each uncertainty. This allows to identify the contribution of a given stochastic parameter to the total variance of an output quantity. Within a PCE framework, this can be easily achieved by exploiting some interesting properties of the previous development. Indeed, the variance decomposition of the response can be written as follows:

$$V(u) = \sum_{u \subseteq U} \sigma_u^2\,(X_u)\,, \tag{5.5}$$

where $U = (1, 2, \cdots, n_\xi)$ is the set of random variables indexes and σ_u^2 is the variance introduced by interactions of random variables $X_u \subseteq X_U$. From a PC expansion it is easy to compute all variances terms σ_u^2 of X_u equivalent to ξ_u i.e., $\sigma_u^2 = \sum_{\alpha \geq u} u_\alpha^2$, with the notation $\alpha \geq u \Rightarrow \alpha_i \geq u_i \forall i = 1, 2, \cdots, n_\xi$. The associated sensitivity measure of X_u, named Sobol's index, is written as the correlation ratio:

$$S_u = \frac{\sum_{v \leq u} \sigma_v^2}{V(u)}, \tag{5.6}$$

For more details, the reader is referred to Ref. [18].

5.3.2 Uncertainty Characterization

Several papers addressed the problem of quantifying uncertainties in the numerical simulation of non-ideal flows. Some of these papers [19–21] specifically focused the attention on the uncertainties affecting the thermodynamic models. In other works [22–24], multiple sources of uncertainties have been taken into account, both on operating conditions and thermodynamic models. According to the conclusions presented in these works, the uncertainties related to the thermodynamic model can be neglected with respect to the ones related to the operating conditions of the experimental facility.

With reference to the experiments carried out in the TROVA test-rig at Politecnico di Milano, the value of total pressure in the settling chamber ahead of the test section is given with its 2σ range. In particular, for every pressure transducers, calibration cycles were carried out at different temperatures. Therefore, the extended uncertainties for pressure probes consists of a function of the temperature. The uncertainty affecting the measured total temperature, ahead of the test section, was also considered. Thermocouples and pressure transducers were calibrated taking into account the actual measurement chain employed during the experiment. Gaussian Probability Density Funcion (PDF) distribution are systematically considered for all the parameters.

The uncertainties are then propagated through the numerical CFD solver. The output statistics, complemented with their numerical 2σ range, are compared against the experimental measurements and their associated tolerances.

In one of the benchmark cases involving a supersonic flow around an airfoil, the geometrical uncertainty related to the angular position of the airfoil is also considered (Sec. 5.4.2, second part). The true value of the angle of attack is assumed to be included within a symmetric range $\pm 0.5^\circ$ around the neutral position, with a uniform probability distribution.

For each test-case, PCE surrogate models are reconstructed using a Gauss-quadrature formulae that tensorizes 1D polynomials with order five in each direction. This procedure yields the definition of a Design of Experiment (DoE), namely a list of diverse

combinations of uncertain parameters. For each combination, a realization i.e., a deterministic CFD simulation, is carried out. The collection of the realizations allow to compute the coefficient of the PCE and thus obtain the meta-model. The PCE approximation i.e., the number of sampling points along each dimension of the probabilistic space, has been chosen relying on a convergence analysis (not reported here).

5.4 Experimental Assessment

The test cases considered hereinafter aim at reproducing the three characteristic regions found in a supersonic flow past a turbine vane, as pointed out in Fig.5.1. Sec. 5.4.1 presents results related to non-ideal flows expanding through a converging-diverging nozzle. Sec. 5.4.2 refers to the supersonic non-ideal flow around two different diamond-shaped airfoils. Eventually, Sec. 5.4.3 reports an assessment of a converging-diverging nozzle characterized by a small step wrought in correspondence of the throat section. The presence of the step results in the formation of two symmetric shocks that propagates downstream.

In the experiments, the state of the fluid, siloxane MDM, was properly selected to span from mild-to-high non-ideal regimes. The Helmholtz EoS in [25], implemented in the FluidProp library, is used as reference fluid model for MDM and it was employed in the computations presented hereinafter. Whenever the FluidProp library is not employed, the polytropic PR and the PIG are also used, to provide comparisons and assess the accuracy of the different fluid models. In this work, SU2 was coupled to a mesh adaptation software, to improve the grids quality in regions of steep gradients. The mesh adaptation technique is based on local error estimates of density gradients and it is detailed in [26].

5.4.1 Non-Ideal Expanding Flows

The first test case is representative of the flow-field developing in ORC turbine vanes. The test section consists of a planar converging-diverging nozzle and the experiment aims at reproducing the isentropic expansion of a siloxane MDM flow in a non-ideal regime. Further details regarding the geometry and the test-rig set-up can be found in [14] and [15]. As mentioned in Sec. 5.2, the TROVA is a blowdown facility and, as the high-pressure reservoir empties, the flow encompasses highly non-ideal to ideal regimes. In the following, 5 time instances (A-E) were selected during a discharge. At each instance, inflow conditions are known from measurements and the corresponding steady flow is simulated.

Two different discharges (labeled 1 and 2) were considered, for a total number of 10 test configurations. Tab. 5.1 and Tab. 5.2 report the total pressure and temperature, as measured at the nozzle inlet, at each time instance (A-E) for discharge 1 and 2, respectively. The compressibility factor for the considered conditions, computed using the reference EoS [25], spans from $Z \approx 0.63$ to $Z \approx 1$. Fig. 5.2 reports the T-s dia-

Exp	Total Pressure		Total Temperature		FluidProp Values	
	P^t [Pa]	U_{P^t}	T^t [K]	U_{T^t}	Z [-]	γ [-]
A_1	919892.3	911.1	540.677955	1.2	0.63322	1.017755
B_1	850791.7	912.6	547.529382	1.2	0.70000	1.017627
C_1	623982.1	912.1	548.462646	1.2	0.80000	1.017610
D_1	327193.8	911.0	543.756790	1.2	0.90000	1.017697
E_1	83658.3	911.2	537.382229	1.2	0.97465	1.017817

Table 5.1: non-ideal expanding flows, discharge 1. Nominal operating conditions P^t and T^t and the corresponding 2σ range;

Exp	Total Pressure		Total Temperature		FluidProp Values	
	P^t [Pa]	U_{P^t}	T^t [K]	U_{T^t}	Z [-]	γ [-]
A_2	458569.3	921.6	512.566216	1.2	0.81046	1.0183170
B_2	395977.3	921.3	519.451403	1.2	0.85000	1.0183173
C_2	269061.1	920.3	515.973949	1.2	0.90000	1.018246
D_2	128935.1	919.8	504.327991	1.2	0.95000	1.018495
E_2	52215.1	919.8	502.877009	1.2	0.98000	1.018527

Table 5.2: non-ideal expanding flows, discharge 2. Nominal operating conditions P^t and T^t and the corresponding 2σ range;

gram for MDM, color scale points out the compressibility factor Z. On the diagram, the $A_1 - E_1$ and $A_2 - E_2$ expansions are plotted (colored lines). The liquid-vapor saturation curve (black bold line) reveals that MDM is endowed with a *retrograde* behavior. Thanks to the retrograde behavior, it is possible to achieve an isentropic expansion from the saturated vapor line towards the superheated region, avoiding the detrimental formation of moisture.

The TROVA is equipped to carry out static pressure measurements at fixed locations along the test section, see Fig. 5.3(a). Tab. 5.3 and Tab. 5.4 report the values of the static pressure, as measured at p1-p4 stations (the position of probes varies from discharge 1 to 2), together with their expanded uncertainty.

Fig. 5.3(b) reports a schlieren image of the test section, centered on the nozzle divergent, during the experimental run labeled A_2. The image reveals an almost uniform flow: weak waves arise from small flaws along the upper and lower wall surfaces. No shock waves or detachments are detected. Test conditions result in an under-expanded supersonic flow: two symmetrical rarefaction fans are clearly visible past the discharge section (dark triangular regions on the right hand side of Fig. 5.3(b)). The same result applies for all the considered inflow conditions $A_1 - E_1$ and $A_2 - E_2$.

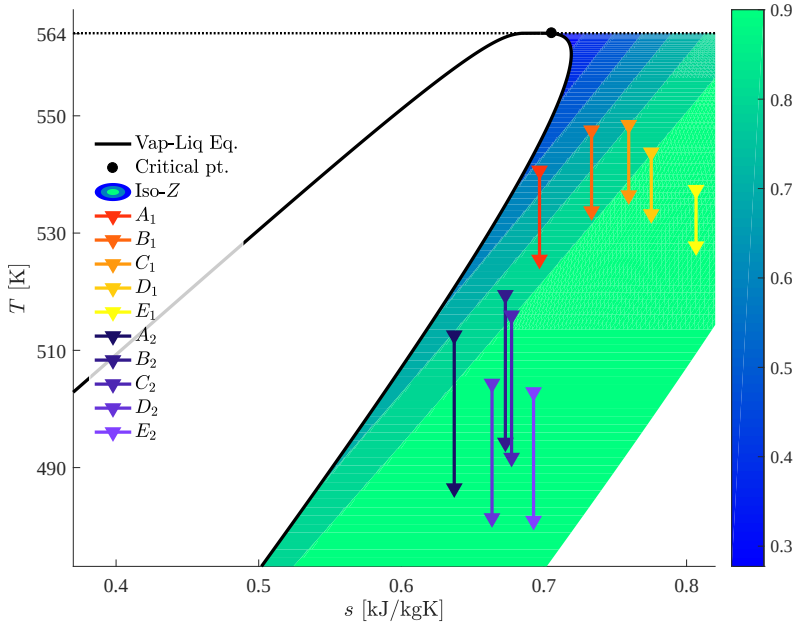

Figure 5.2: non-ideal expanding flows. T-s diagram reporting the liquid-vapor saturation curve (black bold line). On the diagram, the $A_1 - E_1$ and $A_2 - E_2$ expansions are plotted. Color scale points out the compressibility factor Z;

Exp	Measure	Static pressure at probes			
		52.4 [mm]	69.4 [mm]	86.4 [mm]	103.4 [mm]
A_1	P^s [Pa]	876727.9	799536.8	629696.5	388836.2
	U_{P^s} [Pa]	± 1518	± 1436	± 317.0	± 336.1
B_1	P^s [Pa]	808148.1	734519.9	573792.4	354030.8
	U_{P^s} [Pa]	± 1518	± 1438	± 316.9	± 335.9
C_1	P^s [Pa]	589375.1	532367.3	412412.8	250846.9
	U_{P^s} [Pa]	± 1518	± 1442	± 317.9	± 336.8
D_1	P^s [Pa]	308105.1	276217.0	210956.8	126508.1
	U_{P^s} [Pa]	± 1517	± 1460	± 320.6	± 339.9
E_1	P^s [Pa]	79203.6	70137.2	52714.8	31164.0
	U_{P^s} [Pa]	± 1516	± 1477	± 323.5	± 343.4

Table 5.3: non-ideal expanding flows, discharge 1. Experimental pressure measurements at station p1-p4 and related expanded uncertainty (2σ range);

Exp	Measure	Static pressure at x			
		69.4 [mm]	86.4 [mm]	103.4 [mm]	120.4 [mm]
A_2	P^s [Pa]	391484.3	301575.5	182008.1	147176
	U_{P^s} [Pa]	± 1666	± 349.5	± 370.2	± 423.7
B_2	P^s [Pa]	336648.7	258602.0	155236.7	125778.3
	U_{P^s} [Pa]	± 1664	± 349.6	± 370.1	± 423.7
C_2	P^s [Pa]	227492.1	173397.2	103368.4	84279.9
	U_{P^s} [Pa]	± 1665	± 349.9	± 370.8	± 423.7
D_2	P^s [Pa]	108430.3	81788.3	48551.8	38834.0
	U_{P^s} [Pa]	± 1673	± 352.2	± 373.2	± 423.6
E_2	P^s [Pa]	43900.4	32505.4	19194.5	14545.0
	U_{P^s} [Pa]	± 1690	± 354.4	± 375.2	± 423.5

Table 5.4: non-ideal expanding flows, discharge 2. Experimental pressure measurements at station p1-p4 and related expanded uncertainty (2σ range);

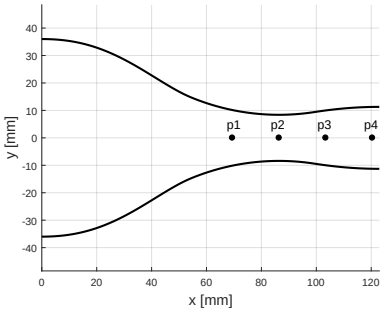

(a)

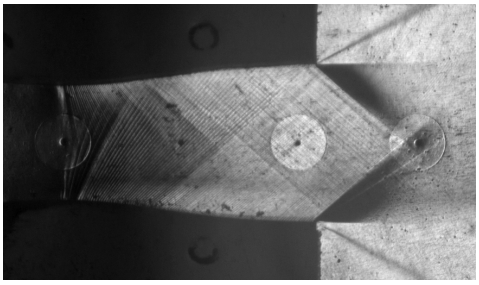

(b)

Figure 5.3: non-ideal expanding flows. (a) Geometrical sketch of the domain. Pressure taps (p1-p4) are highlighted by black dots; (b) Schlieren image focused on the discharging section of the nozzle;

The geometry of the nozzle is sketched in Fig. 5.3(a): the computational domain is limited to the converging and the diverging sections only. Therefore, the settling chamber and the discharge reservoir are not modeled in all the simulation presented hereinafter.

First, the A_2 experiment is reproduced numerically by means of steady simulations of inviscid flows, using diverse thermodynamic models. We are interested in comparing pressure predictions obtained using different thermodynamic models,

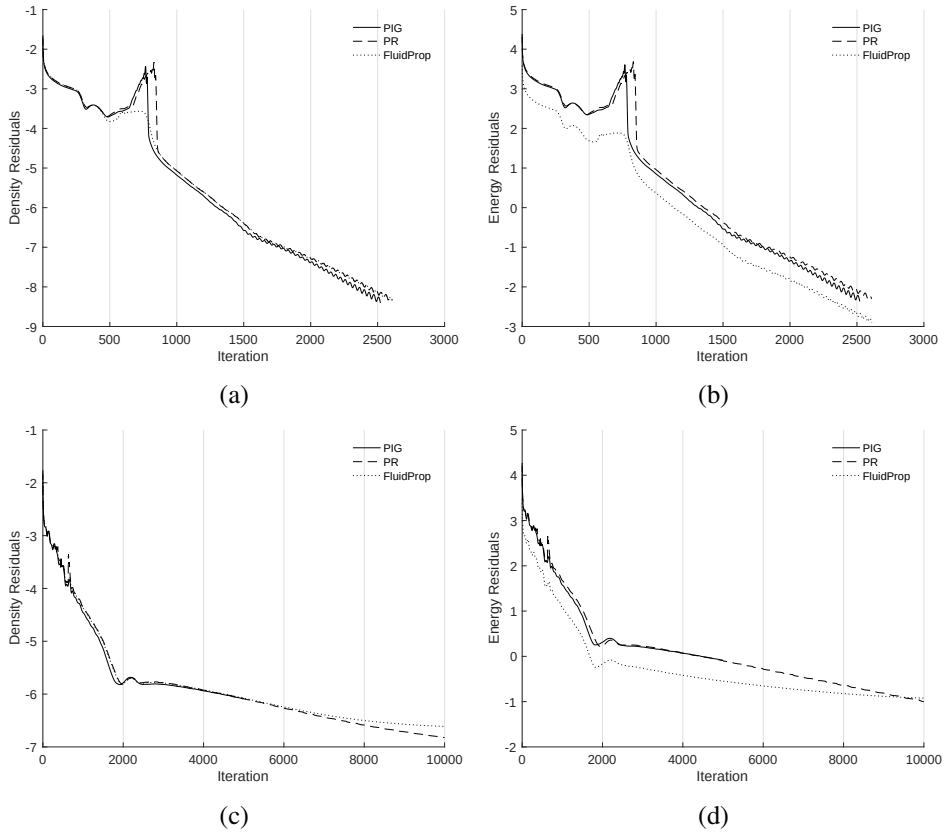

Figure 5.4: case A_2, simulation convergence histories using different fluid models. (a) Density residuals for the euler simulation; (b) Energy residuals for the euler simulation; (c) Density residuals for the RANS simulation; (d) Energy residuals for the RANS simulation;

namely the PIG, the polytropic PR and the multi-parameter EoS included in the FluidProp. This latter fluid model is characterized by a very complex form which yields a sharp increase of the computational cost. Therefore, we will rely on a quite coarse unstructured grid ($\approx$ 30k elements or $\approx$ 15k points), to lower the burden of computations. Nevertheless, the sensitivity analysis reported in Sec. 4.3.4 guarantees that a grid independent solution (considering pressure only) is largely achieved, at least for simulations carried out under the inviscid flow assumption. An implicit second-order accurate MUSCL scheme of Roe type was employed together with a flux limiting function (Venkatakrishnan flux limiter). The Green-Gauss formulae was used to reconstruct gradients at cell interfaces. For all the three cases, simulations were run until a residual reduction of a 6 orders of magnitude was obtained. Fig. 5.4(a-b) shows the history of density and energy residuals over solver iterations.

For the PIG case, 2521 iteration were unrolled in $\approx$ 416 secs before convergence

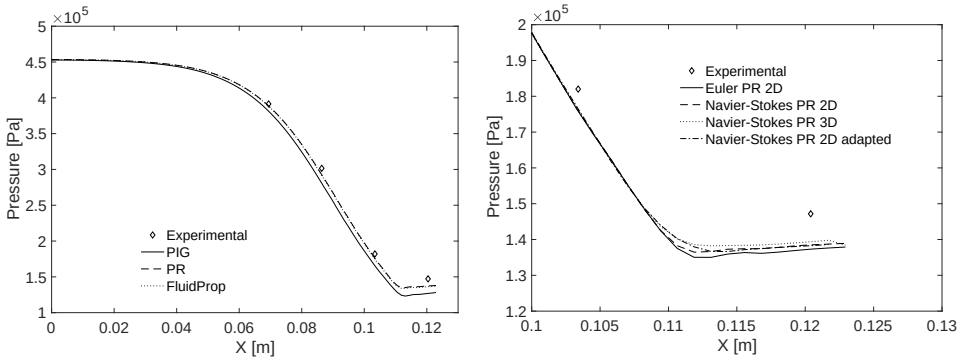

(a) (b)

Figure 5.5: case A_2. Comparison of pressure profiles along the nozzle axis for (a) different thermodynamic models; (b) viscous two- and three-dimensional simulations (enlargement at the nozzle exit);

was reached. 2609 iteration ($\approx$ 622 sec) were needed by the computation involving a PR gas and 2611 iteration ($\approx$ 36500 sec) for the one involving the state-of-the-art fluid model. Remarkably, the employment of the multi-parameter EoS results in a 5700% (w.r.t. the PR model) increase of the computational time. Simulations time are related to single core computation on a Intel® Xeon® x5650 (2.67 GHz) CPU.

Fig. 5.5(a) depicts the pressure profiles obtained using the diverse EoS. The PIG delivers a pressure distribution that qualitatively resembles the actual trend, but it loosely approaches the measured values (diamond marks in Fig. 5.5(a)). Results obtained using the more accurate EoS are found to be closer to experiments.

To assess the role of the boundary-layer, simulations based on the Reynolds-averaged Navier-Stokes (RANS) equations were also carried out. Two and three-dimensional CFD computations were carried out using single block structured meshes (Fig. 5.6 reports a snapshot of the three-dimensional mesh, 1M points). Viscous simulations take advantage of both the Spalart-Allmaras [27] and the Menter Shear Stress Transport [28] turbulence models. SU2 is not equipped with wall functions, therefore the boundary layer must be resolved up to the wall distance scale $y^+ = 1$ (corresponding to $\approx 1e^{-6}$ m). Note that our present knowledge of turbulence in the non-ideal regime is very limited, and so is the applicability of standard turbulence models. Nevertheless, no significant differences were found between the solution computed using different closures. Therefore, only results related to the Spalart-Allmaras model are provided in the following.

Fig. 5.4(c-d) shows the history of density and energy residuals over the RANS solver iterations. Turbulent computations converge slower than the inviscid ones. Fig. 5.5(b) reports an enlargement of the pressure profiles in the close proximity of the exhaust section, where larger differences are observed among numerical predic-

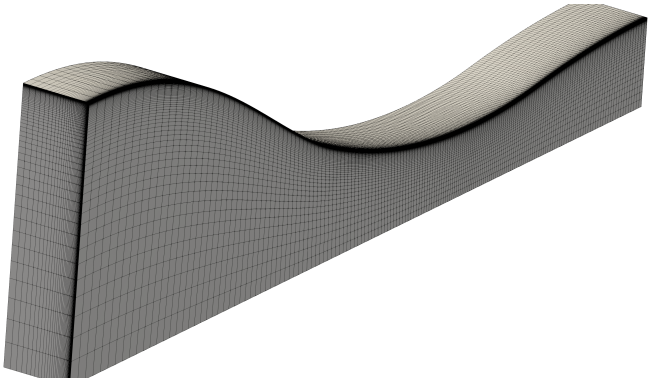

Figure 5.6: case A_2. Three-dimensional grid used to reproduce the flow in the TROVA nozzle. Double symmetry w.r.t. the nozzle center line is exploited to reduce the computational burden;

tions. The thin viscous boundary layer developing over solid walls does not impact the inner inviscid core significantly. Indeed, slight differences between viscous and inviscid simulations are found in correspondence with the terminal plateau only. This latter effect, possibly resulting from the reduction of the nozzle cross-sectional area due to the thickness of the boundary layer, is more relevant if a fully three-dimensional domain is considered. This was expected since the boundary layers now develops also along the nozzle side-walls. An adaptive mesh procedure was applied to two-dimensional viscous simulations, to enhance the quality of the grid within the boundary layer. Nevertheless, the grid adaptation did not yield any remarkable improvement.

To carry out the assessment, two sources of uncertainties, namely on the values of total pressure and total temperature, were taken into account. The total inflow conditions are reported in Tab. 5.1 and Tab. 5.2, together with the 2σ range for each variable. The DoE was created assuming a 5-th order polynomial that brought to the definition of a 6×6 test matrix. The spatial resolution was selected according to the grid sensitivity analysis reported in Sec. 4.3.4. The numerical grid employed hereinafter includes 104k elements (53k points). Realizations were obtained under the adiabatic an inviscid flow assumptions, the set up of numerical simulations resembles the one used to carry out the earlier comparisons. Fig. 5.7(a) reports the mean pressure trend along the nozzle centerline, for discharge conditions A_1, as predicted by metamodels built using polynomials of increasing order D (from $D = 1$ to $D = 3$). No remarkable differences are found between results returned by polynomials of different order. The accuracy of surrogate models was assessed using 25 additional sampling points in the stochastic space. For each point, the centerline static pressure trend was reconstructed using CFD simulations. Note that the additional sampling points were chosen such that they do not coincide with any of the points used for computing the metamodels coefficient. Pressure values predicted by CFD were com-

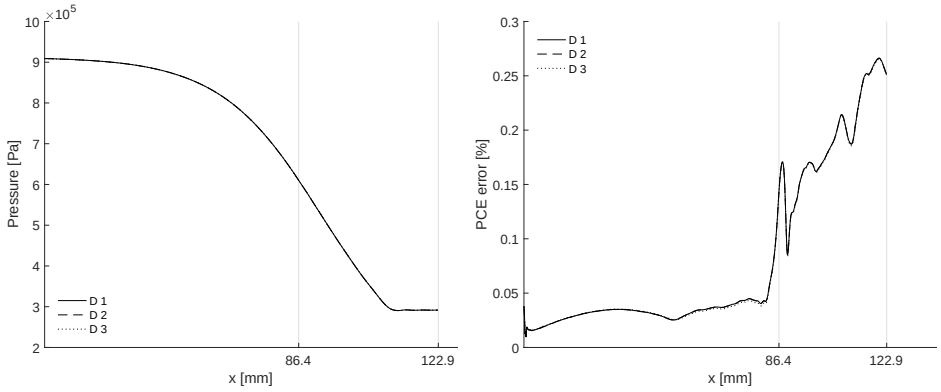

(a) (b)

Figure 5.7: non-ideal expanding flows, case A_1. (a) Comparison of the mean pressure trend along the nozzle centerline, for a diverse polynomial degree D; (b) RMSE w.r.t. additional sampling points from the stochastic space;

pared with the output obtained evaluating surrogate models at the same stochastic points. The percentage error, w.r.t. the average local value of pressure computed considering the 25 points, is plotted in Fig. 5.7(b), for the diverse polynomial orders. Again, no remarkable differences are found among surrogates built using polynomials of different order. Moreover, the error is limited and it can thus be neglected in the model validation process. Fig. 5.8(a) and (b) report the mean centerline pressure trend and the surrogate accuracy analysis for related to the A_2 discharge. The present results apply for all the remaining discharge conditions. Based on this analysis, surrogates relying on a polynomial order $D = 3$ are employed in the following.

Fig. 5.9(a-e) and Fig. 5.10(a-e) show the pressure mean trends, for the 10 considered experiments (A_1-E_1 and A_2-E_2), and the corresponding $\pm 2\sigma$ ranges resulting from the UQ analysis. On the same plots, experimental measurements and 2σ uncertainties are reported for comparison (diamond marks).

The numerical solution fairly matches experimental data in all cases: the mean pressure trend is indeed very close to the measured values. Discrepancies are generally found near the exhaust section, where the increase of the boundary layer thickness causes the flow to re-compress. Moreover, differences reduce as the flow regime drifts from highly non-ideal to ideal.

Schlieren images are exploited to directly measure the local value of the Mach number. For the particular flow configuration of interest here, only the schlieren image related to inflow conditions A_2 is available. Fig. 5.11(a) reports the experimental measurements and the related error bars, see [29]. In the same plot, the numerical mean solution and the $\pm 2\sigma$ interval, resulting from the UQ analysis of the Mach

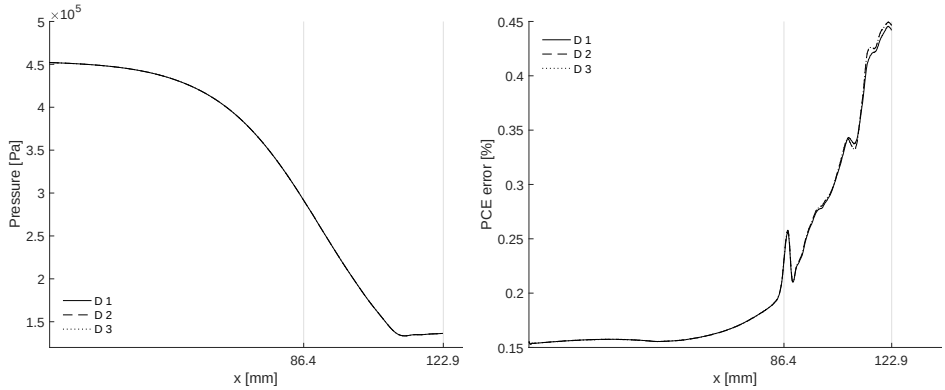

(a) (b)

Figure 5.8: non-ideal expanding flows, case A_2. (a) Comparison of the mean pressure trend along the nozzle centerline, for a diverse polynomial degree D; (b) RMSE w.r.t. additional sampling points from the stochastic space;

	p1	p2	p3
P [Pa]	287990	352710	221010
Δ [Pa]	$\pm$ 320	$\pm$ 340	$\pm$ 380

Table 5.5: non-ideal supersonic flows around a diamond-shaped airfoil. Experimental pressure measurements at station p1-p3 and related expanded uncertainty;

number, for test A_2, are reported. The mean solution is well included within the experimental error bars, pointing out the reliability of the predicted Mach number trend.

In Fig. 5.11(b), the Sobol indices for static pressure are reported, for the A_2 experiment. Fig. 5.11(b) reveals that the uncertainty related to the total pressure has a major influence on the variability of the static pressure. On the other hand, Sobol coefficients show that the uncertainty on temperature is associated to a considerable variability in the close proximity of the discharging section only.

5.4.2 Non-Ideal Supersonic Flows Around Diamond-Shaped Airfoils

The second test case aims at evaluating the solver capabilities when dealing with a flow-field affected by strong gradients, most notably, oblique shock waves. In particular, this test consists of a diamond-shaped airfoil plunged in to a supersonic uniform flow of MDM, at a neutral angle of attack. Pressure measurements at discrete points and the schlieren images of a wide portion of the test section are available from experiments (Tab. 5.5 reports pressure measurements at p1-p3). The domain and the

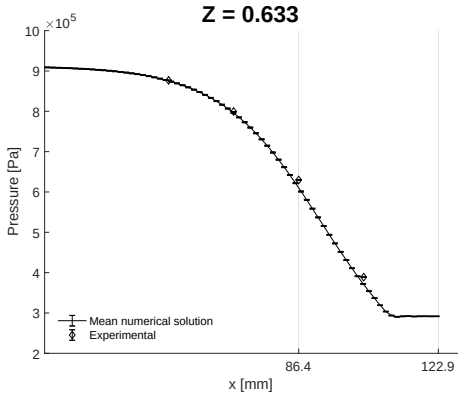

(a) A_1

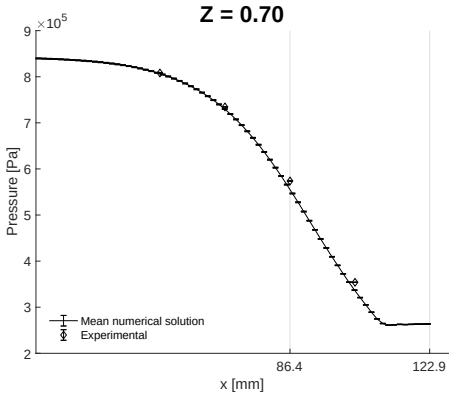

(b) B_1

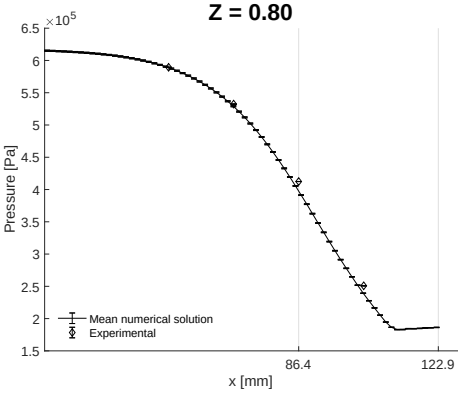

(c) C_1

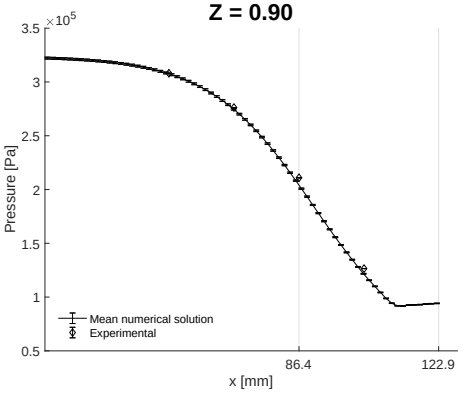

(d) D_1

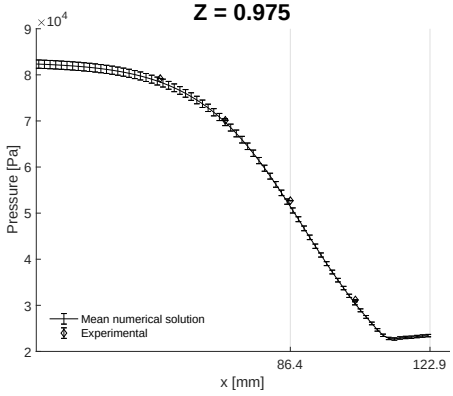

(e) E_1

Figure 5.9: non-ideal expanding flows, discharge 1. Mean pressure trends for the $A_1 - E_1$ experimental runs. Diamond marks correspond to experimental measurements;

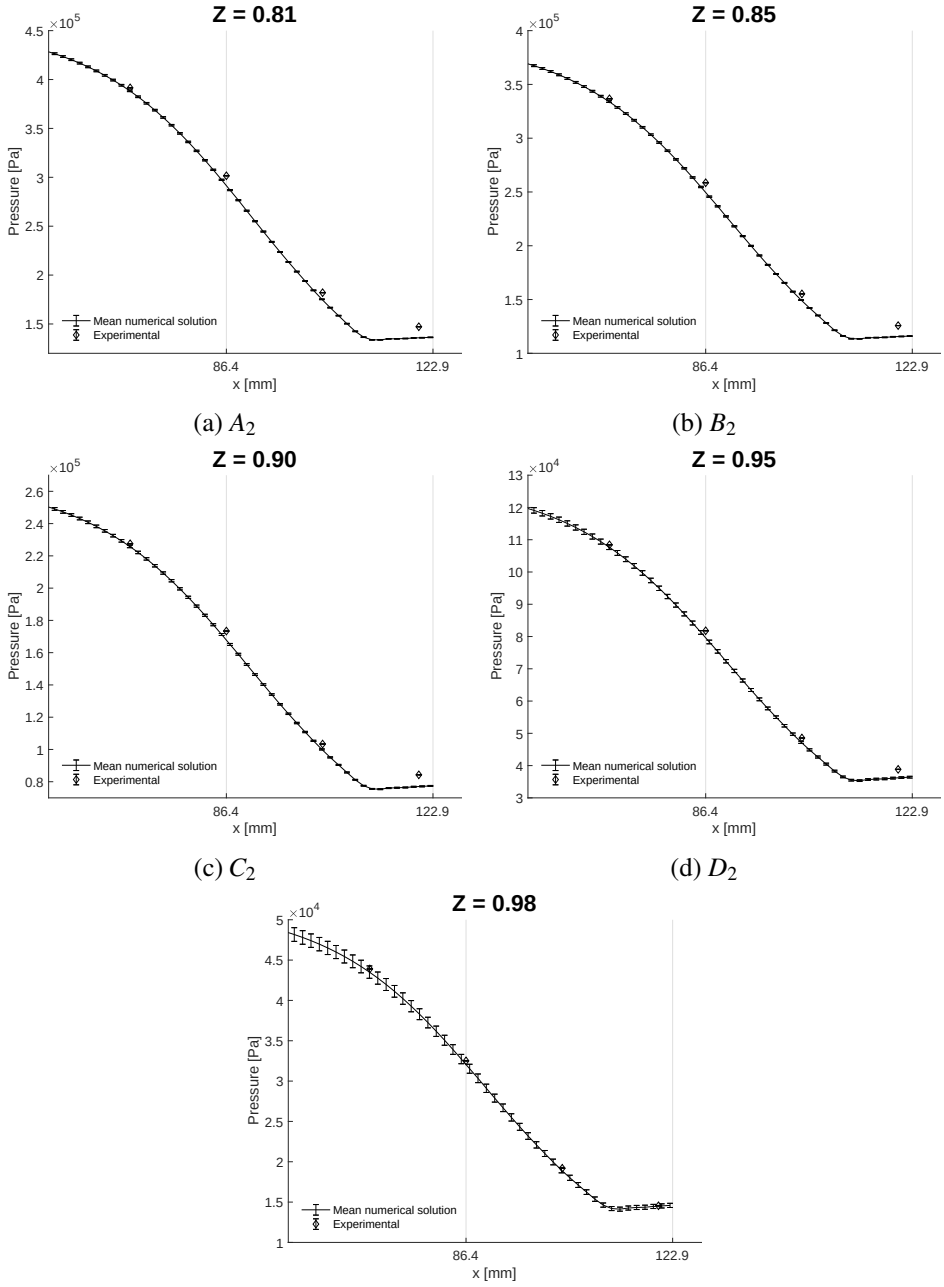

(a) A_2 (b) B_2

(c) C_2 (d) D_2

(e) E_2

Figure 5.10: non-ideal expanding flows, discharge 2. Mean pressure trends for the $A_2 - E_2$ experimental runs. Diamond marks correspond to experimental measurements;

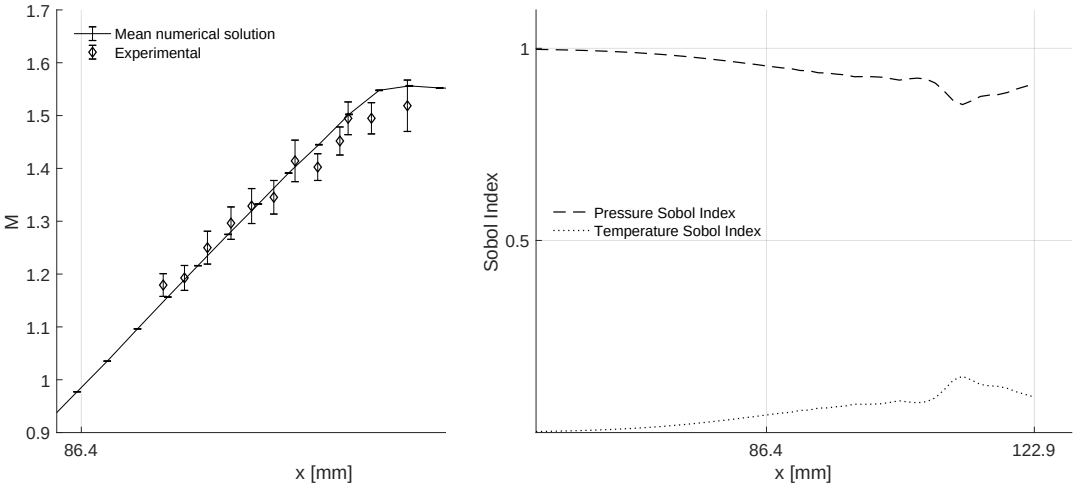

Figure 5.11: case A_2. (a) Experimental values and error bars relative to the Mach number measure are compared against the mean solution and the numerical error bars resulting from the UQ analysis; (b) Sobol indices for static pressure related to uncertainty on both the values of total pressure and total temperature at the inlet;

geometry of the airfoil are detailed in Fig. 5.12. The airfoil, symmetrical with respect to its chord ($c = 36$ [mm]), has a semiangle equal to 7.5° at the leading edge and 10° at the trailing edge, further details may be found in [30].

The nozzle is designed to produce a supersonic uniform flow at the exit section, where the airfoil is placed, see [11, 12]. Fluid conditions in the settling chamber are $P^{\mathrm{t}} = 870759.2$ Pa ($\pm$ 909.2 Pa) and $T^{\mathrm{t}} = 550.77$ K ($\pm$ 1.2 K). Ahead of the airfoil, the flow is approximately uniform at Mach 1.5 and $Z = 0.88$ (mildly non-ideal conditions). The schlieren image in Fig. 5.17(a), shows the terminal section of the nozzle divergent. Oblique shock waves are observed at the airfoil leading edge and they interact with the wind-tunnel walls. Static pressure is measured at selected locations (see Fig. 5.12): the first tap $p1$ is placed on the centerline, in the uniform flow region upstream of the nozzle exhaust section. The other pressure taps are arranged symmetrically on the upper and lower side of the airfoil. They are located in the uniform flow regions downstream of the shock wave ($p2$) and of the expansion fan ($p3$) originating on the airfoil.

This test case is useful to understand the physics of oblique shock-wall and shock-shock interactions in turbine cascades operating in off-design conditions. Since shocks are by far the most relevant feature of this investigation, a mesh adaptation procedure was heavily exploited, to improve the quality of the grid. Therefore, the mesh is automatically refined to capture steep gradients with an appropriate resolution. The adaptation algorithm evaluates density gradients across the domain and, according to an estimator function, it is capable to insert/remove nodes and to swap

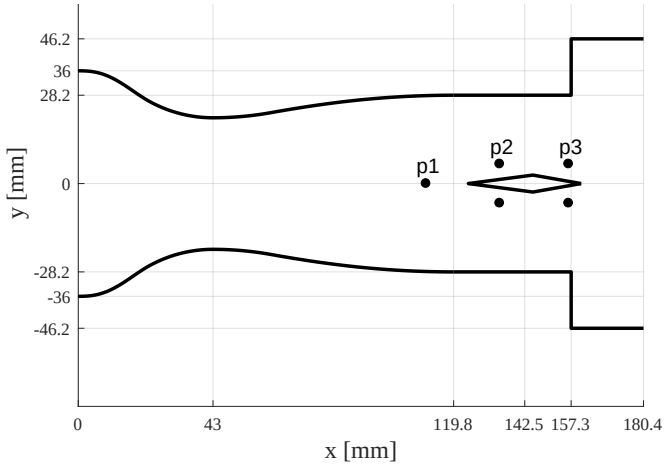

Figure 5.12: non-ideal supersonic flows around a diamond-shaped airfoil. Geometrical sketch of the numerical domain., pressure taps are highlighted by black dots (p1-p3);

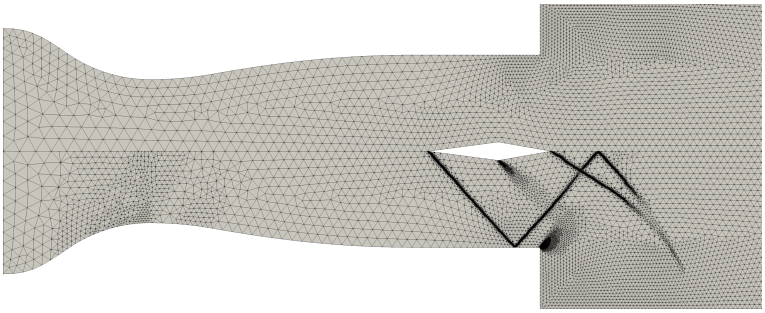

Figure 5.13: non-ideal supersonic flows around a diamond-shaped airfoil. The upper half depicts the baseline numerical grid while the lower side reports the grid resulting after six steps of mesh adaptation procedure (assuming an inviscid flow);

edges to improve the quality of the grid. Fig. 5.13 depicts the numerical domain: the upper side reports the baseline grid while the lower side represents the numerical grid obtained for Euler flows after six steps of adaptive refinement. The final grid ($\approx$ 48k elements, $\approx$ 24k points) includes almost 8 times the number of elements of the baseline mesh ($\approx$ 6k elements, $\approx$ 3k points).

The pressure field computed using the non-ideal CFD solver, for a viscous, fully turbulent flow, is reported in Fig. 5.14. The complex shock pattern is correctly reproduced as well as the shock-boundary layer interaction. For RANS simulations, the Spalart-Allmaras turbulence model was used [27]. 3 steps of adaptive refinement were unrolled. The baseline mesh includes 35k points while the final one includes 85k nodes. Fig. 5.15(a-d) report an enlargement of hybrid quad-triangular mesh (cen-

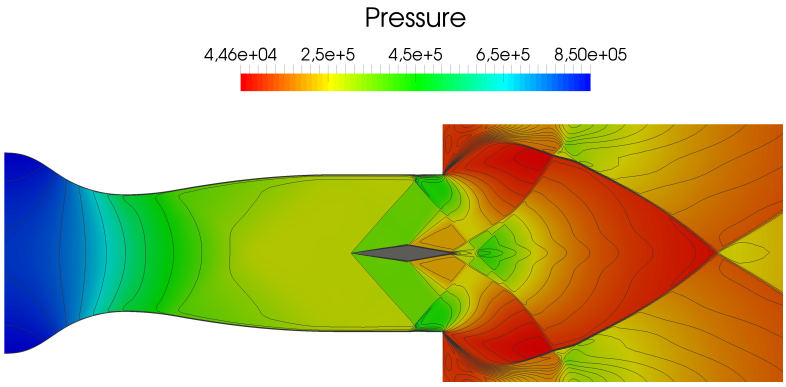

Figure 5.14: non-ideal supersonic flows around a diamond-shaped airfoil. Pressure field as computed by the NICFD solver. Mach Contours are also reported. The complex symmetrical flow around the airfoil features shocks, expansion fans, shock-shock and shock-boundary layer interaction;

tered on the airfoil) as resulting after each adaptation step. The algorithm correctly increases the spatial resolution in correspondence with steep gradients (shock waves and/or rarefaction fans. Further than the Euler flow case, the grid is also nicely refined to capture the complex structure arising from the interaction of the leading shock with the boundary layer over the nozzle profile.

Fig. 5.16(a) reports the pressure profiles, computed for different levels of grid resolution, obtained from inviscid simulations of MDM vapor modeled using the polytropic PR EoS. A second order implicit HLLC (Harten-Lax-van Leer-Contact) scheme [31] was employed to reconstruct the spatial convective fluxes. A flux limiting function (Venkatakrishnan) was used to damp spurious oscillation while the Green-Gauss method was used to reconstruct the spatial gradients. Trends were extracted along a line parallel to the nozzle axis, at a distance of 6.25 mm from the centerline, which corresponds to a straight line through pressure taps $p2$ and $p3$. It has to be remarked that, differently from $p2$ and $p3$, the value of pressure $p1$ is measured along the nozzle axis but it is actually compared against its numerical value at a distance of $y = 6.25$ mm: the flow before the diamond is uniform thus the pressure can be considered almost constant in a direction normal to the nozzle center line. Turbulent viscous simulations using the Spalart-Allmaras turbulent model [27] were also carried out. Fig. 5.16(b) reports a comparison of the pressure trends obtained from inviscid and viscous simulations using both the PR EoS and FluidProp. Experimental measures are reported on the same plot for comparison (diamond marks). The compressibility factor Z is approximately equal to 0.88 ahead of the diamond. For this reason, the pressure trend resulting from a flow modeled with the PIG EoS departs significantly from experimental measurements. On the other hand, numerical results that take advantage of the polytropic PR EoS provide better predictions.

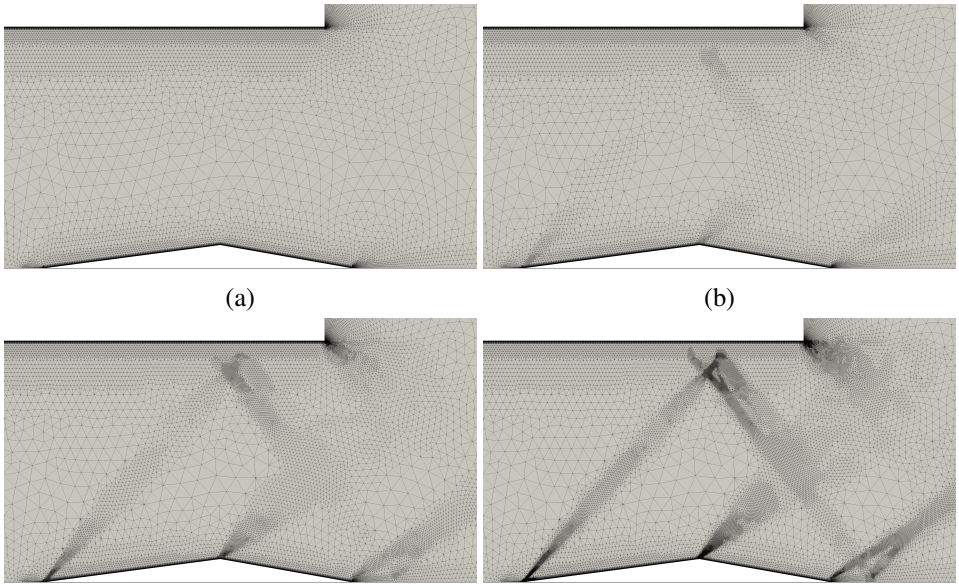

(a) (b)

(c) (d)

Figure 5.15: non-ideal supersonic flows around a diamond-shaped airfoil. (a) Baseline viscous grid; (b) Viscous grid after the first adaptation step; (c) Viscous grid after the second adaptation step; (d) Viscous grid after the third adaptation step;

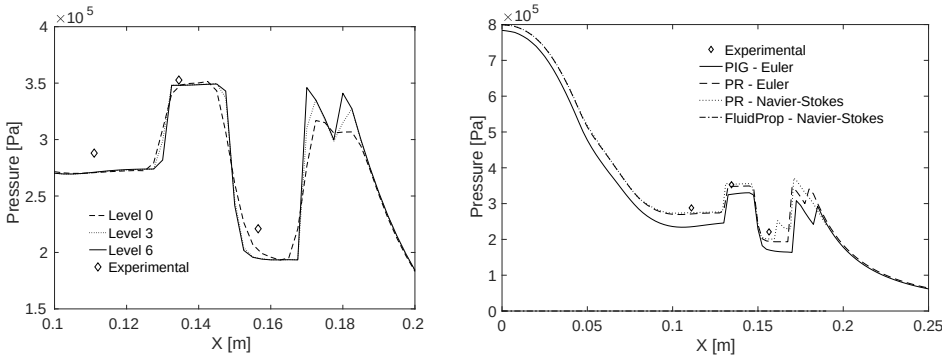

(a) (b)

Figure 5.16: non-ideal supersonic flows around a diamond-shaped airfoil. (a) Pressure trends from inviscid simulations for different adaptation steps are compared against the experimental result. Picture shows an enlargement focused on the region close to the diamond-shaped airfoil; (b) Pressure trends from inviscid and viscous simulation using the PR EoS are compared against the experimental measure. Pressure trend computed for an inviscid ideal flow is also compared;

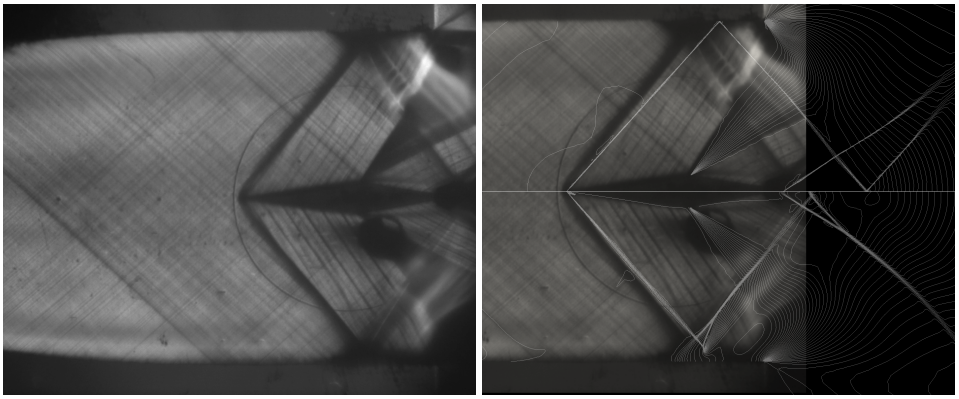

(a) (b)

Figure 5.17: non-ideal supersonic flows around a diamond-shaped airfoil. (a) Experimental schlieren image of the supersonic flow field around the diamond-shaped airfoil. (b) Density contours from inviscid (upper side) and from viscous (lower side) simulations, using the PR EoS, are superimposed to the shlieren image;

In Fig. 5.17(b), density contours are plotted over the corresponding schlieren image. Note that, nominally, the airfoil is at a neutral angle of attack but, due to an unavoidably positioning error in the experimental set up, the resulting shock pattern in the schlieren image is slightly asymmetric.

In particular, Fig. 5.17(b) reports density contours of both inviscid and viscous simulation using the polytropic PR EoS, respectively on the upper and on the lower side. Viscous effects are of utmost importance, as expected, in the close proximity of channel walls, where the boundary layer develops. Indeed, the schlieren image reveals that the structure arising from the interaction of the leading shock-wave with the boundary layer occurs. Obviously, inviscid simulations are not able to capture this feature: though the angle of the leading wave is predicted fairly well, the shock pattern downstream does not match the experimental one (upper side of Fig. 5.17(b)). On the other hand, density contours from Navier-Stokes simulations, reported on the lower side of Fig. 5.17(b), clearly reproduce the shock-boundary layer interaction phenomenon and the shock pattern revealed in the schlieren frame is almost perfectly matched.

To carry out the UQ Forward Propagation, RANS simulations take advantage of the mesh adaptation procedure as well. Namely, three steps of adaptive refinement were unrolled before accepting the solution of each UQ realization. The Spalart-Allmaras turbulent model [27] was used to close the turbulent equations. The very same numerical set up described earlier in the section was maintained. The analysis considered the uncertainties over the total pressure and total temperature and the DoE resulted in a 36 test cases matrix. Thermodynamics was described using the reference EoS included in the FluidProp library.

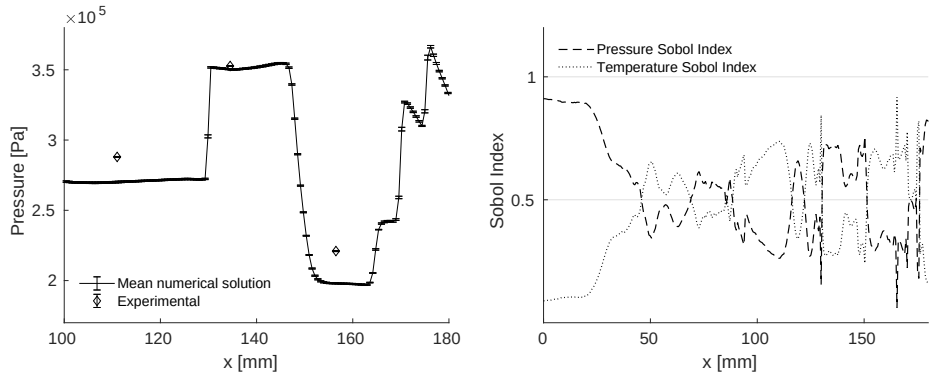

(a) (b)

Figure 5.18: non-ideal supersonic flows around a diamond-shaped airfoil. (a) Mean pressure trend and numerical error bars as resulting from the UQ analysis. Experimental values and the related uncertainties are also reported; (b) Sobol indices for static pressure related to uncertainty on both total pressure and total temperature at the inlet;

As detailed previously, numerical pressure trends were extracted along a direction parallel to the nozzle axis, at a distance of 6.25 mm from the centerline. Fig. 5.18(a) reports the mean pressure trend, resulting from the UQ analysis, and the experimental measures at $p1$, $p2$ and $p3$ (diamond marks).

The analysis of Sobol indices, reported in Fig. 5.18(b), reveals that the uncertainty related to the total pressure has a relatively major role in the nozzle converging section. Past the throat ($x = 43$ mm), the magnitude of the contributions from the two uncertainty sources is instead comparable. Fig. 5.19(a) reports the comparison of the Mach number (as measured from schlieren images) against predictions: results further confirm the predictiveness of the solver. Fig. 5.19(b) reports the 2σ ranges related to the value of temperature over the nozzle centerline. Temperature turns out to be a more sensitive to uncertainties than pressure. The solver is able to reproduce the correct flow-field as the mean pressure trend is very close to the measured values. A limited variability for Mach, pressure ($< 0.01\%$) and temperature ($< 0.2\%$), confirm a very robust and predictive numerical solution.

The very same test section is now used to generate a different experimental data set. Differently than the previous case, in the present configuration the airfoil is placed in a reversed position, so that the semi-angle at the leading edge is now equal to 10° (while at the trailing edge it is 7.5°). The compressibility factor, as resulting from simulations, points out a mildly non-ideal flow regime ($Z \sim 0.93$) ahead of the airfoil. Fluid inflow conditions correspond to $P^t = 619100$ Pa (± 920 Pa) and $T^t = 534.55$ K (± 1.2 K). Uncertainties on the values of total pressure and total temperature at the inlet are again taken into account. For this test case, a further source of uncertainty i.e., the angular position of the airfoil, is considered. In practice, the

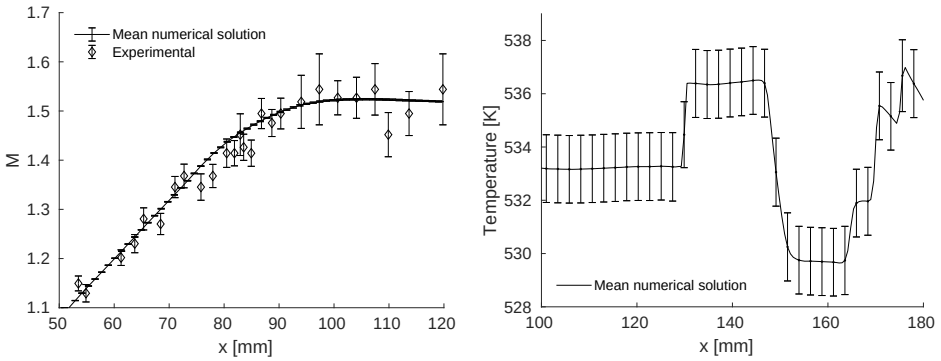

(a) (b)

Figure 5.19: non-ideal supersonic flows around a diamond-shaped airfoil. (a) Experimental values and error bars relative to the Mach number measure are compared against the mean solution and the numerical error bars resulting from the UQ analysis; (b) Mean static temperature trend and numerical error bars resulting from the UQ analysis;

profile is manually set to a neutral angle of incidence by means of a visual reference system. The uncertainty related to the manual orientation of the airfoil is assumed to be uniformly distributed and limited within a range of $\pm 0.5^{\circ}$. Following the same approach described in Sec. 5.3, a 4th order polynomial led to a DoE made up by 125 test cases.

Once again, a second order implicit HLLC (Harten-Lax-van Leer-Contact) scheme [31] was employed to reconstruct the spatial convective fluxes with a flux limiting function (Venkatakrishnan). Green-Gauss method was used to reconstruct the spatial gradients. Turbulent viscous simulations took advantage of the Spalart-Allmaras turbulent model [27]. Again, a grid adaptation algorithm based on the etimation of density gradient is employed. Moreover, as the uncertainty on the angle of attack is considered the flow field can no longer be assumed symmetrical. Therefore, the whole domain needs to be simulated. The solution is qualitatively similar to the one presented in Sec. 5.4.2. The angle of the shocks is different (larger) than the one found in Case B. This is of course due to the different semi-angle characterizing the leading edge, which is now steeper, and to a different state of the fluid. For this test case, the typical structure arising from the shock-boundary layer interaction is much more relevant. An enlargement of the region of the domain characterized by this phenomenon is reported in Fig. 5.20, showing the pressure field and the Mach number contours. Past the shock, the thickness of the boundary layer increases considerably resulting in a region dominated by viscous effects. The UQ analysis shows that the predicted mean pressure trend (Fig. 5.21(a)) is robust with respect of the considered sources of uncertainty. In the region past the leading shock, the numerical error bars have a larger amplitude due to the fact that the slope of the wave strongly

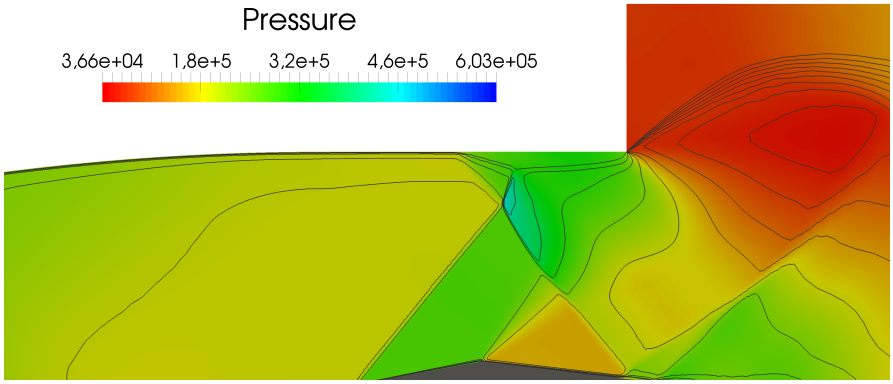

Figure 5.20: non-ideal supersonic flows around a diamond-shaped airfoil (reversed). Pressure field and Mach contours in the close proximity of the structure arising from the shock-boundary layer interaction. This phenomenon is much more relevant than in case B due to different flow conditions.

depends on the angle of the ramp i.e., the angle of attack of the diamond. Indeed, Sobol indices (Fig. 5.21(b)) reveal that the uncertainty affecting the total pressure plays a key role throughout the whole length of the nozzle but it is less relevant as the flows approaches the airfoil. On the other hand, the uncertainty on total temperature shows the reversed behavior. As anticipated, the uncertainty related to the angle of attack is instead relevant, and it actually dominates, the region downstream the airfoil. Pressure measurements are available at station $p1$ ($P = 197870$ Pa ± 300 Pa) and $p2$ ($P = 274150$ Pa ± 350 Pa) only, see Fig. 5.12, while the Mach number is again available from schlieren images. Mach measurements obtained from schlieren frames are reported in Fig. 5.22(a). Once again, the mean solution is well included within the experimental error bars thus confirming the reliability of predictions from the solver. With reference to the sensitivity of the predicted temperature trend Fig. 5.22(b), the solver is proved to be robust and predictive.

5.4.3 Non-Ideal Supersonic over a Backward Facing Step

The last test case consists of a supersonic flow over a backward facing step. The step causes the formation of an oblique shock which is observed experimentally at the flow reattachment point, downstream the step. This geometry is representative of the trailing edge of turbine blades as the resulting flow configuration resembles the formation of the typical fish-tail shock waves. A converging-diverging nozzle is placed in the test section of the TROVA test rig, to produce a supersonic speed. The profile was wrought and a backward facing step of height $h = 0.1$ [mm] was obtained at the

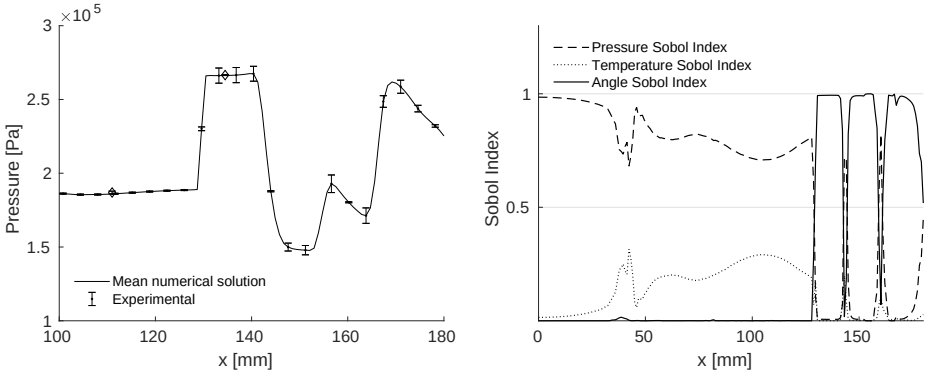

(a) (b)

Figure 5.21: non-ideal supersonic flows around a diamond-shaped airfoil (reversed). (a) mean pressure trend and numerical error bars as resulting from the UQ analysis. Experimental values and the related uncertainties are also reported; (b) Sobol indices for static pressure related to uncertainty on both total pressure and total temperature, at the inlet, and on the airfoil angle of attack;

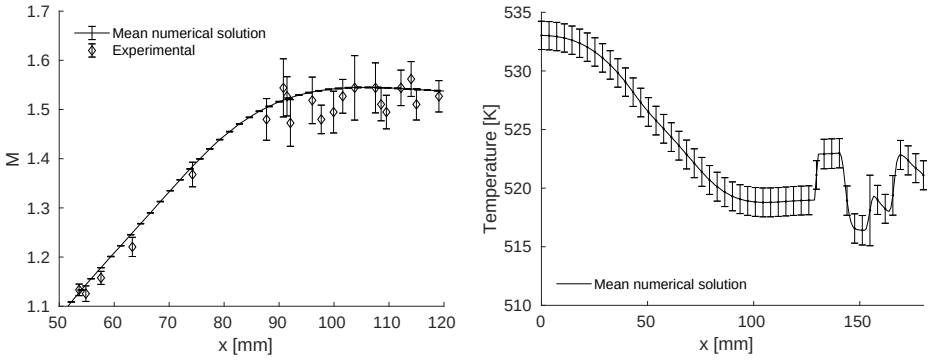

(a) (b)

Figure 5.22: non-ideal supersonic flows around a diamond-shaped airfoil (reversed). (a) Experimental values and error bars relative to the Mach number measure are compared against the mean solution and the numerical error bars resulting from the UQ analysis; (b) Mean static temperature trend and numerical error bars resulting from the UQ analysis;

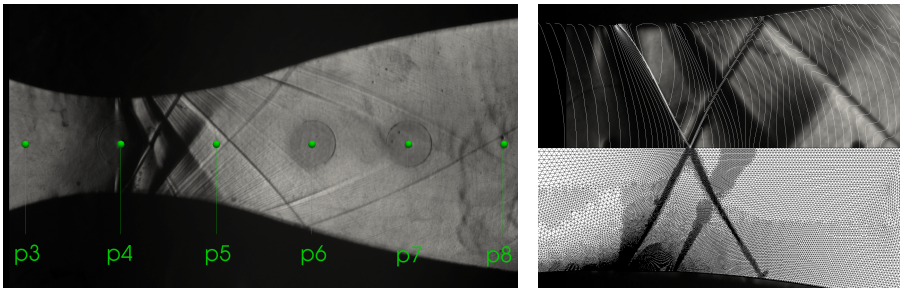

(a) (b)

Figure 5.23: case D. (a) schlieren image of the flow-field within a nozzle with a backward facing step at the throat. Green dots indicate the position of pressure taps; (b) An enlargement of the nozzle throat section. On the upper side density contour from viscous simulation using the PR EoS are superimposed to the schlieren image. On the lower side, the numerical grid after two steps of adaptation procedure is reported;

throat section. The throat is 8.4 [mm] wide, see [15, 32, 33]. Fig. 5.23(a) reports a schlieren snapshot of the test section and the position of each pressure tap. For this test case, the UQ Forward Propagation was not carried out and only an experimental assessment is provided. A RANS simulation was carried out using a second order implicit HLLC (Harten-Lax-van Leer-Contact) scheme [31], to reconstruct the spatial convective fluxes. The Venkatakrishnan flux limiting function was used while the Green-Gauss method was employed to reconstruct the spatial gradients. Test conditions in the settling chamber corresponds to $P^{\mathrm{t}} = 457746.8$ Pa and $T^{\mathrm{t}} = 520.1$ K. There, the value of the compressibility factor Z is equal to 0.82 and it increases monotonically (up to 0.98 at pressure tap $p8$). In the proximity of the step, the flow Mach number is around 1.1 and the compressibility factor $Z \sim 0.89$. The presence of a backward facing step results in a complex (symmetrical) system of shock-waves that are reflected against the walls further downstream. The mesh adaptation procedure was found to be key to improve the resolution of the computed flow-field and, at the same time, to limit the size of the computational grid. Three refinement steps were unrolled, bringing the grid point number from 42k to 108k. Once again, grid refinement is based on the evaluation of density gradients within the domain. Density contours are reported in Fig. 5.23(b): picture shows an enlargement of the nozzle throat region and density contours are superimposed on the experimental schlieren image. Fig. 5.23(b) reports also, on the lower side, the computational grid resulting after 2 steps of adaptive refinement. The resolution of the grid is correctly increased in the close proximity of shock-waves and within rarefaction fans.

Fig. 5.24(a) reports pressure trends over the centerline, as resulting from a deterministic RANS simulation at nominal operating conditions. Three step of grid adaptation were unrolled. In Fig. 5.24(a), experimental measurements are compared against pressure trends computed using the PIG, the polytropic PR EoS and Fluid-

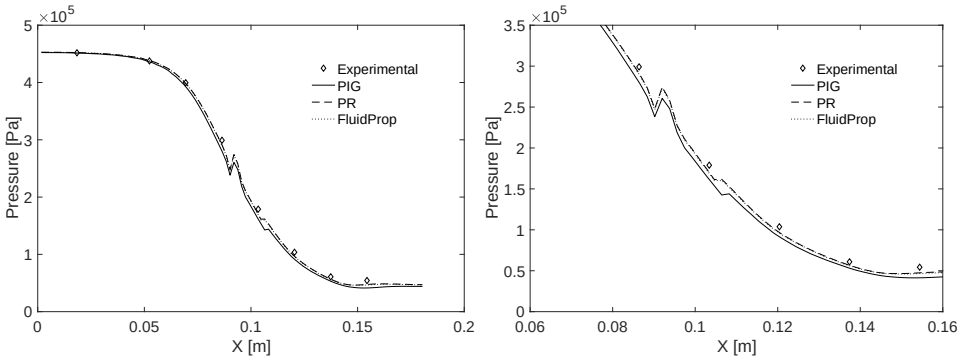

Figure 5.24: case D. (a) Comparison of pressure trends along the axis of the nozzle computed from viscous simulations for backward facing step test case; (b) Enlargement of the pressure trends along the axis of the nozzle computed from viscous simulations for backward facing step test case;

Prop. Fig. 5.24(b) depicts an enlargement of the pressure trend corresponding to the diverging section of the nozzle. With reference to the PIG, both the PR and the state-of-the-art EoS from FluidProp are found to return predictions that better approach the experimental measurements, as expected.

5.5 Conclusions

For the first time, the capabilities of a non-ideal CFD model were assessed against experimental results related to flows of fluid in a non-ideal regime. Experimental data used for comparison were collected using the TROVA facility at Politecnico di Milano.

The non-ideal model included in the SU2 open-source suite was assessed for a set of exemplary flow configurations of relevant interest for practical applications. Such set includes the supersonic flow in a planar converging-diverging nozzle, representative of ORC supersonic stators, a supersonic flow around a diamond-shaped airfoil, which was selected to investigate the physics of oblique shock-wall and shock-shock interactions in turbine cascades and the supersonic flow over a backward facing step. In some cases, the considered flows feature shock waves and rarefaction fans of strong intensity. Therefore, a grid adaptation strategy was key to obtain a satisfying level of resolution using a reasonable amount of grid points. Numerical simulations were carried out using the Reynolds-Averaged compressible Navier-Stokes equations for non-ideal compressible, fully turbulent, flows. A non-intrusive polynomial chaos-based technique was used to forward propagate the physical uncertainties, associated

to the inlet conditions, through the numerical solver.

Comparison against experimental data reveals that all the considered non-ideal flows are fairly well simulated by the solver. The variability of the numerical solution is limited to very small values, pointing out the robustness and the predictive character of the numerical tool. The non-ideal CFD model from the SU2 suite was therefore assessed against experimental results and the reliability of the numerical implementation and the predictiveness of the solver are thus confirmed.

Nevertheless, results presented in this chapter reveal a mismatch between experimental and numerical predictions from SU2. Apparently, the mismatch increases as the regime of the flow departs more and more from the ideal behavior. Since this trend seems to be strictly related to the thermodynamics of the flow, it could be an indication that the CFD model of the TROVA test-rig, which is comprehensive of the thermodynamic fluid model, could be improved. In particular, since experimental measurements are now available, a potential further research effort could consist in calibrating the material-dependent parameters appearing in the EoS used to model the thermodynamic behavior of NICFD flows.

References

[1] F. Palacios, M. R. Colonno, A. C. Aranake, A. Campos, S. R. Copeland, T. D. Economon, A. K. Lonkar, T. W. Lukaczyk, T. W. R. Taylor, and J. J. Alonso. "Stanford University Unstructured (SU^2): An open-source integrated computational environment for multi-physics simulation and design". In: *AIAA Paper 2013-0287* 51st AIAA Aerospace Sciences Meeting and Exhibit (Jan. 2013).

[2] T. D. Economon, D. Mudigere, G. Bansal, A. Heinecke, F. Palacios, J. Park, M. Smelyanskiy, J. J. Alonso, and P. Dubey. "Performance optimizations for scalable implicit RANS calculations with SU2". In: *Computers & Fluids* 129 (2016), pp. 146–158. ISSN: 0045-7930. DOI: http://dx.doi.org/10.1016/j.compfluid.2016.02.003. URL: http://www.sciencedirect.com/science/article/pii/S0045793016300214.

[3] F. Palacios, T. D. Economon, A. Aranake, R. S. Copeland, A. Lonkar, T. Lukaczyk, D. E. Manosalvas, R. K. Naik, S. Padron, B. Tracey, A. Variyar, and J. J. Alonso. "Stanford university unstructured (SU2): Analysis and design technology for turbulent flows". In: *AIAA Paper 2014-0243* 52nd Aerospace Sciences Meeting (2014).

[4] T. D. Economon, F. Palacios, S. R. Copeland, T. W. Lukaczyk, and J. J. Alonso. "SU2: An Open-Source Suite for Multiphysics Simulation and Design". In: *AIAA Journal* 54.3 (2016/09/08 2015), pp. 828–846. DOI: 10.2514/1.J053813. URL: http://dx.doi.org/10.2514/1.J053813.

[5] R. Sanchez, H. Kline, D. Thomas, A. Variyar, M. Righi, D. T. Economon, J. J. Alonso, R. Palacios, G. Dimitriadis, and V. Terrapon. "Assessment of the fluid-structure interaction capabilities for aeronautical applications of the open-source solver SU2". In: *ECCOMAS, VII European Congress on Computational Methods in Applied Sciences and Engineering, Crete Island, Greece* (2016).

[6] S. Vitale, G. Gori, M. Pini, A. Guardone, T. D. Economon, F. Palacios, J. J. Alonso, and P. Colonna. "Extension of the SU2 open source CFD code to the simulation of turbulent flows of fluids modelled with complex thermophysical laws". In: *22^{nd} AIAA Computational Fluid Dynamics Conference*. AIAA Paper 2760. 2015.

[7] G. Gori, A. Guardone, S. Vitale, A. Head, M. Pini, and P. Colonna. "Non-Ideal Compressible-Fluid Dynamics Simulation with SU2: Numerical Assessment of Nozzle and Blade Flows for Organic Rankine Cycle Applications". In: *3rd International Seminar on ORC Power Systems*. Brussels, Belgium, Oct. 2015.

[8] M. Pini, S. Vitale, P. Colonna, G. Gori, A. Guardone, T. Economon, J. Alonso, and F. Palacios. "SU2: the Open-Source Software for Non-ideal Compressible Flows". In: vol. 821. 1. 2017, p. 012013.

[9] G. Gori, M. Zocca, G. Cammi, A. Spinelli, and A. Guardone. "Experimental assessment of the open-source SU2 CFD suite for ORC applications". In: *Energy Procedia* 129.Supplement C (2017), pp. 256–263.

[10] C. J. Roy and W. L. Oberkampf. "A comprehensive framework for verification, validation, and uncertainty quantification in scientific computing". In: *Computer Methods in Applied Mechanics and Engineering* 200.25 (2011), pp. 2131–2144. ISSN: 0045-7825. DOI: https://doi.org/10.1016/j.cma.2011.03.016. URL: http://www.sciencedirect.com/science/article/pii/S0045782511001290.

[11] A. Spinelli, M. Pini, V. Dossena, P. Gaetani, and F. Casella. "Design, Simulation, and Construction of a Test Rig for Organic Vapours". In: *ASME J. Eng. Gas Turb. Power* 135 (2013), p. 042303.

[12] A. Guardone, A. Spinelli, and V. Dossena. “Influence of Molecular Complexity on Nozzle Design for an Organic Vapor Wind Tunnel”. In: *ASME J. Eng. Gas Turb. Power* 135 (2013), p. 042307.

[13] M. Pini, A. Spinelli, V. Dossena, P. Gaetani, and F. Casella. “Dynamic Simulation of a Test Rig for Organic Vapours”. In: *Proceedings of 5th Conference on Energy Sustainability, ASME EsFuelCell2011, Washington, Washington DC, USA*. Aug. 2011.

[14] A. Spinelli, F. Cozzi, M. Zocca, P. Gaetani, V. Dossena, and A. Guardone. “Experimental Investigation of a Non-Ideal Expansion Flow of Siloxane Vapor MDM”. In: *Proceedings of the ASME 2016 Turbo Expo, Soul*. GT2016-57357. 2016.

[15] A. Spinelli, A. Guardone, F. Cozzi, M. Carmine, R. Cheli, M. Zocca, P. Gaetani, and V. Dossena. “Experimental Observation of Non-Ideal Nozzle Flow of Siloxane Vapor MDM”. In: *3rd International Seminar on ORC Power Systems, Brussels, Belgium, 12-14 October*. 2015.

[16] R. Lo and W. Tsai. “Gray-scale hough trasform for thick line detection in grey-scale images”. In: *Pattern Recognition* 28 (1995), pp. 647–661.

[17] A. Spinelli, G. Cammi, S. Gallarini, M. Zocca, F. Cozzi, P. Gaetani, V. Dossena, and A. Guardone. “Experimental evidence of non-ideal compressible effects in expanding flow of a high molecular complexity vapour”. In: *Experiments in Fluids* 59.8 (July 2018), p. 126.

[18] T. Crestaux, O. Le Matre, and J.-M. Martinez. “Polynomial chaos expansion for sensitivity analysis”. In: *Reliability Engineering & System Safety* 94.7 (2009), pp. 1161–1172.

[19] P. Cinnella, P. Congedo, and L. Parussini. “Quantification of thermodynamic uncertainties in real gas flows”. In: *International Journal of Engineering Systems Modelling and Simulation* 2.1-2 (2010), pp. 12–24.

[20] P. Cinnella, P. Congedo, V. Pediroda, and L. Parussini. “Sensitivity analysis of dense gas flow simulations to thermodynamic uncertainties”. In: *Physics of Fluids* 23 (2011).

[21] X. Merle and P. Cinnella. “Bayesian quantification of thermodynamic uncertainties in dense gas flows”. In: *Reliability Engineering & System Safety* 134.Supplement C (2015), pp. 305–323. ISSN: 0951-8320. DOI: https://doi.org/10.1016/j.ress.2014.08.006. URL: http://www.sciencedirect.com/science/article/pii/S0951832014001999.

[22] P. Congedo, C. Corre, and J.-M. Martinez. “Shape optimization of an airfoil in a BZT flow with multiple-source uncertainties”. In: *Computer Methods in Applied Mechanics and Engineering* 200.1-4 (Aug. 2011), pp. 216–232. ISSN: 00457825. DOI: 10.1016/j.cma.2010.08.006. URL: http://linkinghub.elsevier.com/retrieve/pii/S0045782510002392.

[23] P. Congedo, G. Geraci, R. Abgrall, V. Pediroda, and L. Parussini. “TSI metamodels-based multiobjective robust optimization”. In: *Engineering Computations (Swansea, Wales)* 30.8 (2013), pp. 1032–1053.

[24] G. Geraci, P. Congedo, R. Abgrall, and G. Iaccarino. “High-order statistics in global sensitivity analysis: Decomposition and model reduction”. In: *Computer Methods in Applied Mechanics and Engineering* 301 (2016), pp. 80–115. ISSN: 0045-7825. DOI: http://dx.doi.org/10.1016/j.cma.2015.12.022. URL: http://www.sciencedirect.com/science/article/pii/S0045782515004284.

[25] M. Thol, F. H. Dubberke, E. Baumhögger, J. Vrabec, and R. Span. “Speed of Sound Measurements and Fundamental Equations of State for Octamethyltrisiloxane and Decamethyltetrasiloxane”. In: *Journal of Chemical & Engineering Data* 62.9 (2017), pp. 2633–2648.

[26] D. Dussin, M. Fossati, A. Guardone, and L. Vigevano. “Hybrid grid generation for two-dimensional high-Reynolds flows”. In: *Computers & Fluids* 38.10 (2009), pp. 1863–1875.

[27] P. Spalart and S. Allmaras. “A one-equation turbulence model for aerodynamic flows”. In: *AIAA Paper 1992-0439* (1992).

[28] F. Menter. “Zonal Two Equation $k-\omega$, Turbulence Models for Aerodynamic Flows”. In: *AIAA Paper* 93-2906 (1993).

[29] A. Spinelli, G. Cammi, M. Zocca, S. Gallarini, F. Cozzi, P. Gaetani, V. Dossena, and A. Guardone. “Experimental observation of non-ideal expanding flows of Siloxane MDM vapor for ORC applications”. In: *Energy Procedia* 129 (2017), pp. 1125–1132.

[30] A. Guardone, M. Zocca, G. Cammi, and A. Spinelli. “Oblique waves in the non-ideal compressible-fluid regime”. 2017.

[31] W. S. E.F. Toro M. Spruce. “Restoration of the contact surface in the HLL-Riemann solver”. In: *Shock Waves* (1994).

[32] F. Cozzi, A. Spinelli, M. Carmine, R. Cheli, M. Zocca, and A. Guardone. “Evidence of complex flow structures in a converging-diverging nozzle caused by a recessed step at the nozzle throat”. In: *J. Chem. Eng*. 2016.

[33] A. Spinelli, F. Cozzi, G. Cammi, M. Zocca, P. Gaetani, V. Dossena, and A. Guardone. “Preliminary characterization of an expanding flow of siloxane vapor MDM”. In: *1st International Seminar on Non-Ideal Compressible-Fluid Dynamics for Propulsion and Power, Varenna, Italy, 20-21 October*. 2016.

CHAPTER 6

TOWARDS AN IMPROVED THERMODYNAMIC MODEL CALIBRATION

6.1 Introduction

The characterization of NICFD flows is not only of theoretical interest, but it is also relevant to applications such as Organic Rankine Cycle (ORC), supercritical CO_2 power systems, turbogenerators, refrigerators and many others [1–4] Indeed, well-established and accurate thermodynamic models predict that several fluids, currently employed in industrial processes, feature non-ideal effects. Therefore, the performances of devices working with such substances is subject to unusual phenomena which are utterly dominated by the properties of the specific compound. Unfortunately, the behavior of these substances is still unclear and our knowledge is largely affected by uncertainty. This lack of knowledge follows from a remarkably scarce amount of experimental evidences collected in the past decades. The difficulties encountered in running experiments mainly lies in the fact that the conditions of interest are close to the thermal stability point of the compound. Practically, this poses a key feasibility issue because of a likely fluid chemical decomposition during experiments. Recently, the scientific community managed to overthrow some of the experimental-related issues and significant advancements have been achieved in the field of NICFD. The offspring of experimental facilities for the investigation of non-ideal flows goes so far as to envision that a considerable amount of data will be soon available. Certainly, this calls for the development of novel and reliable tools, to take advantage of data collected in experiments. Lately, the community started to tackle the issue by dedicating remarkable efforts to the development of numerical tools tailored for the investigation of complex fluid properties. Note that all the works published up to date are proof of concept since they rely on synthetic data and not on real experimental measurements. In [5] the authors propose a possible uncertainty-quantification based approach to assess the accuracy of the thermophysical sub-model implemented in non-ideal Computational Fluid Dynamic solvers. In [6], a Bayesian calibration of a computer model of the real process is carried out to update the epistemic uncertainty of ultrasonic flow meter measurements under non-ideal flow conditions. Ref. [7] proposed a Bayesian inference methodology, to calibrate complex equations of state used in numerical fluid flow solvers, based on synthetic aerodynamic data regarding a dense gas flow over a wing section.

In Cha. 5, it was shown how predictions from numerical tools compare w.r.t. the first ever experimental measurements of non-ideal supersonic expanding flows. Here, a Bayesian framework is developed to infer the true value of the material-dependent parameters appearing in thermodynamics models suitable for non-ideal flows. The goal is to improve the accuracy of predictions, w.r.t. the experimental measurements, from the numerical model presented in Cha. 5.

Bayesian inference is a wide-spread technique which can be applied to deduce relevant quantities that can not be directly measured from experiments. The framework is tailored on the TROVA test-rig at Politecnico di Milano [8–10] and it is intended to evaluate the potential analysis which could be done on NICFD flows data.

The goal is to infer the parameters appearing in the Peng-Robinson (PR) fluid model [11] and to draw the attention to the potential uncertainties underlying state-of-the-art fluid models.

The challenge lies in the fact that the non-ideal region is found in the close proximity of the liquid saturation curve, near the critical point. This require the vapor to be brought at conditions favorable to condensation or at which chemical decomposition is very likely. The occurrence of these two phenomena is obviously detrimental for the experimental facility and, therefore, it prevents one to obtain measurements suitable for the inference of the fluid parameters. Nevertheless, non-ideal effects are more and more relevant as the state of the fluid is pushed towards these limits, so the challenge is to balance test conditions in order to collect useful measurements yet maintaining a stable chemical equilibrium.

The considered experiment consists in the non-ideal expansion of a supersonic flow across a converging diverging nozzle (see Sec. 5.4.1 for further details). Once again, the fluid under investigation is MDM siloxane. This compound is of the utmost importance for ORC applications as it is employed as working fluid in many power production plants. The experiment was chosen because of its simple configuration and because it aims at producing an isentropic flow. For this reason, the flow field does not feature detached/separated regions or large scale turbulent structures as well as discontinuities like shock-waves.

In the chapter, Sec. 6.2 describes the Bayesian framework. In Sec. 6.3, the aleatoric uncertainties affecting the experiment and the fluid model are characterized. Sec. 6.4 describes the construction of surrogate models (according to the procedure reported in Sec. 5.3) which are exploited to hasten the inference process. 'In order to assess the framework capabilities without dealing with model errors due to geometrical approximations or with measurement error, synthetic data are generated using the state-of-the-art fluid model (Sec. 6.5). By exploiting this data set, an insight of the potentiality of Bayesian techniques for non-ideal flows is provided in (Sec. 6.6). The strengths and the weaknesses of the inference procedure are therefore discussed. Eventually, Sec.6.7 reports the first attempt to infer the parameters using the real experimental measurements. The experimental configuration and the suitability of data collected in the TROVA test rig are ultimately discussed.

6.2 The Bayesian Framework

Bayes' law (or rule) is a well-known theorem in probability theory and statistics. Among the many possible applications of Bayes' theorem, our interest is focused on Bayesian inference, a particular approach to statistical inference. Generally, probabilities are assigned based on observations and logical reasoning and therefore they may have a different interpretation to different subjects. Bayes' theorem expresses how a subjective degree of belief should rationally change to account for the availability of related evidences. The theorem describes the probability $\mathcal{P}$ of an event based on prior

knowledge of conditions that might be related to such event, and it reads

$$\mathcal{P}(A \mid B) = \frac{\mathcal{P}(B \mid A)\,\mathcal{P}(A)}{\mathcal{P}(B)}, \tag{6.1}$$

where A and B are events and $\mathcal{P}(B) \neq 0$. The conditional probability $\mathcal{P}(A \mid B)$ is the likelihood of event A occurring given that B is true. Naturally, $\mathcal{P}(B \mid A)$ is also a conditional probability of event B occurring given that A is true. On the other hand, $\mathcal{P}(A)$ and $\mathcal{P}(B)$ are the marginal probabilities i.e., the probabilities of observing A and B independently of each other.

In Bayesian inference problems, one tries to estimate the probability density function of event B given the observations of a certain number of realizations. In this sense, $\mathcal{P}(B)$ is defined as the *posterior* probability distribution as it is obtained after all the available information are integrated.

First, all the information related to our degree of belief about the event, before any evidence is taken into account, must be provided. $\mathcal{P}(A)$ is indeed referred to as the *prior* probability distribution of the uncertain quantity and it is intended to specify the prior knowledge one could have about the event. Additionally, Eq. 6.1 must be complemented with the conditional probability $\mathcal{P}(A \mid B)$, or likelihood. The likelihood may be interpreted as the measure, or the amount of information, that the data provides about the true value of the inferred parameter. According to Bayes' theorem, the combination of the information included in the prior distribution with those yield by the likelihood allows to retrieve the posterior distribution $\mathcal{P}(B)$ of the unknown parameter(s).

In the following, the goal consists in inferring the true value of a set of unknown parameters $\mathbf{q}$ of dimension 6 which includes the TROVA operating conditions (P^{t} and T^{t} at the nozzle inlet) and the PR model parameters (P_{cr}, T_{cr}, ω and γ). To achieve this goal, the process takes advantage of experimental measurements, or observations, $\mathbf{o}$. According to this notation, the Bayes theorem reads

$$\mathcal{P}(\mathbf{q} \mid \mathbf{o}) \propto \mathcal{P}(\mathbf{o} \mid \mathbf{q})\,\mathcal{P}(\mathbf{q}), \tag{6.2}$$

being $\mathbf{q} = (P^{\mathrm{t}}, T^{\mathrm{t}}, P_{cr}, T_{cr}, \omega, \gamma)^T$. Note that Eq. 6.2 misses the denominator in the right hand side. Bayes' rule now consists in a proportional relation but this doesn't actually affect the outcome of the inference procedure as the term $\mathcal{P}(B)$ simply acts as a scaling factor.

Given N_e experiments, the likelihood function $\mathcal{L}_j$ (where subscript j labels the experimental run) is assumed to be a Gaussian-like distribution centered on the experimental observation, namely

$$\mathcal{L}_j = \Pi_i \exp\left(-\frac{\left(O_{ij} - O^s_{ij}\right)^2}{2\sigma^2_{ij}}\right), \quad i = N_p, \tag{6.3}$$

where N_p corresponds to the number of sensors placed in the test section i.e., the number of measurements available for a single experiment. $O_{ij} \in \mathbf{o}_j$ is the measure at probe i for the experimental run j and σ_{ij} is the related 2σ interval.

O^s_{ij} is the value of the observable predicted by the Computational Fluid Dynamics (CFD) framework, which is ultimately substituted with a surrogate model.

According to the latter statements, the posterior PDF of the inferred variables can be expressed as

$$\mathcal{P}(\mathbf{q} \mid \mathbf{o}) \propto \Pi_j \mathcal{L}_j \mathcal{P}(\mathbf{q}), \qquad j = N_e, \tag{6.4}$$

The posterior has a complex structure which can not be retrieved analytically. To overcome this issue, we rely on a Markov-Chain Monte-Carlo (MCMC) approach. MCMC algorithms are generally used for sampling from multi-dimensional distributions with a large number of dimensions. Among the MCMC based methods, the Metropolis-Hastings (MH) algorithm [12] is here used to obtain a sequence of random samples from a complex probability distribution.

To carry out the investigation presented here, PCE surrogate models are employed (see Sec. 5.3). Metamodels serve to mimic the CFD solver and to significantly hasten the unroll of the MCMC chain.

6.3 Uncertainties: Prior PDFs

The PR EoS is built on top of a set of material-dependent parameters which must be inferred from experimental measurements or derived from theoretical models. Reference values can be usually found in literature and they are often given with a related uncertainty. Unfortunately, the shortage of experimental data regarding the complex compounds of interest here limits our chances to rely on accurate references. Indeed, the few available data were collected at specific fluid conditions and no measurements are found for a broader range of thermodynamic state variability. Moreover, not all the fluid model parameters are directly measurable and they have to be extrapolated from combined measurements. As a results, the estimation of reference values is strictly related to the particular test-rig used to conduct the experiments and it is largely affected by the assumptions made in the post-processing process. This often leads to discrepancies in the reference values reported by different authors. For instance, the value of P_{cr} for MDM reported by [13] is 1460 [kPa] while it is 1420 [kPa] in [14], 1415 [kPa] in [15] and 1437.5 [kPa] in [16]. From the lowest to the largest reference value, a variation of $\approx 3.18\%$ is found. Furthermore, if measurements uncertainties are considered then the variability is even larger.

Only uniformly distributed priors $\mathcal{P}(\mathbf{q}) \sim \mathcal{U}_{\mathbf{q}}[\mathbf{q}_{min}, \mathbf{q}_{max}]$ are considered hereinafter. Priors bounds are selected to largely encompass reference values found in literature or they are established according to thermodynamic stability criteria or physical limits. The operating conditions are also treated as uncertain parameters and they are included in the inference process. The uncertainty on the operating

	Operating Conditions		Model Parameter			
	P^{t}	T^{t} [K]	P_{cr} [Pa]	T_{cr} [K]	ω [-]	γ [-]
Nominal	458569.3	512.56	1400000	560	0.5	1.0183170
Uncertainty	$\pm$ 2%	$\pm$ 2%	$\pm$ 5%	$\pm$ 3 %	$\pm$ 70 %	$\pm$ 0.13 %

Table 6.1: bayesian inference problem. Priors are uniform distributions centered on the nominal value. The distance of prior bounds from the center is expressed as percentage of the nominal value;

conditions is assumed to be way larger than the interval from the actual experiment. Reference values and their bounds are reported in Tab. 6.1.

Given that $\mathcal{U}$ points out a uniform probability distribution, the Bayes theorem ultimately reads

$$\mathcal{P}(\mathbf{q} \mid \mathbf{o}) \propto \Pi_j \mathcal{L}_j \mathcal{U}_{\mathbf{q}}, \qquad j = N_e \tag{6.5}$$

6.4 Surrogate models construction

The stochastic space has dimension 6 ($\mathbf{q} \in \mathbb{R}^6$). First, the unknown parameters are transformed to scale the support of the prior distribution to $[0,1]$. The parameters are therefore expressed in terms of the vector $\xi \in \mathbb{R}^6 \sim \mathcal{U}_\xi[0,1]$, with $\xi = (\xi^{P^{\mathrm{t}}}, \xi^{T^{\mathrm{t}}}, \xi^{P_{cr}}, \xi^{T_{cr}}, \xi^{\omega}, \xi^{\gamma})^T$ To build the surrogate, up to 4 samples are taken along each direction of the stochastic space, leading to a total of $M = 4^6 = 4096$ quadrature points for the computation of the PCE coefficients. CFD simulations are carried out using the non-ideal solver included in SU2 [17–19]. All the realizations were carried out considering the very same numerical set up and the very same computational grid. To lower the burden, realizations are obtained under the inviscid flow assumption. This assumption is justified by the results reported in Sec. 5.4.1, where viscous effects are shown to have a negligible effect. Indeed, the pressure trend is almost insensitive to the presence of the boundary layer and the only remarkable viscous effect is found in the close proximity of the discharge section.

Following what is presented in Sec. 5.4.1, grid independence (w.r.t. the computed pressure trend) is achieved using approximately 10k points. For each realization m, a reduction of at least 7 order of magnitude is guaranteed for the residual related to the density. 6 order of magnitude are granted for the ones related to the energy. A multigrid hierarchical approach is exploited: three levels of grid resolution are employed to further accelerate numerical convergence.

Once all the M realization were unrolled, the PCE surrogate models were built on top of the numerical solutions. Fig. 6.1(a) reports the mean pressure trend along the nozzle centerline, as predicted by metamodels of different polynomial order. Similarly, Fig. 6.1(b) reports the variance. No remarkable differences are found between

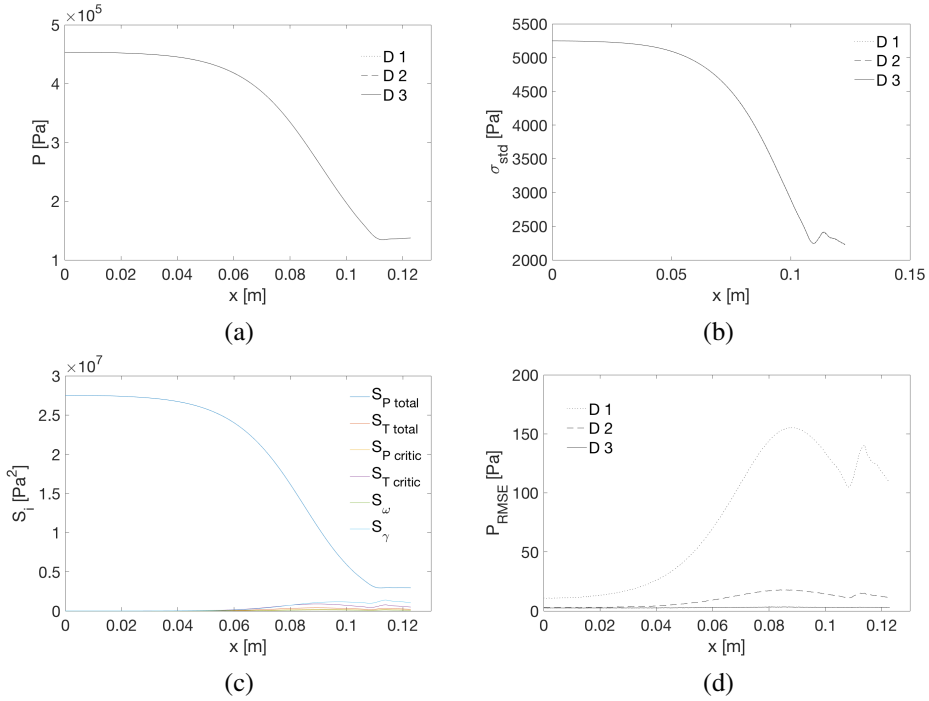

Figure 6.1: comparison of diverse PCE order (D). (a) Mean pressure along the nozzle centerline; (b) Pressure variance along the nozzle centerline; (c) Sobol indexes along the nozzle centerline, scaled by the variance; (d) RMSE w.r.t. additional sampling points from the stochastic space;

the results returned by a polynomial of order 1, 2 or 3. Fig. 6.1(c) reports the Sobol Indexes (using D 3 and scaled by the variance) for the pressure along the nozzle. As clear from the plot, the problem is largely dominated by the uncertainty over the value of total pressure at the inlet. Its importance decreases towards the discharge section, where the specific heat ratio γ is found to gain relevance.

The accuracy of the surrogate model was also assessed: a total of 729 stochastic points were further sampled. These points do not coincide with any of the 4096 points used to build the metamodel. CFD simulations using SU2 were once again carried out, to obtain the solution at the 729 points. The solution was compared with predictions from the surrogate models, the L_2 error is plotted in Fig. 6.1(d), for different polynomial orders. The PCE with the largest order (D 3) has an almost negligible error at every point along the centerline. Therefore, PCEs of order 3 were selected to lighten the Bayesian procedure.

P^t	T^t [K]	P_{cr} [Pa]	T_{cr} [K]	ω [-]	γ [-]
458569.3	512.56	1437500	565.3609	0.524	1.0183170

Table 6.2: parameter values set for the generation of the synthetic data;

6.5 Synthetic data generation

The FluidProp library [20] is coupled to the SU2 non-ideal solver, to provide access to the state-of-the-art fluid model for MDM. The multiparameter fluid model based on the Helmholtz potential [16] is exploited to model the thermodynamics of the flow across the TROVA test section. A generalized Approximate Riemann solver (ARS) of Roe type was employed. Second-order spatial accuracy is guarantee by a Monotone Upstream-centered Schemes for Conservation Laws (MUSCL) approach. The van Albada slope limiter is used to facilitate the numerical convergence, to prevent and suppress possible spurious oscillations that may appear during the transient from the initial condition to the steady state solution.

A viscous, fully turbulent, two-dimensional simulation of the TROVA test section is carried out for the selected experimental configuration, using a grid made up of $\approx 59k$ points. The boundary mesh employs 80 layers, whereas the height of the first cell is set to be in the order of $10^{-6}[m]$, approximately in the $y^+ = 1$ limit. The Menter's Shear Stress Transport (SST) [21] model is used to close the RANS equations. The operating conditions (P^t and T^t) were chosen to reproduce one of the latest experiments recently carried out at Politecnico di Milano (Exp. A_2 in Sec. 5.4.1). Tab. 6.2 reports the values of the parameters used to produce the synthetic data. The values in Tab. 6.2 correspond to those from [16].

The solution is extracted at four different locations along the nozzle centerline. Synthetic measurements of static pressure, static temperature, Mach number and flow velocity are therefore obtained. Fig. 6.2(a) reports a comparison (plot is an enlargement of the nozzle discharge section) of the synthetic pressure trend against the trend predicted by the PR EoS, using the nominal values reported in Tab. 6.1. Pressure trends are almost superimposed and small differences, possibly due to viscosity effects, are found only in the close proximity of the discharge section. For this reason, the position of the measuring point is such to avoid the final portion of the nozzle. Synthetic data are extracted at $x_1 = 0.015$ [m], $x_2 = 0.045$ [m], $x_3 = 0.075$ [m] and $x_4 = 0.105$ [m]. The QoI are the static pressure P^s, the static temperature T^s, the Mach number M and the speed of the flow $\|\mathbf{v}\|$. These quantities were chosen as they are the ones practically measurable in an experiments using the TROVA test-rig. Concerns may be raised about obtaining static temperature measurements. Indeed, thermocouples should be placed within the stream, thus heavily affecting the flow. Moreover, nozzle walls are artificially heated, to avoid condensation during the discharge. Therefore, the assembly of thermocouples should be provided by insulating

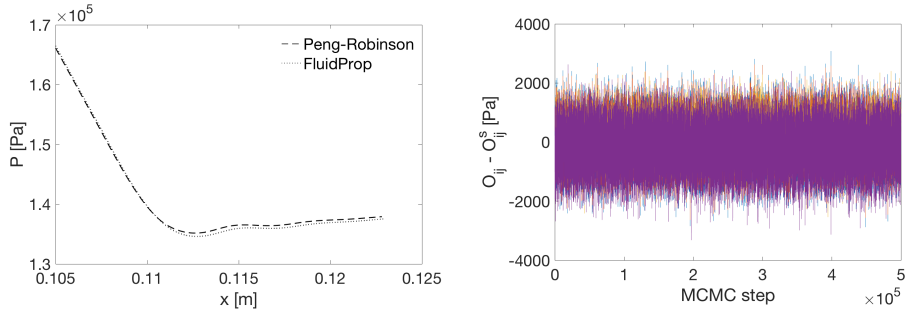

(a) (b)

Figure 6.2: (a) Comparison of pressure trends as obtained using FluidProp (RANS simulation) and the PR EoS (inviscid simulation). Enlargement of the nozzle discharge section; (b) Calibration on synthetic pressure data: difference ([Pa]) between the synthetic value of pressure at the 4 locations and the surrogate models predictions, for any given combination of the 6 parameters in the MCMC chain);

Measure	Probe position			
	x_1	x_2	x_3	x_4
P^s [Pa]	452753	441586	362708	165776
U_{P^s} [Pa]	± 1000	± 1000	± 1000	± 1000
T^s [K]	512.373	511.998	509.217	499.906
U_{T^s} [K]	± 1	± 1	± 1	± 1
M [-]	0.176185	0.30143	0.727538	1.42934
U_M [-]	± 5 %	± 5 %	± 5 %	± 5 %
$\|\|\mathbf{v}\|\|$ [m/s]	19.373	33.3562	83.9179	± 179.023
$U_{\|\|\mathbf{v}\|\|}$ [m/s]	± 1 %	± 1 %	± 1 %	± 1 %

Table 6.3: synthetic measurements at station x1-x4 and related uncertainty;

layer. Nevertheless, as we are dealing with synthetic data we will consider temperature measurements as feasible.

6.6 Fluid Model Calibration Using Synthetic Data

The calibration of the fluid model parameters is carried out for diverse combinations of measurements. This is aimed at stressing out the relevance of each physical quantity to the inference of fluid properties. Synthetic data are exploited to evaluate the potential of the Bayesian framework for the investigation of the properties of fluids

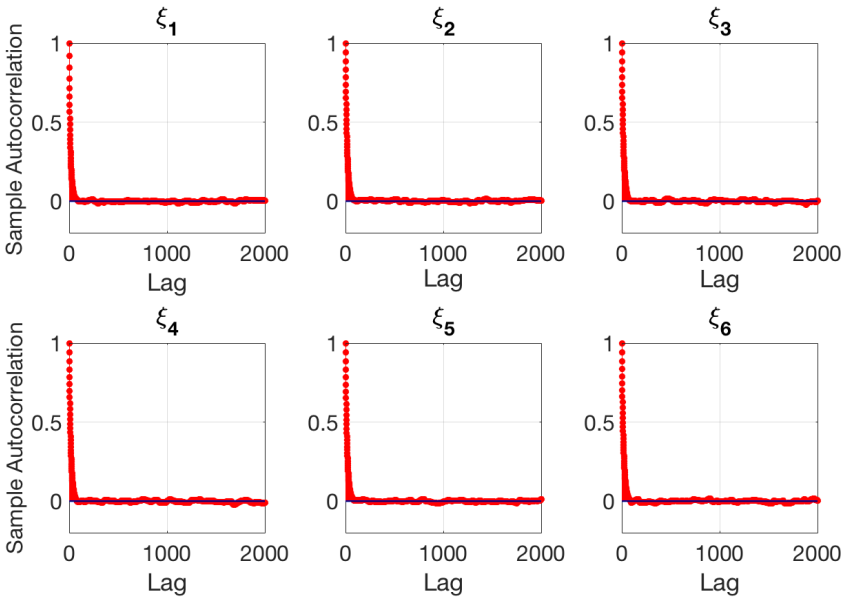

Figure 6.3: calibration on synthetic pressure data. Sample autocorrelation of each parameter;

of interest for NICFD without having to deal with measurement bias or model errors. Note that use the expression *model error* as a general term referred to the numerical description of the flow field. The term is therefore comprehensive of errors due to approximations made to simplify the geometry, of errors arising from the decomposition of the domain into grid elements and of errors due to the specific implementation of the CFD solver. For all the tests presented hereinafter, $100k$ MCMC steps were unrolled to adapt the covariance matrix to the particular probability distribution (*burnout phase*). $500k$ sampling steps were instead collected in the unfolding of the MCMC chain.

6.6.1 Pressure measurements

First, the calibration procedure is carried out considering only static pressure measurements P^s. The MCMC chain shows a pretty good mixing, reported in Fig. 6.2(b). Namely, Fig. 6.2(b) reports the difference between the synthetic value of pressure at the 4 locations, and the values predicted by the surrogate models for any given combination of the 6 parameters in the MCMC chain. As shown in Fig. 6.2(b), the framework succeed in finding combinations of parameters that nullify the difference. Fig. 6.3 reports instead the autocorrelation function for the 6 parameters, along the MCMC chain. As shown in plots, the autocorrelation decays quickly for all the parameters meaning that the sampling process shortly becomes independent from the

starting point.

The posteriors resulting from the unfolding of the MCMC chain are reported in Fig. 6.4. On the diagonal, the posteriors of P^{t}, T^{t}, P_{cr}, T_{cr}, ω and γ are reported in this exact order (from top-left to bottom-right corner). Unfortunately, the posteriors are poorly informative. Indeed, only the probability distribution related to the value of P_t is sufficiently sharp to identify a limited range of most-likely values. The remaining posteriors tell that a large range of values are almost equally probable. On the upper extra-diagonal slots of Fig. 6.4, the points sampled along the chain are projected onto a 2D stocastic space whose directions correspond to the $i-th$ and the $j-th$ variable in ξ. These plots show us that the MCMC algorithm is able to explore the complete stochastic space without finding any attractive region (except for the stochastic direction related to P_t). Similarly, the lower off-diagonal slots in Fig. 6.4 report the joint probability distribution resulting from the combination of the $i-th$ and the $j-th$ posteriors. In these plots, warmer colors identify the region of the stochastic space where the true parameter values are likely to lie.

6.6.2 Pressure, Mach and flow velocity measurements

In this section, the outcome of the calibration algorithm as obtained by including also Mach number and flow speed measurements is presented. These three quantities (Pressure, Mach and flow speed) represent the ones potentially measurable in the TROVA test-rig. Practically, the Mach can be measured in a large number of points in the domain, whereas the flow is supersonic. Here, we are dealing with synthetic data therefore we can avoid bothering with the constrain of taking measures in a supersonic region of the flow only.

The speed of the flow may be measured using a Laser Doppler Velocimetry (LDV) technique. Though a preliminary work regarding the application of this method to non-ideal flows was done [22], many issues still remain unsolved and question its practical feasibility, at least about its effectiveness in the TROVA test-rig. Nevertheless, the LDV technique still retain some potential that may be unleashed in future developments.

We considered 4 measure points, both for Mach number and for flow velocity, corresponding to the very same location of pressure taps. Once again, the MCMC chain unfolding reveals a good mixing and a fast autocorrelation decay (not reported). Fig. 6.5 shows the posterior PDFs, on the diagonal slots, the points of the MCMC chain in a 2-dimensional space, on the upper off-diagonal slots, and the joint probability distributions, on the lower upper off-diagonal positions. The posteriors reveal that the combination of the three measures of pressure, Mach and velocity may be beneficial to slightly improve (but still not sufficiently enough) the inference of T_t and of the specific heat ratio γ. Nevertheless, little or no information are provided about the critical quantities and the acentric factor.

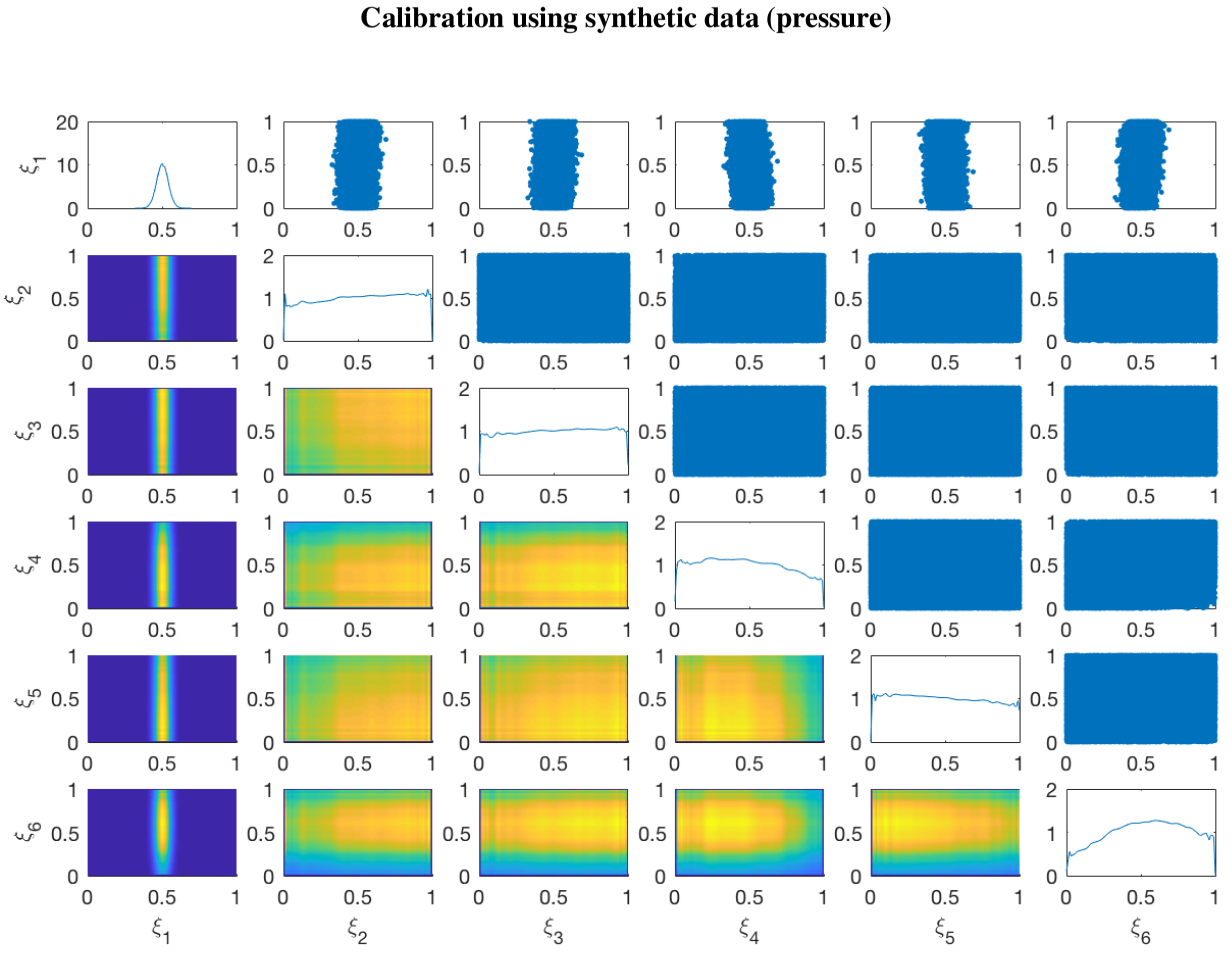

Figure 6.4: calibration of the PR EoS. MCMC results considering synthetic pressure data. Posteriors are reported in the diagonal slots. Figures on the upper extra-diagonal slots report the chain points projected onto a 2 stocastic directions. Lower off-diagonal slots report the joint probability distribution resulting from the combination of the $i-th$ and the $j-th$ posteriors;

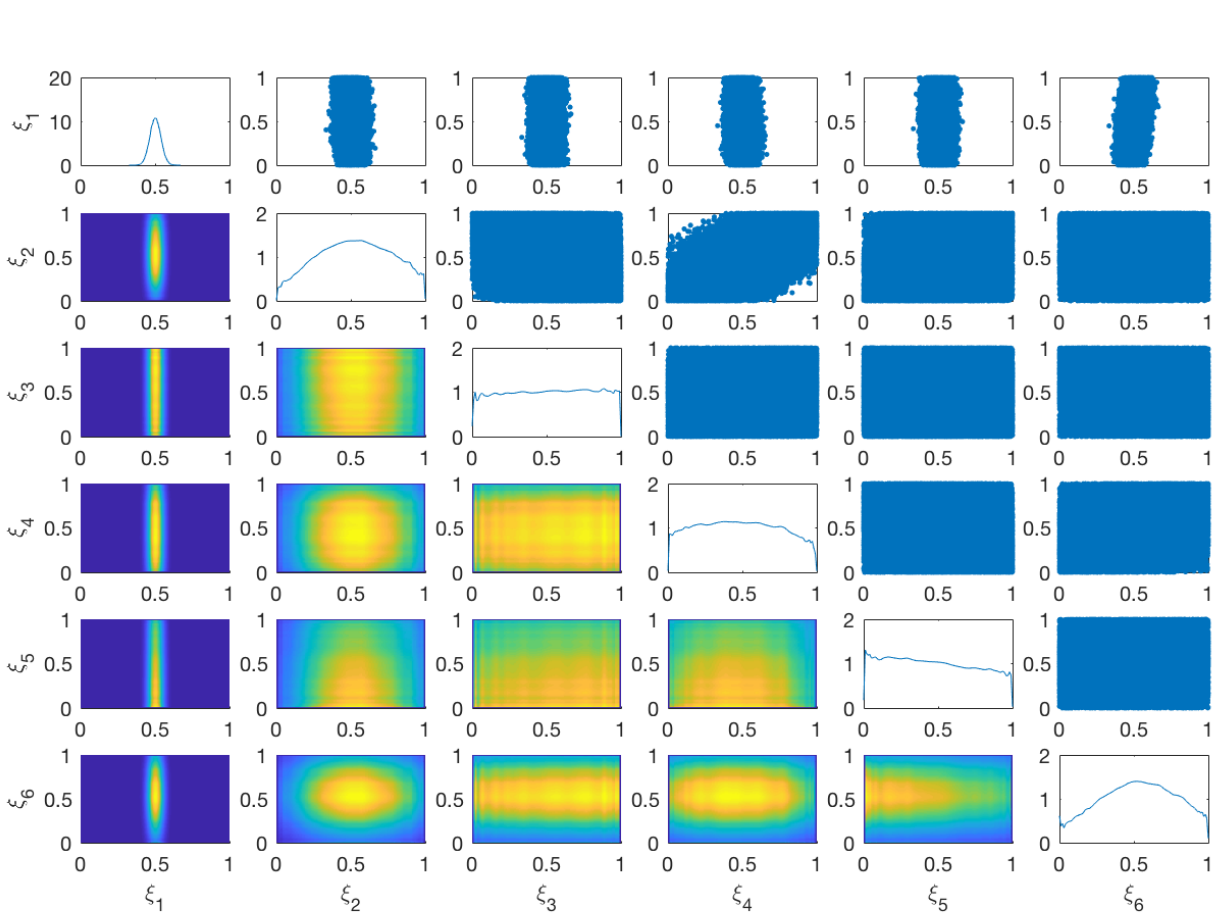

Figure 6.5: calibration of the PR EoS. MCMC results considering synthetic pressure, Mach, and Velocity data. Posteriors are reported in the diagonal slots. Figures on the upper extra-diagonal slots report the chain points projected onto a 2 stocastic directions. Lower off-diagonal slots report the joint probability distribution resulting from the combination of the $i-th$ and the $j-th$ posteriors;

6.6.3 Pressure and Temperature

In this case, synthetic data provide measurements of pressure and temperature. Technically, the measure of temperature within the TROVA test section would be quite difficult and quite invasive. Nevertheless, we provide here an assessment of the possible benefit that such information could yield to the calibration of the fluid model parameters.

Once again, the chain mixing and the autocorrelation decay show a very nice trend, confirming the reliability of the MCMC procedure. Fig. 6.6 reveals that the addition of the temperature measure would be very beneficial to the inference of a few parameters. In particular, now the posterior related to the value of T^{t} at the domain inlet is very narrow. On the other hand, also the posterior of the γ is now much narrower, providing a good estimation of its true value. This was somehow expected as the value of γ is strictly related to the vibrating modes of the molecules, which ultimately depends on the temperature of the gas. Unfortunately, the posteriors of P_{cr}, T_{cr} and ω still remain non-informative. Nevertheless, results show that temperature measurements would be of utmost relevance for the investigation of complex fluid flows.

6.7 Fluid Model Calibration Using Real Data

In this section, the actual experimental measurement collected in the TROVA test-rig are exploited to infer the true values of the PR fluid model. Data are available from two different TROVA discharges (1 and 2). During each discharge, pressure was measured at 5 different time instances ($A - E$) at 4 different locations. The reader is referred to Sec. 5.4.1 for a throughout description of the experiments and for a detailed summary of test conditions (Tab. 5.1 and Tab. 5.2). Measurements at each of the considered time instances $A_1 - E_1$ and $A_2 - E_2$ are reported in Tab. 5.3 and Tab. 5.4. Again, $100k$ MCMC steps were unrolled for the burnout phase while $500k$ sampling steps were collected in the unfolding of the MCMC chain.

First, only one experiment is accounted in the construction of the likelyhood function. The considered experiment (labeled A_2) was earlier exploited to assess the framework against synthetic data (see Sec. 5.4.1). Results reveal that the MCMC algorithm struggles to find a combination of parameters that nullify the difference between the measured and the predicted quantities. Fig. 6.7(a) reports the such difference for the 4 pressure tabs. As clear from Fig. 6.7(a), there is no parameters combination which allow to match all the 4 observations at the same time. Indeed, the difference is nullified only for the pressure tab placed at x = 69.4 [mm] (orange line).

The resulting PDFs for the element ξ_i of ξ vector are reported in Fig. 6.8. Generally, the mass of the posteriors is accumulated over the upper of the lower bounds. This reveals that the sampling algorithm is trying to explore regions of the stochastic

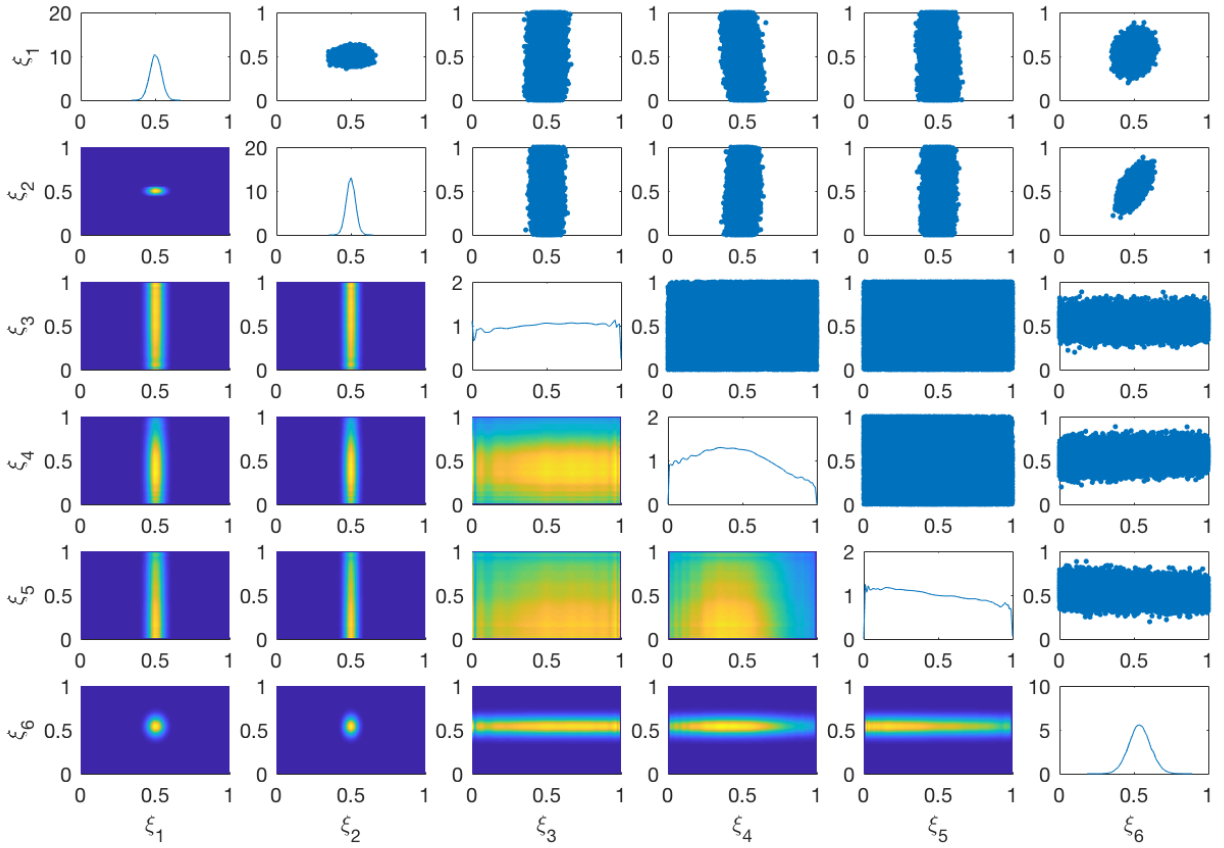

Figure 6.6: calibration of the PR EoS. MCMC results considering synthetic pressure and temperature data. Posteriors are reported in the diagonal slots. Figures on the upper extra-diagonal slots report the chain points projected onto a 2 stocastic directions. Lower off-diagonal slots report the joint probability distribution resulting from the combination of the $i-th$ and the $j-th$ posteriors;

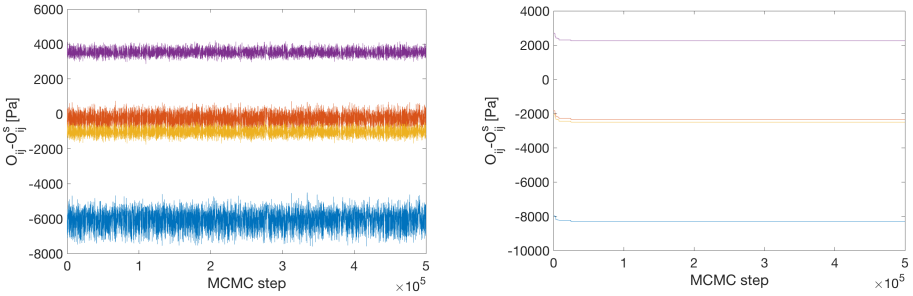

(a) (b)

Figure 6.7: calibration of the PR EoS. (a) Chain mixing considering experiment A_2; (b) Chain mixing considering experiments $A_1 - E_1$ and $A_2 - E_2$;

space which are not admissible from the physical point of view. The posterior of ξ_1, related to the total pressure P^t at the nozzle inlet, is fully contained within the prior range. Though the ξ_1 PDF has quite narrow support, its mass is quite drifted towards the upper bound. This would mean that the real operating conditions are far from the ones measured during the experiment but, given the lack of reliability of the inference process w.r.t. the other unknown parameters, such conclusion shall not be considered.

The inference procedure is again carried out accounting all the available observation from the experiments $A_1 - E_1$ and $A_2 - E_2$ but the addition of more observation does not improve the results. The chain is characterized by a very low acceptance rate and its mixing is reported in Fig. 6.7(b), where it is possible to observe the chain spoiled behavior. The resulting posteriors are therefore not reasonable.

6.8 Conclusions

In the chapter, a Bayesian framework for the investigation of non-ideal flows of interest for renewable energy applications is presented. The framework aims at inferring the parameters of the Peng-Robinson fluid model for a vapor of siloxane MDM and to evaluate the potential analysis which could be done on non-ideal flows. Namely, the procedure presented in the chapter attempts to infer the material dependent coefficients appearing in the Peng-Robinson fluid model for a siloxane MDM fluid. The inference process is based on a synthetic data set extrapolated from a high-fidelity simulation of an actual experiment realized at the TROVA test-rig at Politecnico di Milano. The choice of relying on a synthetic data set was made so to avoid dealing with any possible measurement bias or epistemic uncertainty underlying the CFD representation of the test-section.

Results reveal that the considered experiment may not be suitable for the goal of inferring the Peng-Robinson model coefficients for MDM. Indeed, it is virtually shown that, despite all the possible measured quantities (pressure, temperature, flow

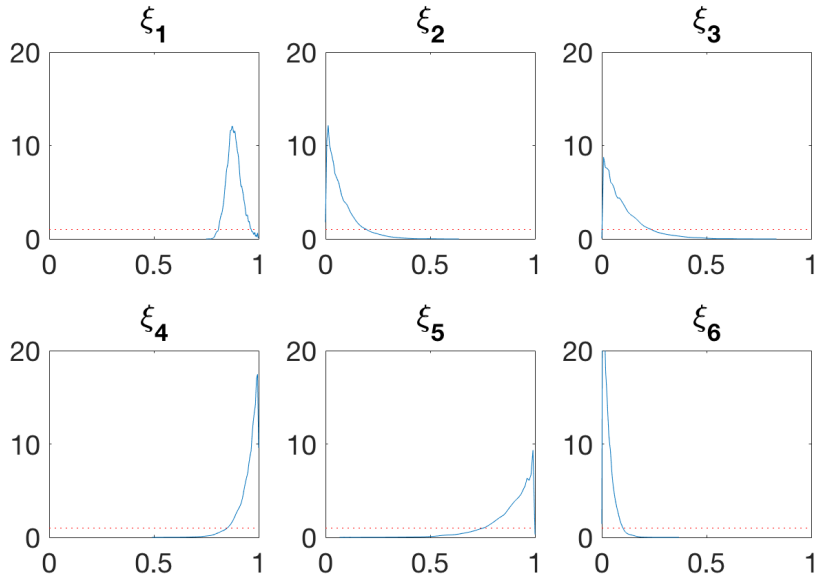

Figure 6.8: calibration of the PR EoS. PDFs resultimg from the MCMC chain obtained considering experiment A_2;

velocity and flow Mach number), little may be potentially learned from the experimental data set. Indeed, among the six considered variables, only three were endowed with informative posterior PDFs. Moreover, two of these parameters are relative to the operating conditions of the facility during the experiment, therefore they do not provide any relevant information about the thermodynamics of the fluid. An attempt to infer the uncertain parameters was also carried out using real experimental measurements of static pressure. Unfortunately, the Bayesian framework fails in finding a combination of values, within the limit of physical admissibility, that allows numerical predictions to match the experimental measurements. Indeed, for most parameters the mass of the posterior probability distribution is accumulated over the upper or the lower bounds. This points out either an epistemic uncertainty underlying the computational model of the test section (including a possible epistemic uncertainty affecting the state-of-the-art fluid model for complex compound) or a biased experimental measurement process.

Ultimately, the findings reported in the chapter reveal that the considered experiment may not be suitable for inferring the material-dependent coefficient included in the Peng-Robinson fluid model. Nevertheless, the framework is returning substantial indications towards the development of future experiments. For instance, though very difficult to obtain (at least in the TROVA test-rig), temperature measurements would be very beneficial to the inference process, as their inclusion helps sharpen-

ing the posterior distributions of some variables. Moreover, results reveal that, in the considered thermodynamic conditions, the problem is utterly dominated by the uncertainty over the value of total pressure at the domain inlet. In particular, in the considered experiment the flow is almost not sensitive to (even large) variations of the Peng-Robinson fluid model parameters. Though not easily achievable in practice, test conditions closer to the saturation curve, which foster more significant non-ideal effects and hopefully result in a larger sensitivity of the flow w.r.t. the model parameters, may yield an improved output of the inference process. Unfortunately, the feasibility of such experiment is questionable as the more extreme conditions would likely cause the molecules to decompose into simpler compounds. The search for different and more appropriate test conditions is left for future investigations.

References

[1] P. Colonna, N. R. Nannan, and A. Guardone. "Multiparameter equations of state for siloxanes:[(CH 3) 3-Si-O 1/2] 2-[O-Si-(CH 3) 2] i= 1,. . . , 3, and [O-Si-(CH 3) 2] 6". In: *Fluid Phase Equilib.* 263.2 (2008), pp. 115–130.

[2] P. Congedo, C. Corre, and P. Cinnella. "Numerical investigation of dense-gas effects in turbomachinery". In: *Comput. & Fluids* 49.1 (2011), pp. 290–301.

[3] A. Wheeler and J. Ong. "The role of dense gas dynamics on Organic Rankine Cycle turbine performance". In: *J. Eng. Gas Turbines Power* 135.10 (2013), p. 102603.

[4] P. Colonna, E. Casati, C. Trapp, T. Mathijssen, J. Larjola, T. Turunen-Saaresti, and A. Uusitalo. "Organic Rankine Cycle Power Systems: From the Concept to Current Technology, Applications, and an Outlook to the Future". In: *J. Eng. Gas Turb. Power* 137.10 (2015).

[5] A. Head, S. Iyer, C. de Servi, and M. Pini. "Towards the Validation of a CFD Solver for Non-ideal Compressible Flows". In: *Energy Procedia* 129 (2017). 4th International Seminar on ORC Power SystemsSeptember 13-15th, Milano, Italy, pp. 240–247. ISSN: 1876-6102.

[6] Z. Belligoli, R. Dwight, G. Kok, and P. Lucas. "A Bayesian study of uncertainty in ultrasonic flow meters under non-ideal flow conditions". In: *Metrologia* 54.4 (2017), p. 584.

[7] X. Merle and P. Cinnella. "Bayesian quantification of thermodynamic uncertainties in dense gas flows". In: *Reliability Engineering & System Safety* 134.Supplement C (2015), pp. 305–323. ISSN: 0951-8320. DOI: https://doi.org/10.1016/j.ress.2014.08.006. URL: http://www.sciencedirect.com/science/article/pii/S0951832014001999.

[8] A. Spinelli, M. Pini, V. Dossena, P. Gaetani, and F. Casella. "Design, Simulation, and Construction of a Test Rig for Organic Vapours". In: *ASME J. Eng. Gas Turb. Power* 135 (2013), p. 042303.

[9] A. Guardone, A. Spinelli, and V. Dossena. "Influence of Molecular Complexity on Nozzle Design for an Organic Vapor Wind Tunnel". In: *ASME J. Eng. Gas Turb. Power* 135 (2013), p. 042307.

[10] M. Pini, A. Spinelli, V. Dossena, P. Gaetani, and F. Casella. "Dynamic Simulation of a Test Rig for Organic Vapours". In: *Proceedings of 5th Conference on Energy Sustainability, ASME EsFuelCell2011, Washington, Washington DC, USA*. Aug. 2011.

[11] D. Y. Peng and D. B. Robinson. "A New Two-constant Equation of State". In: *Ind. Eng. Chem. Fundam.* 15 (1976), pp. 59–64.

[12] W. K. Hastings. "Monte Carlo sampling methods using Markov chains and their applications". In: *Biometrika* 57.1 (1970), pp. 97–109. DOI: 10.1093/biomet/57.1.97. eprint: http://biomet.oxfordjournals.org/cgi/reprint/57/1/97.pdf. URL: http://biomet.oxfordjournals.org/cgi/content/abstract/57/1/97.

[13] E. Dickinson, I. A. McLure, and B. H. Powell. "Thermodynamics of n-alkane + dimethylsiloxane mixtures. Part 2.—Vapour pressures and enthalpies of mixing". In: *J. Chem. Soc., Faraday Trans. 1* 70 (0 1974), pp. 2321–2327. DOI: 10.1039/F19747002321. URL: http://dx.doi.org/10.1039/F19747002321.

[14] D. Ambrose. "Vapor-Liquid Critical Properties". In: *NPL Report Chem* 107 (1980).

[15] D. D. Lindley and H. C. Hershey. "The orthobaric region of octamethyltrisiloxane". In: *Fluid Phase Equilibria* 55.1 (1990), pp. 109–124. ISSN: 0378-3812. DOI: https://doi.org/10.1016/0378-3812(90)85007-W. URL: http://www.sciencedirect.com/science/article/pii/037838129085007W.

[16] M. Thol, F. H. Dubberke, E. Baumhögger, J. Vrabec, and R. Span. "Speed of Sound Measurements and Fundamental Equations of State for Octamethyltrisiloxane and Decamethyltetrasiloxane". In: *Journal of Chemical & Engineering Data* 62.9 (2017), pp. 2633–2648.

[17] T. D. Economon, D. Mudigere, G. Bansal, A. Heinecke, F. Palacios, J. Park, M. Smelyanskiy, J. J. Alonso, and P. Dubey. "Performance optimizations for scalable implicit RANS calculations with SU2". In: *Computers & Fluids* 129 (2016), pp. 146–158. ISSN: 0045-7930. DOI: http://dx.doi.org/10.1016/j.compfluid.2016.02.003. URL: http://www.sciencedirect.com/science/article/pii/S0045793016300214.

[18] M. Pini, S. Vitale, P. Colonna, G. Gori, A. Guardone, T. Economon, J. Alonso, and F. Palacios. "SU2: the Open-Source Software for Non-ideal Compressible Flows". In: vol. 821. 1. 2017, p. 012013.

[19] G. Gori, M. Zocca, G. Cammi, A. Spinelli, and A. Guardone. "Experimental assessment of the open-source SU2 CFD suite for ORC applications". In: *Energy Procedia* 129.Supplement C (2017), pp. 256–263.

[20] P. Colonna, T. P. der Stelt, and A. Guardone. *FluidProp: A program for the estimation of thermophysical properties of fluids*. Energy Technology Section, Delft University of Technology, The Netherlands. 2005.

[21] F. Menter. "Zonal Two Equation $k-\omega$, Turbulence Models for Aerodynamic Flows". In: *AIAA Paper* 93-2906 (1993).

[22] S. Gallarini. "Design and commissioning of a laser Doppler velocimetry seeding system for non-ideal fluid flows". MA thesis. Italy: Politecnico di Milano, 2016.

CHAPTER 7

APPLICATION TO RELEVANT NICFD FLOWS

Part of the contents of this chapter appear in

D. Vimercati, G. Gori and A. Guardone, *Non-ideal effects on the typical trailing edge shock pattern of ORC turbine blades*, Energy Procedia, Vol. 129, 2017

P. Molesini, G. Gori and A. Guardone, *An analysis of fast-response pressure probes dynamics for ORC power systems*, Energy Procedia, Vol. 129, 2017

G. Gori, P. Molesini and A. Guardone, *Non-Ideal Compressible-Fluid Dynamics of Fast-Response Pressure Probes for Unsteady Flow Measurements in Turbomachinery*, Journal of Physics: Conference Series, Vol. 821, 2017

G. Gori and A. Guardone, *VirtuaSchlieren: A hybrid GPU/CPU-based schlieren simulator for ideal and non-ideal compressible-fluid flows*, Applied Mathematics and Computations, Vol. 319, 2018

7.1 Introduction

In the chapter, several contribution to the investigation of non-ideal compressible-fluid flows are presented. The SU2 NICFD solver is exploited to carry out numerical simulations of the non-ideal flow-fields considered in the following. In the first part of the chapter, the solver is used to carry out an analysis of the typical fish-tail shock pattern generated at the turbine blade trailing edge for ORC applications. The analysis aims at investigating possible non-ideal effects across oblique shock waves and the influence of thermodynamic conditions on the shock properties.

Secondly, the dynamics of pressure probes for high frequency measurements is investigated considering fluids in the non-ideal regime. In particular, the time-response is reconstructed with respect to step perturbations on the pressure field. This analysis is carried out to assess the effects of non-idealities on the time-response of devices typically employed to measure pressure fluctuations past an ORC turbine rotor.

Eventually, the non-ideal CFD solver is used to reconstruct the flow-field around exemplary geometrical configurations. The solution is postprocessed to generate the expected schlieren image of the test section. The procedure may provide an additional way to compare numerical results against experimental measurements.

7.2 Fish-tail shock Pattern at Turbine Blade Trailing Edge

The flow pattern at the trailing edge of supersonic high-pressure turbine blades is well understood [1] and it potentially comprises different wave systems (e.g. shock/shock, shock/Prandtl-Meyer fan) either at design or off-design conditions. Since the trailing

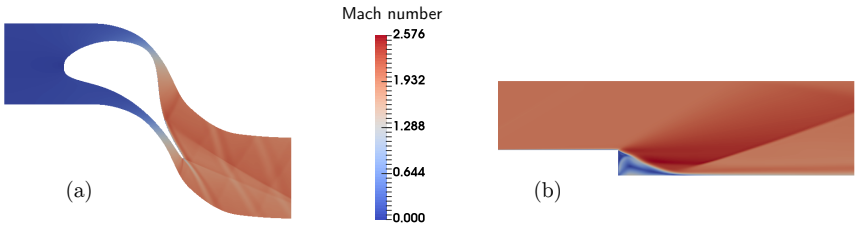

Figure 7.1: Mach number field of siloxane MDM as predicted using RANS calculations. (a) Flow within a typical ORC turbine vane, details on the geometry can be found in Ref. [4, 5]. Total upstream conditions $P^t = 8$ bar, $T^t = 272$ °C; (b) Flow over a backward facing step. Static upstream conditions $P = 1$ bar, $T = 242$ °C, $M = 2$;

edge has a finite thickness, a supersonic Prandtl-Meyer expansion occurs generating a limited region of separation between the high speed flows from the pressure and suction sides of the blade. The merging of these two supersonic flows results in the formation of compression waves that eventually form a characteristic shock pattern comprising two oblique shock waves, the so-called fish-tail shocks. In addition, shock and shock/fan systems can arise in case of a post-expanded channel design or at off-design conditions. In the theoretical case of infinitesimal trailing edge thickness, the post-expansion achieved by the deviation occurs through an oblique shock/Prandtl-Meyer fan system.

The supersonic stream at the trailing edge of the stator vanes may possibly result in large losses, making the trailing-edge region critical to turbine efficiency [2, 3]. Moreover, further losses are typically induced from shock-boundary layer interactions at the adjacent blades. Periodical mechanical stresses arise at rotor blades interacting with upstream shocks, which can be of relevant strength, especially at off-design conditions.

ORC turbine stator blades are particularly prone to this phenomenon since they are designed to provide a large outlet Mach number, especially at the first stage. These features are shown in Fig. 7.1(a), where the Mach number field is depicted for an exemplary ORC turbine vane with an exit Mach value approximately equal to 2.

Once again, non-ideal effects are investigated using siloxane vapor MDM as an exemplary organic fluid. The present results can be arguably extended to most vapors currently employed in ORC applications and they follow the study of [6], where the authors focused on non-ideal compressible-fluid effects on the flow turning angle resulting from the Prandtl-Meyer expansion, which influences the shape and size of the downstream recirculating region. One of the drawbacks of utilizing complex organic vapors lies in the low values of the speed of sound typically achieved within ORC expanders. This causes the flow to easily reach high Mach numbers at the nozzle exit. Note that, from the qualitative standpoint, the flow configuration at the trailing edge is similar to the one occurring in a supersonic flow over a backward

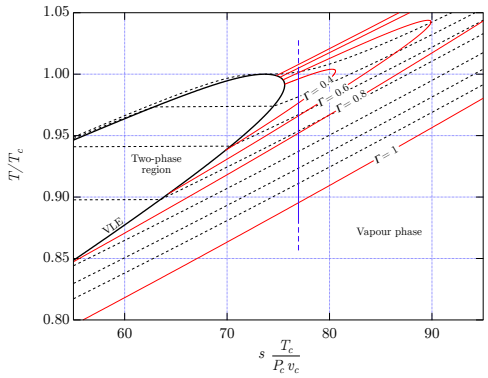

Figure 7.2: Temperature–entropy diagram for MDM, computed from the reference EoS [12], showing the selected isentrope (blue line) for the parametric studies, $s_{\mathrm{A}} = s(0.557P_c, 0.964T_c)$. Also shown is a set of isobars (black dashed lines) and Γ–contours (red lines);

facing step, see Fig. 7.1(b) and Cha. 5. Here, a supersonic Prandtl-Meyer expansion occurs and a limited region of separation is generated behind the step. At the end of the separation bubble, compressive waves coalesce into an oblique shock wave.

Recent investigations [7, 8] pointed out the influence of the fundamental derivative of gasdynamics Γ [9] on the flow pattern downstream the trailing edge, by comparing working fluids with increasing complexity. A reduction of the separated region is observed at decreasing values of Γ, associated with the larger turning angles that the flow sustains across Prandtl-Meyer waves. The shape and extension of the separated region largely affects the subsequent fish-tail structure, which can possibly deliver large flow angles deflections in order to match the flows from the suction and pressure blade surfaces. Both the molecular complexity of the compound and non-ideal effects influence the separation pattern and, consequently, the oblique shocks originating from it. The upstream thermodynamic state has a major influence on the fish-tail structure as, if $\Gamma < 1$, it governs the maximum flow turning angle and it may result in a non-ideal Mach number increase across a shock, see Ref. [10, 11].

In the following, subscript A and B refer, respectively, to the state of the fluid upstream and downstream the shock. Two parametric studies are conducted to assess the shock polar dependence on the upstream thermodynamic state (for a fixed upstream Mach number $M_A = 2.0$ and $M_A = 1.5$, respectively). In both studies, the upstream entropy is fixed ($s_{\mathrm{A}} = s(0.557P_c, 0.964T_c)$) and it corresponds to the inlet entropy of the stator passage shown in Fig. 7.1(a). Different upstream pressures are considered. The range in which the upstream thermodynamic state is allowed to vary corresponds to the thermodynamic region where ORC turbines typically operate. In this regime, see Fig. 7.2, Γ is possibly lower than unity. This implies that the speed of sound decreases upon isentropic compression. Several effects are related to the

condition $\Gamma < 1$, see e.g. Ref. [9, 13, 14] and Cha. 2. These phenomena also affect the shape of the shock polars, as it is shown below.

The first parametric study ($M_A = 2$ and a pressure range $P_A/P_c \in [0.070, 0.557]$ at fixed entropy), is shown in Fig. 7.3(a-d). Fig. 7.3(a) shows the shock angle–deviation polars obtained from the reference EoS implemented in FluidProp (blue lines) and from the PIG model of MDM (red line). For the reference EoS, significant modifications to the shock angle–deviation polar are observed for different values of the upstream pressure. With reference to Fig. 7.2, the range of the selected upstream thermodynamic states is such that Γ_A increases with P_A, thus justifying the departure from the ideal behavior of the shock polars observed in Fig. 7.3(a). Note that for a gas in the ideal regime (red dashed curve) the shock polar depends on the pre-shock Mach number only. Additionally, another significant non-ideal effect is related to the maximum deviation angle that the flow can sustain. As depicted in Fig. 7.3(a), and more in detail in Fig. 7.3(b), the maximum deviation ϑ_{max} can possibly attain much larger values in the non-ideal regime than in dilute conditions. Also, note in Fig. 7.3(b) a non-monotonic dependence of ϑ_{max} on P_A along the selected isentrope.

Fig. 7.3(c) depicts the post-shock Mach number for both the weak and the strong solution, for different flow turning angles and different pressure ratios. As depicted in Fig. 7.3(c), non-ideal effects result in a Mach number increase upon compression, within a limited range of flow turning angles and pressure ratios.

Finally, Fig. 7.3(d) shows the deviation polar of the total pressure ratio, which allows to account for the total pressure loss across the oblique shock wave. Both the weak and strong oblique shock branches exhibit non-monotonic properties in the range of pressures considered. If, for instance, the flow deviation ϑ is fixed, the total pressure loss initially increases with the upstream pressure, but eventually decreases for the largest pressure values considered.

A similar parametric study has been carried out for $M_A = 1.5$ and is shown in Fig. 7.4(a-d). Here, the pressure range $P_A/P_c \in [0.070, 0.696]$ is considered along the reference isentrope. The oblique shock configurations of Fig. 7.4(a-d) show the same trends observed in the previous parametric study for $M_A = 2$. Further computations, performed for different upstream Mach numbers (not shown here), confirm the present findings. Note that there exist a minimum value of the upstream Mach number, namely $M_{A,min} = (1 - \Gamma_{min})^{-1/2}$, where Γ_{min} is the minimum value of the fundamental derivative in the vapor phase, for which the downstream Mach number can increase across oblique shocks of small strength.

Despite the present study is limited to siloxane MDM only, most moderate-to-high molecularly complex fluids exhibit the same qualitative behavior, in accordance with the principle of corresponding states, and therefore the present analysis arguably apply to several different fluids employed in ORC power systems (but not limited to). In particular, the non-ideal features presented in the chapter are admissible within the limits of thermal stability for isopentane and R245fa, closer to the limit for MM, toluene and cyclopentane, while they appear to be slightly above the limit for MDM.

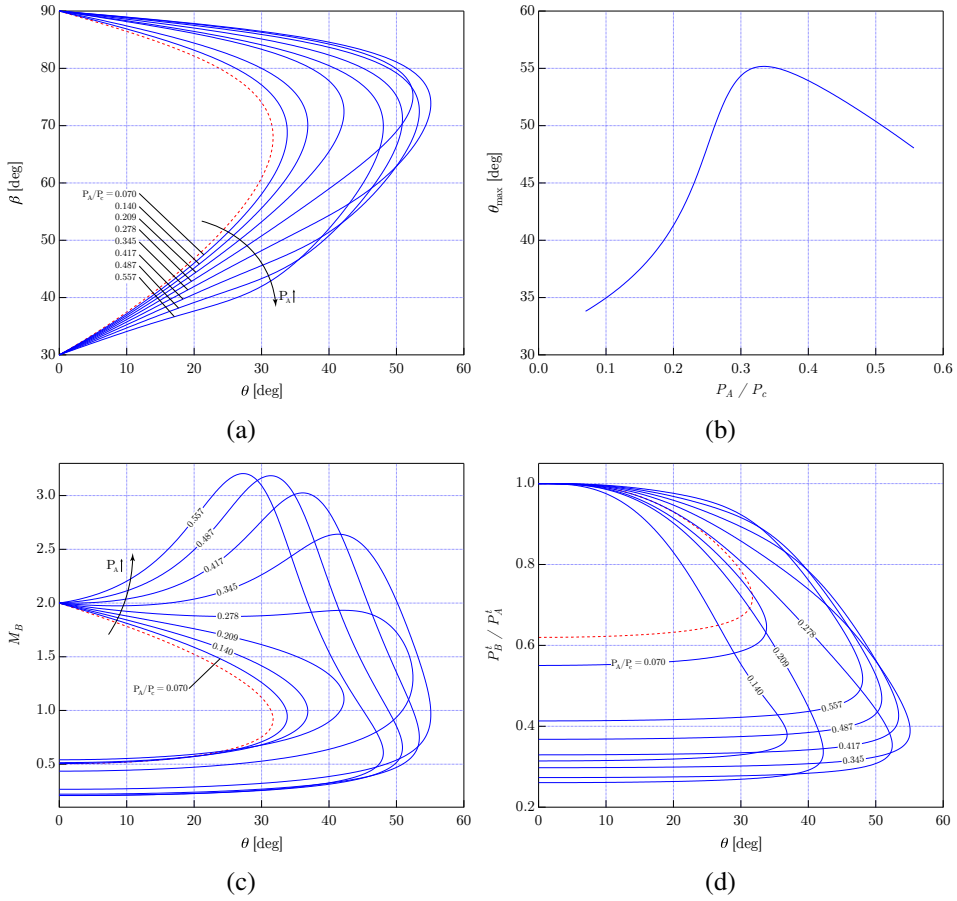

Figure 7.3: shock polars computed using the reference EoS [12] for MDM. $M_A = 2$, $s_A = s(0.557P_c, 0.964T_c)$ and pressure range $P_A/P_c \in [0.070, 0.557]$. Also shown (red dashed line) are the polars obtained from the PIG model; (a) Shock angle–deviation polar; (b) Variation of the maximum deviation angle with the upstream pressure; (c) Mach number–deviation polar; (d) Total pressure ratio–deviation polar;

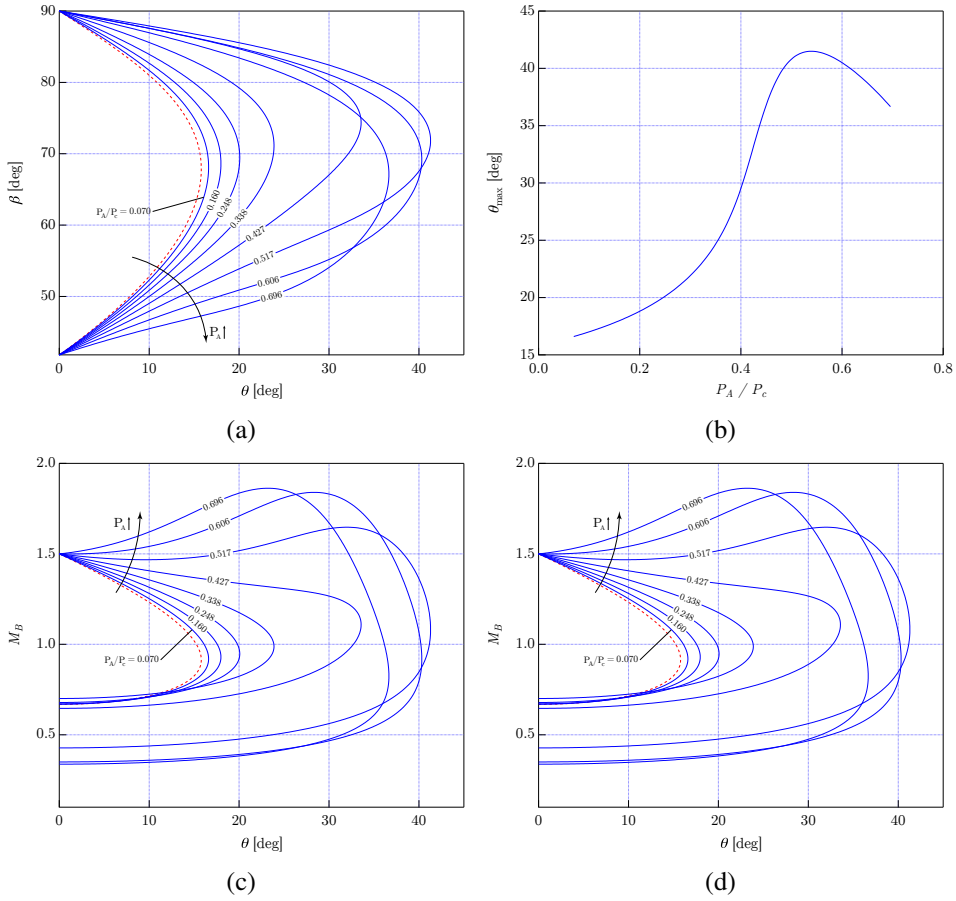

Figure 7.4: shock polars computed using the reference EoS for MDM. $M_A = 1.5$, $s_A = s(0.557P_c, 0.964T_c)$ and pressure range $P_A/P_c \in [0.070, 0.696]$. Also shown (red dashed line) are the polars obtained from the PIG model; (a) Shock angle–deviation polar; (b) Variation of the maximum deviation angle with the upstream pressure; (c) Mach number–deviation polar; (d) Total pressure ratio–deviation polar;

7.3 Fast-response Probe Analysis

Time resolved measurements of fluid properties are fundamental to investigate the complex flow-field that develops in a turbomachinery cascade. Unsteady phenomena, such as vortex shedding or pressure fluctuations related to the wake of rotating blades, play a key role in determining the efficiency of the stage and they possibly result in undesired noise and thermal stresses [15]. Due to the high rotational speed of blade cascades, fast-response probes are required to capture pressure fluctuations within a wide bandwidth which spans from very low frequencies to up to several kHz [16–20].

The development of fast-response pressure probes profited of micro piezo-resistive sensors and flow reconstruction techniques, which allowed to resolve the flow field by means of multiple measurements taken at different times and positions [21]. To enhance the strength of the probe frame, a possible choice is to encapsulate the piezo-resistive sensor within the probe head. This solution guarantees a more robust (in the mechanical sense) device. As a consequence, the encapsulation implies that the time response suffers from a delay due to the dynamics originating from the line-cavity system, which connects the external domain to the piezo-resistive transducer. Since the dynamic of the piezo-resistive transducer is usually much faster than that of the line-cavity system, the geometrical configuration of the capsule and the properties of the fluid have a major influence on the overall time response [22]. Currently, the analytic models to predict the response of such systems rely, in general, on the acoustic wave assumption i.e., they model the response for weak perturbations only. Moreover, analytic models are built on top of the ideal gas assumption whereas ORC power systems employ fluids that exhibit non-ideal features.

The knowledge of the dynamic characteristics of instruments is key to select the tool that suits a particular measurement process best. The bandwidth of the instrument defines the range of frequencies for which the probe returns a reliable output. To establish the maximum frequency that can be captured by a given device, dynamic calibration must be carried out. This crucial step is mandatory since analytic/numerical models are commonly based on a simplified description of the geometry of the probe.

Currently, analytic models are based on mechanical or electrical analogies [23]. They usually describe the line-cavity system as a second-order linear system, providing the value of the resonant frequency and of the non-dimensional damping factor. The system is described as a damped harmonic oscillator where the mass corresponds to the amount of fluid contained in line and the mechanical compliance is related to the compressibility of the fluid within the cavity. Damping is usually modeled via a resistance factor which is retrieved by the analytic solution of the two-dimensional viscous equation for laminar flows [23]. The Hougen model [23] stems from this

hypotheses and it reads:

$$f_{res} = \frac{c}{2\pi(L+\delta)\sqrt{\frac{V}{SL}+\frac{1}{2}}}, \qquad \xi_v = \frac{2\nu}{Sf_{res}}, \tag{7.1}$$

where ρ, c and ν are respectively the density, the speed of sound and the kinematic viscosity of the fluid in the current measurement conditions. In the formulae, L is the length of the line, S is the line cross section, V is the volume of the cavity (see Fig. 7.6(a)). δ is the so-called *end-line* correction [24], a parameter used to take into account the inertia of the fluid within the line. Eq. (7.1) holds under the acoustic assumption i.e., non-linear terms are not considered. However, pressure signals measured by fast-response pressure probes may suffer from significant unforeseen damping if pressure perturbations are not infinitesimal (see e.g. [22]). This could warp the expected dynamic response and could ultimately translate into an incorrect design.

If the pressure field undergoes a step perturbation of intensity ΔP, acoustic waves (or shocks, for larger intensities) propagate through the line into the cavity. Most line-cavity models are derived from the 1D momentum equation integrated over the line, which gives [25]:

$$\frac{d^2P}{dt^2} + \left[\frac{1}{2}\frac{c\Delta M}{(L+2\delta)} + \frac{8\pi\nu}{S}\right]\frac{dP}{dt} + \frac{Sc^2}{(L+2\delta)V}P = \beta P, \tag{7.2}$$

where $\beta = (P+\Delta P)/P$ is a parameter to express the intensity of the initial perturbation. ΔM is the Mach number variation across the wave. In the Hougen model, the damping term reduces to Eq. (7.1). Eq. (7.1) generally provides unrealistically small values of ξ_v, especially if it is used to estimate the damping of a fast-response pressure probes. On the contrary, in Eq. (7.2) the Mach number variation (ΔM) may increase significantly as β increases, determining a larger value of damping due to non-linear terms.

Although inaccurate for shock waves propagation, the line impedance relation $\Delta M = \Delta P/(\rho c^2)$ represents a simple way to define a conservative relation between the Mach number variation and the pressure perturbation entering the line-cavity system, as it provides larger values than those obtained from the Rankine-Hugoniot relations. Therefore, the non-dimensional damping factor related to non-linear convective terms is expected to increase with $\Delta P/(\rho c^2)$.

The considered line-cavity design is reported in Fig. 7.5 and it is employed in all simulations presented hereinafter. The shape of the cavity is properly chosen to be as simple as possible. Moreover, the geometry aims at avoiding flow separation and vortex shedding. The length of the cavity L_C is 1.0 mm, the cavity length to line length ratio is 3.33, the line diameter d to line length ratio is 0.1 and $\theta = 30°$. The line axis is normal to the mean direction of the external flow field i.e., static pressure is measured. Since the flow at the line inlet is always subsonic, a large portion of

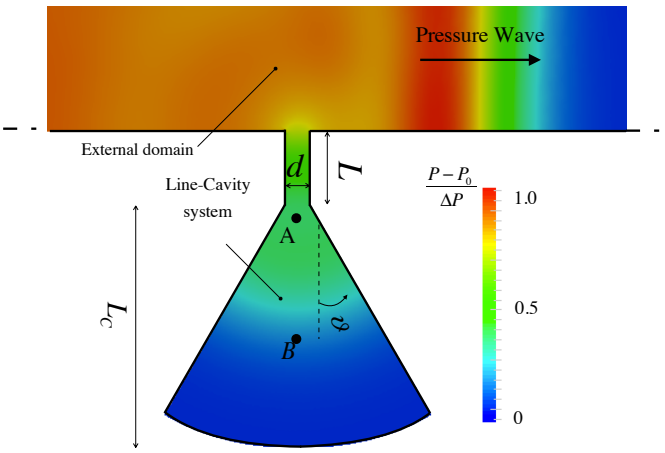

Figure 7.5: line-cavity system investigation. Geometrical sketch of the considered probe design;

the external domain is also included in the computational domain. This allows to provide a full description of the dynamics which now accounts also for effects related to wave propagation in the external domain. Fig. 7.5 reports the unsteady flowfield developing in the considered domain: the pressure wave travels from left to right over the line inlet. This causes pressure perturbations to propagate through the line into cavity, where they reverberate against the probe walls. The pressure signal, measured locally in time at the center of the cavity (point B), will be considered as the quantity of interest in the analysis. The intensity of the incoming pressure wave is represented by the pressure ratio β.

The capabilities of the numerical solver for this set of problems were already assessed in [26], at least for ideal flows of air. As in [26], a two-dimensional approximation of the domain is used. Numerical simulations are carried out under the inviscid fluid assumption. A backward Euler scheme with a dual-time-stepping method is used for the unsteady term while Roe scheme is employed for the computation of the numerical convective fluxes. Sensitivity analyses, not reported here, were carried put considering numerical grids of different resolution and diverse integration time steps. Solutions over a range of significantly different meshes and time steps demonstrate that the selected mesh and integration interval yield grid and time-step independent (or converged) results.

Ideal Flow The step-response to an acoustic perturbation ($\beta = 1.001$) is first reconstructed for air at standard conditions ($P = 1$ bar, $T = 290$ K). A time-step of 0.15 μs is chosen to evolve the solution in time over a numerical grid containing 50000 triangular elements. Figure 7.6(a) reports the output pressure signal, as reconstructed

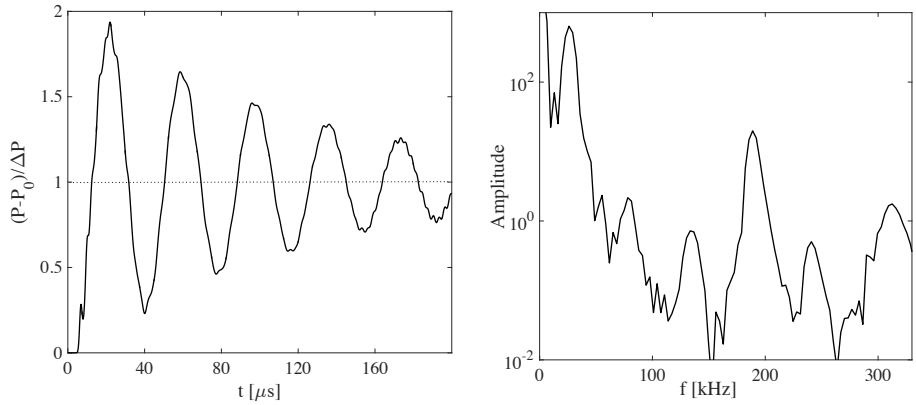

(a) (b)

Figure 7.6: line-cavity system investigation. (a) Non-dimensional step-response considering air and $\beta = 1.001$; (b) Amplitude spectrum for the step-response considering dilute air and $\beta = 1.001$;

in time at point B and scaled by the applied step value. The shape of the predicted time response resembles the one typical of an under-damped second-order system. A second-order identification approach, based on ARX algorithm [27], provides a resonant frequency of 25.7 kHz and a non-dimensional damping factor of 0.055, whereas the analytic expression Eq. (7.1) prescribes a resonant frequency of 30.6 kH and a non-dimensional damping factor due to viscous terms of 0.019. Differences between numerical results and analytic predictions are possibly due to the particular design and setting, as described in [26]. The amplitude spectrum of the step-response is presented in Fig. 7.6(b). A Hamming window is applied and the observation time is 200 μs. The main frequency peak is placed at 25.7 kHz, but the spectrum of the signal is characterized by a high-frequency peak at about 192 kHz, which is believed to be associated to the acoustic wave reverberation within the cavity. These harmonic fluctuations cannot be modeled under second-order approximations. However, the amplitude of these secondary harmonics is one order of magnitude smaller than that of the fundamental frequency. Therefore, the contribution of secondary harmonics on the overall pressure signal is negligible.

The time response is studied now beyond the limit of acoustic waves i.e., for large values of β. Several numerical simulations were performed, for different values of β, considering air at fixed operating conditions. Numerical results provide evidences that the non-linear damping, and therefore the intensity of the initial perturbation, impacts significantly on the system dynamics. For instance, Fig. 7.7(a) presents the non-dimensional step-response of the probe for an increasing value of β ($\beta \sim 1.0$, $\beta = 1.1$, $\beta = 1.2$, $\beta = 1.3$. The pressure is scaled by the intensity of the perturbation. Numerical results reveal that the non-dimensional characteristic frequency slightly

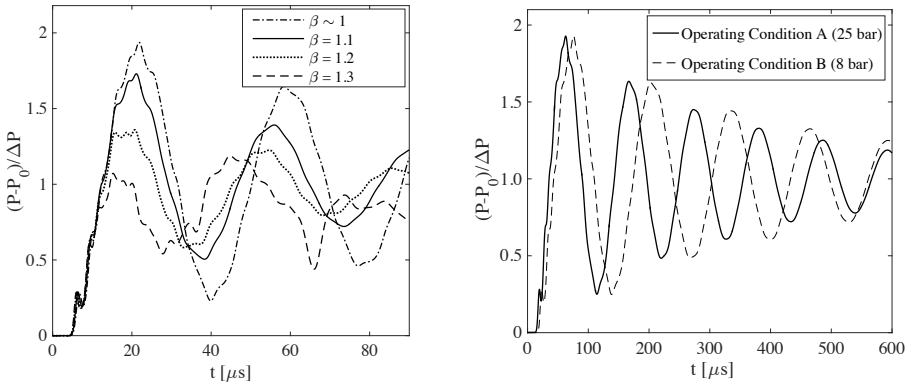

(a) (b)

Figure 7.7: numerical step-response characteristics. (a) Air considering different β; (b) MDM time response $\beta = 1.001$;

increases as β increases, and signal damping increases as well. These effects entail larger rising times i.e., slower probe responses. Second-order identification provides reference values of the non-dimensional damping factor for different β. Numerical results clearly suggest that the damping grows critically as the intensity of the perturbation increases. The time response was reconstructed numerically also for different operating conditions. Although the characteristic frequencies of the output signal change, due to a different value of the speed of sound, the shape of the time response remains similar.

Non-Ideal Flow The response of the line-cavity system is now evaluated considering a MDM vapor at two selected operating conditions *A* and *B*, see Tab. 7.1. *A* corresponds to a thermodynamic state achieved during one of the TROVA experiments while conditions *B* are typically obtained in a ORC stator nozzle, see [28])

According to the PR model, operating conditions *A* and *B* lie respectively in the ideal and non-ideal regime. Since the dynamics of the probe is mainly governed by wave propagation and reflection, non-ideal effects, such as the non-monotone variation of the speed of sound, are expected to play a major role in defining the dynamics of the system.

Fig. 7.7(b) depicts the non-dimensional step-response to a small perturbation ($\beta \sim 1$). The predicted non-dimensional signals are very similar and poorly damped. Fig. 7.8(a) reports the spectral analysis of the signals. Results show that for operating conditions *A* the time response is characterized by higher harmonics. This was expected since the speed of sound is larger, as reported in Tab. 7.1. Second-order identification predicts a natural frequency of $f_{res}^{A} \approx 9.2$ kHz and $f_{res}^{B} \approx 7.6$ kHz. These values fairly agree with analytic predictions from equation Eq. (7.1), which

Exp	P [bar]	T [C]	c [m/s]	Γ	ν [mm^2/s]
A	25	310.3	117.8	3.11	0.186
B	8	270.5	96.7	0.61	0.136

Table 7.1: operating conditions for MDM. The speed of sound values are computed using the PR model;

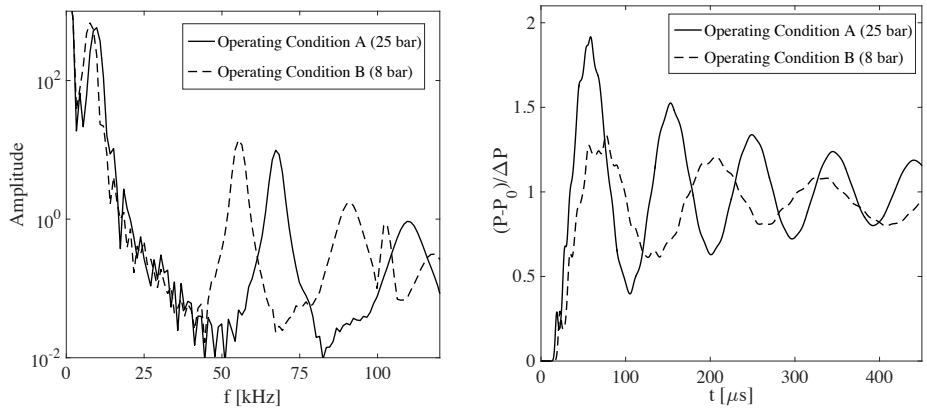

(a) (b)

Figure 7.8: System step response for an MDM vapor. (a) MDM time response amplitude spectrum $\beta = 1.001$; (b) Time response for $\beta = 1.1$;

returns $f^A_{res} \approx 9.9$ kHz and $f^B_{res} \approx 8.5$ kHz. Relative differences between numerical values and analytic predictions are comparable to that registered for dilute air and small perturbation.

Numerical results suggest that thermodynamic non-idealities do not play a significant role within the limit of acoustic perturbations. Indeed, the spectral density comparison of signal A against signal B, reported in Fig. 7.8(a), reveals that the energy is distributed similarly among the harmonics. Indeed, both signals present a steady contribution and a main peak corresponding to the resonant frequency. Secondary peaks are detected at 67 kHz (A) and 56 kHz (B) while tertiary peak are also found at higher frequency. As mentioned earlier, the bias between the corresponding amplitude peaks is due to the different value of the speed of sound. Given that f_{hf} is the high-frequencies peaks, the ratio c/f_{hf} is constant for both operating conditions and for the acoustic response of dilute air. This suggest that the system response to an acoustic perturbation does not depend on the fluid properties.

If larger pressure perturbations are considered a different behavior is predicted. For instance, Fig. 7.8(b) and Fig. 7.9(a) report the non-dimensional signals for $\beta = 1.1$ and $\beta = 1.2$, respectively.

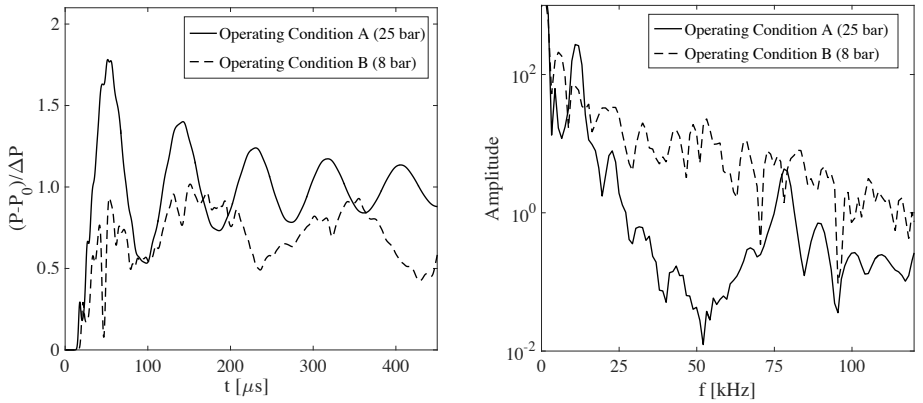

(a) (b)

Figure 7.9: System step response for an MDM vapor. (a) Time response for $\beta = 1.2$; (b) Amplitude spectrum of step response for $\beta = 1.2$;

With particular reference to Fig. 7.8(b), besides the expected differences related to a different value of the speed of sound, numerical results reveal a significant variation of the damping factor. In particular, the response in non-ideal regime (operating condition B) is more damped than that of ideal regime, even though the same perturbation is applied. This difference is even more relevant for a larger value of $\beta = 1.2$, as showed in Fig. 7.9(a). The system response in the non-ideal regime is almost critically damped and it presents dramatic differences if compared to the signal resulting for an ideal fluid. These differences are also observed from the comparison of the spectrum amplitude of pressure signals, reported in Fig. 7.9(b). Within the limit of acoustic waves, the amplitude spectrum was similar for different fluids despite the ideal or the non-ideal regimes. Different behaviors were possibly due to a different value of the speed of sound which is strictly related to the properties of the fluid in its unperturbed conditions. If $\beta = 1.2$, the amplitude spectrum in the non-ideal regime presents a very different trend. There is no clear separation between the main and secondary frequency peaks, but the energy distribution keeps decreasing constantly as the harmonic frequency increases.

A thorough investigation of pressure probe dynamics, considering different geometries, working fluids and operating conditions is mandatory before extending the limits of the results presented in this work.

7.4 VirtuaSchlieren

Current research activities in fluid mechanics integrate theoretical predictions, numerical simulations and experimental measurements to tackle physical problems of

ever increasing complexity. Indeed, in laboratories worldwide CFD simulations are often used to guide experimental activities and to complement the actual measurements. Unfortunately, the comparison of CFD against experimental results is not always a straightforward task. Measurement procedures may possibly deliver a representation of the flow field that is not as detailed as CFD ones and measured quantities are often not immediately related to flow variables such as density, pressure and velocity. In these cases, complex and/or time consuming algorithms are to be applied to numerical results for comparing simulations and experiments.

A good example is the post-processing of numerical simulations of fluid flows for comparison against measurements obtained from an experimental technique called schlieren visualization.

Schlieren is a German word used to indicate optical non-homogeneities. In fluid mechanics, the word schlieren is commonly associated to optical techniques for capturing the density variation along a specified direction. This method is applicable to fluid flows embedding regions of variable density, such as, for instance, supersonic flows or liquid/gas mixtures. The advantage of this technique lies in its simplicity and in the fact that it is non-intrusive—only optical access is to be guaranteed and no seeding of the flow is required. The schlieren technique is widely used in many different fields from automotive [29] to medical research [30] or from fundamental physics [31] to micro-fluidics [32].

In a standard schlieren apparatus a collimated light beam is cast through the test chamber. The apparatus usually includes a set of mirrors and optical lens used to drive the light from the source, which is assumed to be point-wise, across the domain. A shutter, called *knife*, is placed at the focal point of the light beam to isolate rays that were deflected by non-homogeneities in the continuum. In this way, only a fraction of the initial light beams eventually reach the screen, where the schlieren image is projected. The schlieren image is therefore a two-dimensional picture of the three-dimensional flow domain. The image is characterized by darker and brighter regions whose intensity depends on the sign of density variations encountered by light rays while crossing the continuum. The orientation of the knife determines the components of the density gradient the measurement system is sensitive to. Several experimental techniques were derived from Schlieren such as, for instance, the Background Oriented Schlieren BoS [33], the Laser Schlieren Deflectometry LSD [34] or Moire deflectometry [35].

In the following, results from the the *VirtuaSchlieren* software, that was developed during this thesis, are presented. The VirtuaShlieren code is a hybrid GPU/CPU-based schlieren simulation tool for obtaining schlieren images from three-dimensional CFD simulations of variable density flows, including non-ideal fluid flows. The algorithm moves from the work of [36, 37] and it is capable of accounting for diverse experimental arrangements such as the single pass or the double-pass reflected schlieren apparatuses. Further details about the software, the algorithms implemented and about the test cases presented here can be found in [38].

Briefly, to obtain the virtual schlieren image from CFD simulations of the flow field, a large number of light paths is computed starting from the light source and across the computational domain. The ray trajectories and their light intensity are influenced by the local value of the fluid refraction index, which is computed from the interpolated value of the density within the computational cell. Once the ray paths are reconstructed and the intensity of the light computed, the virtual schlieren is reconstructed on the screen plane. The virtuaSchlieren code takes advantage or fast search algorithms, such as a standard kd-tree approach (implemented in the open-source ANN library) and the PoliTree algorithm (see [38]), to hasten the ray tracing process. Virtual schlieren images may be compared against the experimental one to assess the accuracy of the mathematical fluid model and to determine specific properties of the fluid. Imaging science offers a wide set of different image processing methods that could accomplish this goal, among the others it is worth mentioning statistical methods such as those based on convolution and cross-correlation, see for instance [39] or those derived from the Keypoint Matching approach [40].

NICFD flow fields, such those reported in [41], can be studied thank to a general formulation of the density-refraction index relation based on the Lorentz-Lorenz model, see [42]. Some exemplary results for compressible flows, including smooth variation of the density as well as shock waves, are presented in this section. Further details about the code and its implementation can be found in [38]. The NICFD solver included in the SU2 suite is used in all computations, to obtain the flow-field.

Axisymmetric body in supersonic flow An experimental test case is reproduced numerically and the predicted schlieren images are compared against actual experimental pictures. The domain consists of a small rectangular supersonic wind tunnel. The domain has an optical access on both sides so that a single passing schlieren can be used. An axisymmetric body, namely a cone-shaped bow that merges into a cylindrical rear segment, is placed along the channel axis. The fluid is air in dilute conditions and the flow is parallel to the cylinder axis x. The upstream Mach number is equal to 2 and the inflow conditions correspond to a static pressure $\mathrm{P}_s = 1$ bar and temperature $\mathrm{T}_s = 300$ K. Fig. 7.10(a) and Fig. 7.10(b) briefly report geometrical data and the set up of the experimental apparatus. A detailed description of the test-rig set up and a complete discussion about results can be found in [33]. Domain symmetries were exploited to reduce the dimension of the problem in CFD simulations: only a 90° sector of the body was considered. The unstructured computational grid is composed by approximately 7 million tetrahedral elements, see Fig. 7.11(a). The inviscid flow field is solved using an implicit second order accurate scheme of Roe type with no limiting function. The schemes employs a weighted least square method to reconstruct the spatial gradients at cell interfaces. A Multigrid approach is exploited, to accelerate the convergence of the numerical simulation. Fig. 7.11(b) reports the density field computed using SU2. The cone-shaped shock wave generated at the tip of the body is correctly reproduced, as well as the rarefaction fan developing at the

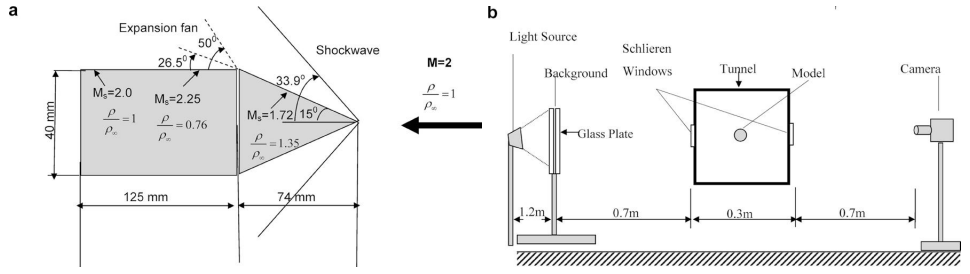

(a) (b)

Figure 7.10: (a) Picture reports geometrical data of the cone-shaped body and depicts main features of the analytic solution [33]; (b) Pictorial representation of the test rig used to investigate the flow field around the supersonic body [33];

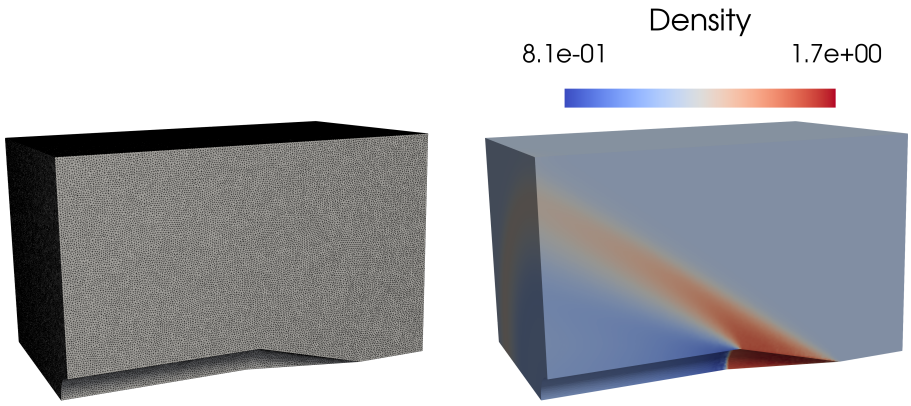

(a) (b)

Figure 7.11: Picture reports the numerical grid employed to simulate the axisymmetric body in supersonic flow; (b) Picture reports the density field around the cone-shaped body;

junction of the nose solid cone with the aft cylindrical part of the body.

Fig. 7.13(a) reports the experimental schlieren image to be compared against Fig. 7.12(a) and Fig. 7.12(b), showing the numerical schlieren images produced using two different fast searching algorithms (the ANN and the PoliTree algorithms, see [38]).

Though a proper approach to quantify the light intensity difference between the experimental and the numerical image is still under development, the predicted schlieren image fairly compare to the experimental one. The conical shock-wave and the rarefaction fan are correctly reproduced in terms of light gradients and wave angles, thus confirming the correctness of the present approach. The ANN and the PoliTree fast search algorithm produce very similar results: no significant differences are notable between Fig. 7.12(a) and Fig. 7.12(b). A more quantitative comparison is shown

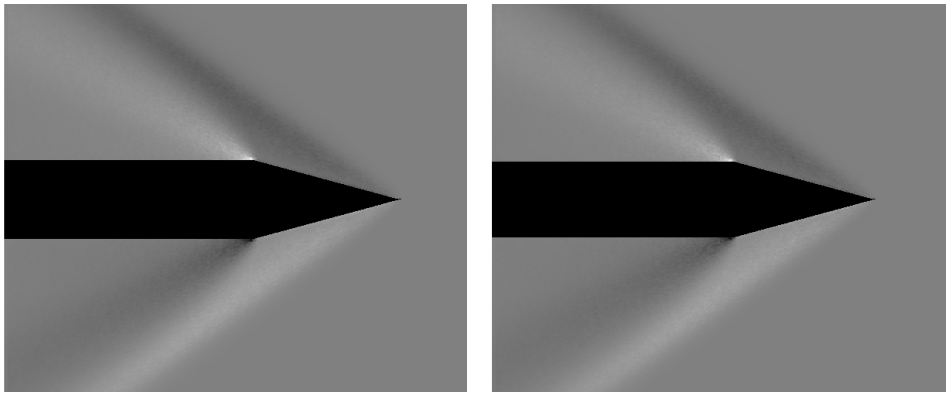

(a) (b)

Figure 7.12: (a) Virtual image predicted for the supersonic cone-shaped body, using the ANN library; (b) Virtual image predicted for the supersonic cone-shaped body, using the PoliTree algorithm;

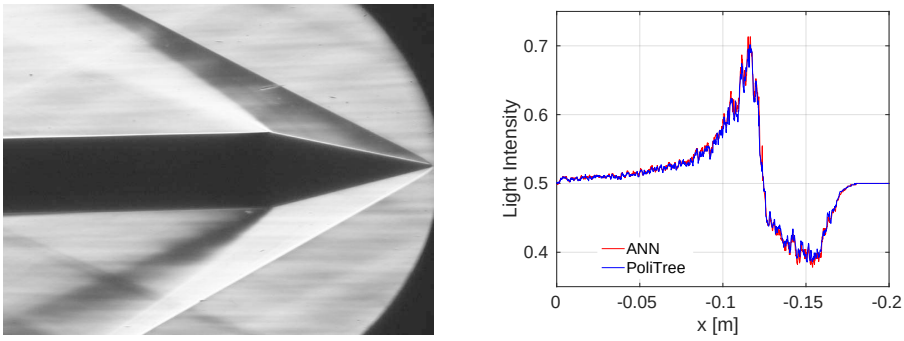

(a) (b)

Figure 7.13: (a) Experimental schlieren image of the density field around a cone-shaped body within a supersonic flow [33]; (b) supersonic body. Comparison of light intensity trends extracted from the numerical schlieren image predicted exploiting the ANN and the PoliTree search algorithm;

in Fig. 7.13(b), where the light intensity values obtained by the two approaches are compared along a straight line located on the *x*-*y* plane 0.024 m above the axis of symmetry. Only negligible differences are observed in Fig. 7.13(b) between the two approaches.

Non-ideal Compressile Fluid flow This test case regards the isentropic expansion of a fluid at non-ideal conditions. The inviscid supersonic flow of a generic fluid over an expansion edge is simulated. The thermodynamics is modeled through the vdW EoS. The fluid is defined by a specific heat ration γ of 1.0173 and a gas constant

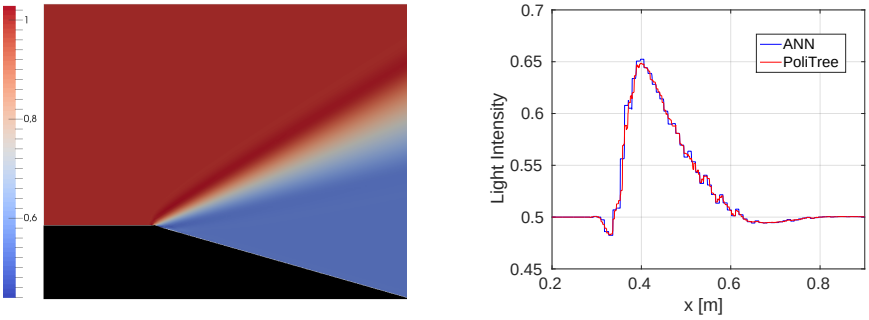

(a) (b)

Figure 7.14: (a) Computed density field for the non-ideal supersonic expansion test case. The field is scaled using the value ρ_0; (b) Non-ideal expansion: comparison of light intensity trends extracted from the numerical schlieren image predicted using the ANN and the PoliTree search algorithm;

$R = 26.04$ J/KgK. Inflow conditions, identified by subscript 0 hereinafter, correspond to a static pressure P_0 of 1 bar and a static density $\rho_0 = 85.6$ Kg/m^3 and are well within the non-ideal thermodynamic region.

The domain length in the (x) or flow direction is 1, the height (y) is 0.8 and the thickness (z) is 0.3 unit length. The flow is turned by an angle $\theta = 15.95°$ over the edge. With reference to Fig. 7.14(a), the inlet boundary is on the left hand side while the outlet boundary is on the right. Slip-wall condition holds on all the remaining boundaries. The numerical grid is made of 363,558 hexahedral elements (380,800 nodes).. A second order implicit HLLC (Harten-Lax-van Leer-Contact) scheme [43] was employed to reconstruct the spatial convective fluxes using a weighted least square approach. A Multigrid strategy was again employes, to hasten the convergence ot the simulation. Fig. 7.14(a) reports the density field, scaled by the upstream value of density, computed using the SU2 NICFD solver. An expansion fan centered at the expansion corner is clearly visible and it separates the upstream (0) region from the downstream one.

Fig. 7.15(a-b) shows respectively the schlieren image obtained using the ANN library and using the PoliTree library. 4 millions light rays were used to produce the schlieren image on the screen. Fig. 7.14(b) depicts light intensity trends along a line crossing the domain at $y = 0.25$. Despite its lower precision in determining the position of the nearest neighbor, the PoliTree simplified search is proved to deliver results comparable to those obtained from the ANN library.

(a) (b)

Figure 7.15: virtual schlieren images predicted using the VirtuaSchlieren tool. (a) Image obtained using the ANN library (b) Image obtained using the PoliTree algorithm;

7.5 Non-Ideal Supersonic Flows Around a Diamond-Shaped Airfoil

The VirtuaSchlieren software is now used to generate the expected schlieren image of the TROVA experiment involving the non-ideal supersonic flow around a diamond-shaped airfoil. Namely, the test case reproduced here corresponds to the one presented in Sec. 5.4.2. The diamond is placed at a neutral angle of attack and it has a semiangle equal to 7.5° at the leading edge and 10° at the trailing edge, further details may be found in Sec. 5.4.2 and in Ref. [44]. To reduce the computational burden, only the region of the test section including the diamond is reproduced numerically i.e., the portion of the domain corresponding to the nozzle is not modeled. Fig.7.16(a) reports the two-dimensional grid used to compute the numerical solution of the flowfield using the Reynolds-Averaged Navier-Stokes (RANS) model. No mesh adaptation strategy is used in this case. Therefore, the numerical grid has a very fine resolution, to catch the strong gradients due to the presence of shock-waves with a sufficient level of accuracy. An implicit second-order accurate MUSCL scheme of Roe type was employed together with a flux limiting function (Venkatakrishnan flux limiter). The Green-Gauss formulae was used to reconstruct gradients at cell interfaces. The Menter Shear Stress Transport [45] closure model was employed. The boundary layer is resolved up to the wall distance scale $y^+ = 1$ (corresponding to $\approx 1e^{-6}$ m). Fig.7.16(b) reports the flowfiels computed using the PR EoS to model thermodynamics. The applied inflow conditions correspond to the state of the fluid ahead of the diamond retrieved from the simulation reported in Sec. 5.4.2. Namely, inflow conditions correspond to a static pressure $P^s = 271072$ Pa and temperature $T^s = 533.22$ K, with a flow Mach number of 1.52. Once the two dimensional flowfield is computed, the solution is projected onto a three dimensional extruded mesh, in order to be able to the apply ray tracing algorithm. Note that, even if the flowfield

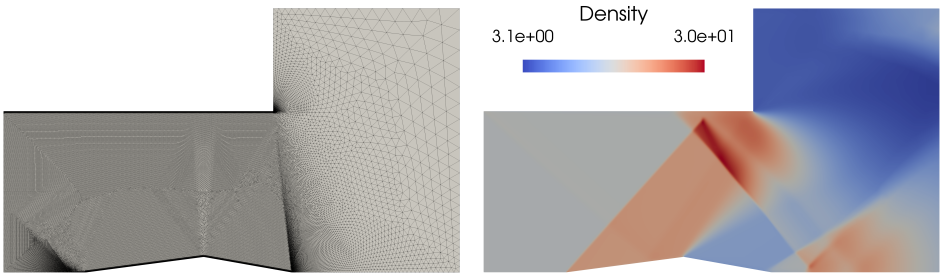

(a) (b)

Figure 7.16: non-ideal supersonic flow around a diamond-shaped airfoil. (a) Numerical hybrid unstructured grid used to carry out RANS simulations; (b) Density flowfield as computed from the SU2 non-ideal computaitonal fluid dynamics solver;

is still two dimensional, because no dependency on the extrusion direction applies, the ray tracing problem is instead three-dimensional. Indeed, the light particles have an initial trajectory which is normal to the plane of the solution but, as they advance into the extruded field, they are diverted according to the fluid density gradients they encounter. Fig. 7.17 reports the comparison between the experimental and the numerical schlieren image. The VirtuaSchlieren software is able to generate an image which fairly resembles the experimental one. In the experiment, the orientation of the knife edge is such to visualize density gradients in the streamwise direction. This means that the knife is rotated so that darker gray levels are associated to positive density gradients (compressions) and lighter gray levels to negative ones (expansions). Indeed, the leading edge shock and its reflection against the test section wall are correctly reproduced as dark lines. Note that in the experimental schlieren image (upper side of Fig. 7.17) both positive and negative density gradients correspond to region of low light intensity. According to [46], this unexpected result is due to the specific configuration of the schlieren apparatus, see [47]. Briefly, density gradients in the test section are so strong that they are deviated outside the measuring range, thus they do not reach the camera sensor. For this reason, both positive and negative density gradients result in dark flow regions in the experimental snapshot. Since the VirtualShlieren just computes the light intensity variation according to the light ray absolute deviation, and it doesn't account for the specific test-rig configuration, the numerical image correctly represents compressive gradients as dark regions and rarefaction gradients as bright regions. The synthetic image is characterized by a higher resolution which is possibly related to the two-dimensional character of the fluid dynamics solution. Indeed, the experimental image contains a few blurred regions, like for instance in the proximity of the leading shock reflection point or the airfoil trailing edge. This effect may be possibly due to three-dimensional effects related to the interaction of the boundary layer, developing on the front and back walls, with shock waves.

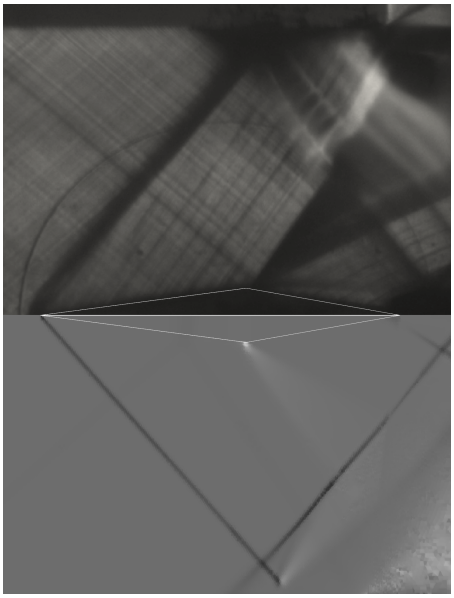

Figure 7.17: comparison of the experimental (upper side) and virtual schlieren images. The VirtuaSchlieren is able to produce an expected schlieren image which fairly matches reality;

7.6 Conclusions

In the chapter, several exemplary fluid-dynamics problems involving non-ideal flows were described. In the first part, a numerical investigation of non-ideal effects across oblique shock waves was provided. These non-ideal effects are of utmost relevance to ORC applications, since shocks generated at the trailing edge of supersonic stator blades largely affect the overall stage performances. In this respect, the understanding of the main parameters of influence on the characteristic shock wave pattern is key to improve the correct estimation of losses. Differently than the perfect gas case, the upstream thermodynamic state play a major role in determining the variation of relevant properties across the shock. In particular, these include the maximum flow deflection angle, the Mach number variation and the total pressure loss across the shock. Additionally, in the acoustic limit the variation of the shock angle and of the downstream Mach number with the flow deflection ultimately depend on the upstream value of the fundamental derivative of gasdynamics.

In the second part of the chapter, the step-response of a line-cavity system to non-acoustic pressure perturbations was assessed. The analysis includes the non-ideal regime of interest for ORC applications. The pertinent technology is fast-response pressure probes for pressure measurements past the turbine rotor. First, the role of non-linear terms has been assessed through several numerical simulations, involving dilute air, to investigate how the system responds to diverse perturbation intensities.

Indeed, the Hougen model predicts a constant damping factor while numerical results show that the damping factor instead increases as the pressure perturbation intensity increases. Numerical results suggest that the time response of pressure probes operating with flows that obey the perfect gas law is strictly related to the intensity of the perturbation. At the same time, numerical results suggest that non-idealities do not play a significant role within the limit of acoustic perturbations. When the acoustic perturbation assumption is relaxed, non-idealities are found to introduce even higher levels of damping.

Eventually, the *VirtuaSchlieren* software was used to post-process the CFD solution, provided by the SU2 solver, in order to obtain virtual schlieren images of the test domain. Numerical results compare fairly well to experimental Schlieren images. These are relative to both an ideal test case, a conical body plunged in a supersonic stream, and a non-ideal flow, the supersonic flow around a diamond-shaped airfoil which is one of the experiment carried out in the TROVA test-rig.

References

[1] B. Saracoglu, G. Paniagua, J. Sanchez, and P. Rambaud. "Effects of blunt trailing edge flow discharge in supersonic regime". In: *Computers & Fluids* 88 (2013), pp. 200–209.

[2] J. Denton and L. Xu. "The trailing edge loss of transonic turbine blades". In: *ASME 1989 International Gas Turbine and Aeroengine Congress and Exposition*. 1989.

[3] D. Mee, N. Baines, M. Oldfield, and T. Dickens. "An examination of the contributions to loss on a transonic turbine blade in cascade". In: *ASME 1990 International Gas Turbine and Aeroengine Congress and Exposition*. 1990.

[4] P. Colonna, J. Harinck, S. Rebay, and A. Guardone. "Real-gas effects in Organic Rankine Cycle turbine nozzles". In: *J. Propul. Power* 24.2 (2008), pp. 282–294.

[5] M. Pini, G. Persico, D. Pasquale, and S. Rebay. "Adjoint method for shape optimization in real-gas flow applications". In: *Journal of Engineering for Gas Turbines and Power* 137.3 (2015).

[6] F. J. D. Galiana, A. P. S. Wheeler, J. Ong, and C. A. M. Ventura. "The effect of dense gas dynamics on loss in ORC transonic turbines". In: *Journal of Physics: Conference Series* 821.1 (2017), p. 012021.

[7] F. J. D. Galiana, A. P. Wheeler, and J. Ong. "A study of trailing-edge losses in organic Rankine cycle turbines". In: *Journal of Turbomachinery* 138.12 (2016), p. 121003.

[8] F. D. Galiana, A. Wheeler, J. Ong, and C. de M Ventura. "The effect of dense gas dynamics on loss in ORC transonic turbines". In: *Journal of Physics: Conference Series*. Vol. 821. 1. IOP Publishing. 2017, p. 012021.

[9] P. A. Thompson. "A fundamental derivative in gasdynamics". In: *Phys. Fluids* 14.9 (1971), pp. 1843–1849.

[10] G. Gori, D. Vimercati, and A. Guardone. "Non-ideal compressible-fluid effects in oblique shock waves". In: *Journal of Physics: Conference Series* 821.1 (2017), p. 012003. URL: `http://stacks.iop.org/1742-6596/821/i=1/a=012003`.

[11] D. Vimercati, G. Gori, and A. Guardone. "Non-ideal oblique shock waves". In: *Journal of Fluid Mechanics* 847 (2018), pp. 266–285. DOI: `10.1017/jfm.2018.328`.

[12] E. W. Lemmon, M. L. Huber, and M. O. McLinden. "NIST reference database 23: reference fluid thermodynamic and transport properties–REFPROP, version 9.1". In: *Standard Reference Data Program* (2013).

[13] M. S. Cramer and A. Kluwick. "On the Propagation of Waves Exhibiting Both Positive and Negative Nonlinearity". In: *J. Fluid Mech.* 142 (1984), pp. 9–37.

[14] M. S. Cramer and L. M. Best. "Steady, isentropic flows of dense gases". In: *Phys. Fluids A* 3.4 (1991), pp. 219–226.

[15] O. P. Sharma, G. F. Pickett, and R. H. Ni. "Assesment of unsteady flows in turbomachinery". In: *ASME J. Turbomachinery* 114 (1992), pp. 79–90.

[16] R. J. Miller, R. W. Moss, R. W. Ainsworth, and C. K. Horwood. "Time-resolved vane-rotor interaction in a high-pressure turbine stage". In: *ASME J. Turbomachinery* 125 (2003), pp. 1–13.

[17] J. Schlienger, A. I. Kalfas, and R. S. Abhari. "Vortex-wake-blade interaction in a shrouded axial turbine". In: *ASME Turbo Expo Conference*. Wien, 2004.

[18] P. Gaetani, G. Persico, V. Dossena, and C. Osnaghi. "Investigation of the Flow Field in a High-Pressure Turbine Stage for Two Stator-Rotor Axial Gaps-Part II: Unsteady Flow Field". In: *ASME J. Turbomachinery* 129 (2007), pp. 580–590.

[19] L. Porreca, A. I. Kalfas, and R. S. Abhari. “Aero-thermal Analysis of Partially Shrouded Turbine Blades”. In: *J. Propulsion and Power* 25 (2009).

[20] G. Persico, P. Gaetani, and C. Osnaghi. “A parametric study of the blade row interaction in a high pressure turbine stage”. In: *ASME J. Turbomachinery* 131 (2009).

[21] J. F. Brouckaert. “Fast Response Aerodynamic Probes for Measurements in Turbomachines”. In: *J. of Power and Energy* 126 (2007).

[22] G. Persico, P. Gaetani, and A. Guardone. “Design and analysis of new concept fast-response pressure probes”. In: *Meas. Sci. Technol.* 16 (2005), pp. 1741–1750.

[23] J. O. Hougen, O. R. Martin, and R. A. Walsh. “Dynamics of pneumatic transmission lines”. In: *Contr. Eng.* (1963).

[24] E. O. Doebelin. *Measurement systems: application and design*. McGraw-Hill, 1990.

[25] J. P. M. Trusler. *Physical Acoustics and Metrology of Fluids*. The Adam Hilger Series on Measurement Science and Technology. Bristol, England: Adam Hilger (IOP Publishing Ltd.), 1991.

[26] G. Gori, P. Molesini, G. Persico, and A. Guardone. “Non-Ideal Compressible-Fluid Dynamics on Fast-Response Pressure Probes for Unsteady Flow Measurements in Turbomachinery”. In: *Journal of Physics Conference Series* 821 (Mar. 2017).

[27] L. Lijung. *System Identification – Theory for the User*. 2nd. Upper Saddle River, NJ: Prentice Hall, 1999.

[28] P. Colonna, S. Rebay, J. Harinck, and A. Guardone. “Real-gas effects in ORC turbine flow simulations: influence of thermodynamic models on flow fields and performance parameters”. In: *ECCOMAS CFD 2006*. Egmond aan Zee, NL, 2006.

[29] J. Lee, N. Kim, and K. Min. “Measurement of spray characteristics using the background-oriented schlieren technique”. In: *Measurement Science and Technology* 24.2 (2012).

[30] J. Tang, T. Liebner, B. Craven, and G. Settles. “A schlieren optical study of the human cough with and without wearing masks for aerosol infection control”. In: *Journal of the Royal Society Interface* 6 (2009), pp. 727–736.

[31] K. Hirano, C. Matsumoto, K. Shimoda, and T. Yamamoto. “Cross Check of Electron Density Distribution by Moiré-Schlieren Technique and Mach-Zehnder Interferometry”. In: *Japanese Journal of Applied Physics* 24.11 (1985), pp. 1518–1521.

[32] C. Huang, J. Gregory, and J. Sullivan. “A modified schlieren technique for micro flow visualization”. In: *Measurement Science and Technology* 18.5 (2007).

[33] L. Venkatakrishnan and G. Meier. “Density measurements using the Background Oriented Schlieren technique”. In: *Experiments in Fluids* 37.2 (2004), pp. 237–247.

[34] J. Schäfer, R. Foest, T. Kewitz, J. Šperka, and K. Weltmann. “Laser Schlieren deflectometry for temperature analysis of filamentary non-thermal atmoshperic pressure plasma”. In: *Review of Scientific Instruments* 83 (2012).

[35] O. Kafri and I. Glatt. “Moire deflectometry: a ray deflection approach to optical testing”. In: *Opt. Eng.* 24.6 (1985).

[36] L. Yates. “Images Constructed from Computed Flowfields”. In: *AIAA Paper 92-4030* 17th AIAA Aerospace Ground Testing Conference (1992).

[37] C. Brownlee, V. Pegoraro, S. Shankar, P. McCormick, and C. Hansen. “Physically-based interactive flow visualization based on Schlieren and interferometry experimental techniques”. In: *IEEE Transactions on Visualization and Computer Graphics* 17.11 (2011).

[38] G. Gori and A. Guardone. "VirtuaSchlieren: A hybrid GPU/CPU-based schlieren simulator for ideal and non-ideal compressible-fluid flows". In: *Applied Mathematics and Computation* 319 (2018). Recent Advances in Computing, pp. 647–661. ISSN: 0096-3003. DOI: https://doi.org/10.1016/j.amc.2017.07.041. URL: http://www.sciencedirect.com/science/article/pii/S0096300317305027.

[39] T. Keating, P. Wolf, and F. Scarpace. "An improved method of digital image correlation". In: *Photogrammetric Engineering and Remote Sensing* 41.8 (1975).

[40] D. Lowe. "Object recognition from local scale-invariant features". In: *Computer vision, 1999. The proceedings of the seventh IEEE international conference on*. Vol. 2. Ieee. 1999, pp. 1150–1157.

[41] A. Spinelli, F. Cozzi, M. Zocca, P. Gaetani, V. Dossena, and A. Guardone. "Experimental Investigation of a Non-Ideal Expansion Flow of Siloxane Vapor MDM". In: *Proceedings of the ASME 2016 Turbo Expo, Soul*. GT2016-57357. 2016.

[42] Y. Liu and H. Daum. "Relationship of refractive index to mass density and self-consistency of mixing rules for multiocomponent mixtures like ambient aerosols". In: *J. of Aerosol Science* 39 (2008), pp. 974–986.

[43] W. S. E.F. Toro M. Spruce. "Restoration of the contact surface in the HLL-Riemann solver". In: *Shock Waves* (1994).

[44] A. Guardone, M. Zocca, G. Cammi, and A. Spinelli. "Oblique waves in the non-ideal compressible-fluid regime". 2017.

[45] F. Menter. "Zonal Two Equation $k-\omega$, Turbulence Models for Aerodynamic Flows". In: *AIAA Paper* 93-2906 (1993).

[46] C. C. Conti. "Non-ideal flows of organic vapors : an experimental investigation for applications in organic Rankine cycle turbines". MA thesis. Italy: Politecnico di Milano, 2017.

[47] F. Cozzi, A. Spinelli, M. Carmine, R. Cheli, M. Zocca, and A. Guardone. "Evidence of complex flow structures in a converging-diverging nozzle caused by a recessed step at the nozzle throat". In: *J. Chem. Eng*. 2016.

CHAPTER 8

CONCLUSIONS AND OUTLOOK

The present doctoral dissertation covered many diverse topics related to Non-Ideal Compressible-Fluid Dynamics (NICFD). NICFD is a quite novel research field devoted to the investigation of flows of fluids that do not abide by the ideal gas law. The characterization of non-ideal compressible-fluid flows is of the utmost relevance to applications involving complex fluids in the single vapor phase, at conditions close to the saturation curve and near the critical point. This typically occur in Organic Rankine Cycle machineries (ORC), supercritical CO_2 power systems, turbogenerators, refrigerators and many others industrial applications.

The advancements reported in the dissertation regards theoretical, numerical and experimental aspects related to the NICFD research field.

Advancements in NICFD physics. Under the theoretical perspective, the findings reported in the thesis reveal the existence of a unprecedented non-ideal effect. Namely, if the state of the fluid is located within the non-ideal thermodynamic region, where $\Gamma < 1$, an overall Mach number increase upon flow compression across steady oblique shock waves was predicted. This non-ideal phenomenon was formalized through theoretical developments following the conservation laws for inviscid and adiabatic flows. Moreover, it was shown how the effect is strictly related to the regime of the flow. It was shown also that, in a non-ideal regime, the flow maximum turning angle and the shock wave slope, w.r.t. the upstream flow direction, strictly depend on the whole pre-shock state. This oppose the physics ruling out dilute gas flows, for which the variation of fluid properties across the shock solely depend on the pre-shock Mach number value. Theoretical predictions presented in this work are confirmed by numerical experiments. Exemplary computations were performed using state-of-the-art fluid models. The non-ideal Mach number increase was predicted considering diverse compounds of interest for industrial applications. For siloxane

MDM, a post-shock Mach number increase, up to 1.5 times the pre-shock value, was discovered. The experimental verification of the occurrence of non-ideal shock waves can be devised in test rigs working with fluids of high to moderate molecular complexity and it is currently under investigation at the CREA Lab (Compressible fluid dynamics for Renewable Energy Applications laboratory) at Politecnico di Milano. The investigation of the non-ideal oblique shocks finds its purpose in applications where waves are either intentionally formed (e.g. intake ramps and rockets) or they are present within the flow as a byproduct of the supersonic flow expansion (e.g. fish-tail shocks in turbine nozzle vanes, over/under-expanded jet from nozzle exit). A thorough understanding of the physics underlying non-ideal oblique shocks is essential to improve the performances of devices exploiting complex compounds as working fluid. For instance, in a typical turbine stage, the stator is used to accelerate the fluid and to add swirl to the flow. In other words, a set of static guide vanes are designed to produce a high speed flow optimally directed towards the next row of movable turbine blades, the rotor. Typically, a fish-tail shock arises at the blade trailing edge and the flow downstream the stator utterly depends on the characteristics of this structure. Therefore, to optimally redirect the flow past the stator in ORC cascades, the design process should account for the findings presented in this dissertation.

Advancements in NICFD numerics. The dissertation addressed also the development of numerical tools suitable for the simulation of complex fluid flows in the non-ideal regime. Namely, the SU2 open-source suite was largely redesigned to accommodate state-of-the-art fluid models. A limited set of different equations of state is now included in an embedded thermodynamic library while additional ones are available through a dedicated interface which provides access to the FluidProp library. The steps undertaken to extend the SU2 solver to NICFD flows were described throughout the dissertation. Particular attention was pledged to presenting the modifications required to generalize the standard approximate Riemann solver. Eventually, the implementation of the non-ideal solver was verified exploiting analytic test problems regarding flows of fluids in the non-ideal regime. Grid sensitivity analyses were carried out, to assess the influence of the spatial discretization on the computed solution and to quantify the error related to grid spacing. Furthermore, for the first time the thermodynamic models implemented in a NICFD solver were assessed against experimental data from dynamic test cases. The non-ideal solver was assessed for a set of exemplary flow configurations of relevant interest for practical applications. The experiments were realized using the Test-Rig for Organic VApours (TROVA) at Politecnico di Milano. The comparison of numerical prediction against experimental data was complemented with an uncertainty quantification analysis. The uncertainty affecting the test-rig operating conditions were forward propagated through the NICFD solver and the sensitivity of the numerical solution, w.r.t. the input variability, was evaluated. The assessment reveals that all the considered non-ideal flows are

fairly well simulated by the solver and that the variability of the quantities of interest is limited to very small values. Evidences regarding the reliability of the numerical implementation and the predictiveness of the solver are provided.

Moreover, the *VirtuaSchlieren* software is presented in the dissertation. The software is a hybrid GPU/CPU-based schlieren simulation tool for obtaining virtual schlieren images from three dimensional CFD simulations of variable density flows, including non-ideal fluid flows. Results presented in this dissertation show a good qualitative agreement between numerics and experiments. Though there is still plenty to be discovered, in particular regarding the modelisation of the refracting index for complex compounds and its dependence on the flow regime, the VirtuaSchlieren provides an additional means to compare measurements and numerical predictions. In this perspective, future work may foresee the application of image matching techniques to obtain a quantitative comparison between the experimental and the virtual schlieren images.

Advancements in NICFD experiments. The dynamics of pressure probes for high frequency measurements was investigated numerically considering fluids in a non-ideal regime. These devices, which can be modeled as a line-cavity system, are typically employed to measure pressure fluctuations past turbine rotors. The probe time-response to pressure perturbations was reconstructed and the effects of non-idealities were assessed. The role of non-linear terms, generally neglected by analytic models, was also assessed. The Hougen model, which is based on the acoustic perturbation assumption, predicts a constant value for the damping factor. In the dissertation, numerical results reveal that the damping factor increases as the acoustic assumption is relaxed and the intensity of pressure perturbations increase. Moreover, non-idealities do not play a significant role within the limit of acoustic perturbations. On the other hand, if the acoustic assumption does no longer apply, non-idealities are found to introduce even higher levels of damping. Remarkably, the dynamics of the probe changes significantly when it is used to measure strong perturbations propagating in a non-ideal flow. Therefore, researchers should carefully account for these results when measuring high frequency pressure fluctuations in ORC turbomachinery applications.

A Bayesian inference framework was developed. First, synthetic data of the MDM flow within the TROVA test-rig were generated using the state-of-the-art fluid model. The inference process was unrolled with the goal of learning the true value of the parameters appearing in the Peng-Robinson fluid model. Results suggest that the considered experiment may not be suitable to achieve the target because, for such test configuration, the thermodynamics shows a loose dependency on model parameters. Indeed, the considered problem largely depends on the operating condition of the test rig. Therefore, operating conditions dominate the development of the flowfield within the test section and they utterly cover up the influence of the thermodynamic model parameters. This also suggests that an accurate knowledge of the values of a few

parameters appearing in the Peng-Robinson model (critical pressure and temperature and acentric factor) is not essential. Indeed, at least for the considered experiment, the numerical solution is almost insensitive to a variation of such parameters, even if they are allowed to vary significantly. Nevertheless, the framework is returning substantial indications towards the development of future experiments. Indeed, the knowledge of the stream temperature is shown to be beneficial, though still not sufficient, to the inference process while Mach and velocity measurements are found to be only slightly relevant. Anyway, the critical pressure and temperature and the acentric factor could never be inferred from the considered experiment. Nevertheless, the framework may be employed for the design of novel future experiments. Indeed, the exploitation of inference techniques based on the virtual simulation of the experimental test-rig,may help experimentalists in anticipating the usefulness of measurements that will be collected. Moreover, the framework could also provide an insight about the optimal probe location, in order to maximize the amount of information extracted from the experiment.

Remarkably, when the inference is carried out exploiting real experimental measurements, the Bayesian process points out either an epistemic uncertainty underlying the computational model of the test section (including a possible epistemic uncertainty affecting the state-of-the-art fluid model for complex compound) or a biased experimental measurement process.

The findings reported in the dissertation helps opening a window on fundamental aspects regarding experiments involving NICFD flows. Namely, evidences show that the tools currently employed to carry out measurements in NICFD flows may not always be suitable and they should be possibly redesigned, to account for non-ideal effects. Moreover, the dissertation provides findings revealing that there is still a not full understanding of the flow dynamics developing within the TROVA test-rig.

Open questions. Despite the recent development in the field of NICFD, a number of questions still remain unanswered. Further experimental campaigns are planned in the near feature, to deepen the investigation of non-ideal flows and to broaden the experimental database. Beside representing a sound base to confirm theoretical advancements, the database will also serve as a set of reference benchmark tests for the validation of NICFD solvers. Different siloxane compounds, including mixtures, are expected to be investigated in the near future at the CREA Lab of Politecnico di Milano. According to the findings reported in the dissertation, particular attention should be pledged to the study of non-ideal oblique shock waves. Questions still remain unanswered about if, and how, the occurrence of non-ideal oblique shock-waves may be exploited (or disrupted) to improve the efficiency of ORC turbomachines. To this extend, experiments may represent the primary means to broaden our knowledge and to validate theoretical models using real data. The design process of new experimental set-ups should be supported by uncertainty quantification techniques aimed at mitigating the effects of non-controllable parameters. Namely, the configuration

of future test-rigs should be robust to operating conditions variability, to manufacturing and assembly tolerances and to uncertainty related to the measurement chain. The numerical tools presented in this dissertation could help defining the type of measurements to be collected and the location of probes, according to the goal of extracting as much knowledge as possible from each experiment.

Results presented in this work revealed potential limitations in the computational model of the TROVA test-rig. Such limitations could be due either to a deficiency of the mathematical form of the state-of-the-art thermodynamic models or to a non-comprehensive representation of the fluid dynamics occurring within the TROVA facility, possibly related to geometrical simplifications applied to represent the domain numerically. Alternatively, results may also indicate a potential bias affecting the (few) experimental data available. Current developments aim at modeling the discrepancies between numerical predictions and experimental measurements. In the future, machine learning techniques are expected to be implemented, to obtain corrective terms tailored on the TROVA test-rig, to directly address model-form errors or measurement bias.

Moreover, it was shown that the design of fast-response probes currently employed to measure strong pressure fluctuation past an ORC turbine rotor does not suit experiment requirements best. Possibly, the community should look for alternative designs developed specifically for ORC applications.

In computational fluid dynamics, a popular strategy to simulate a flow consists in using the Reynolds-Averaged Navier-Stokes equations. Turbulence models must be employed, to reconstruct the Reynold stress term arising from the time-averaged decomposition of the Navier-Stokes equations and to recover the effects related to random velocity fluctuations. Unfortunately, turbulence models often consist in empirical or semi-empirical closures that depend on a set of constants that must be estimated. Unfortunately, the scarce amount of experimental data prevents the correct estimation of such parameters for non-ideal flows. The accuracy of RANS simulations is therefore highly questionable and, currently, there are no publications reporting on the calibration of turbulence model parameters with respect to real experimental data concerning non-ideal flows. The investigation of turbulence in non-ideal flows is therefore a promising research topic. Diverse approaches may be followed to quantify models uncertainty and to improve the accuracy of RANS simulations. For instance, one could attempt to calibrate model parameters based on experimental measurement, for diverse flow configurations. On the other hand, researchers may pledge their efforts to the quantification of epistemic model-form uncertainties and to the application of Machine Learning techniques in data-driven frameworks, to reconstruct the functional form of turbulence unkowns. Moreover, the scarce knowledge regarding the development of turbulent structures in non-ideal flows pave the road for a novel, and possibly prolific, experimental front.

LIST OF FIGURES

LIST OF TABLES